Fall 10-1-2021

Statistical Estimation and Inference Improvements for Exoplanet Discovery

Parker Hinckley Holzer
Yale University Graduate School of Arts and Sciences, holzerparker@gmail.com

Recommended Citation

Holzer, Parker Hinckley, "Statistical Estimation and Inference Improvements for Exoplanet Discovery" (2021). *Yale Graduate School of Arts and Sciences Dissertations*. 350.
https://elischolar.library.yale.edu/gsas_dissertations/350

Abstract

Statistical Estimation and Inference Improvements for Exoplanet Discovery

Parker Hinckley Holzer

2021

The radial velocity method has been widely used by astronomers since the 1990's for discovering extra-solar planets, often referred to as simply "exoplanets". This method involves estimating the radial velocity of a distant star over time using the stellar light, followed by modeling such radial velocity estimates as a function of time using Keplerian-orbital equations with parameters that describe the exoplanet. While a number of approaches exist for estimating the radial velocity from the stellar light, we introduce a new approach for this that uses Hermite-Gaussian functions to reduce the estimation to linear least-squares regression. Furthermore, we demonstrate that this new approach, compared to the commonly used cross-correlation approach, provides an approximate 21% reduction of statistical risk in simulation studies as well as in applications to recently collected data. We then extend this linear model to include additional terms that represent the effect of stellar activity on the observed light, an effect known to both hide and imitate the signal of exoplanets. The F-statistic for the fitted coefficients of these additional terms is found to have higher statistical power than many traditional stellar activity indicators at detecting the presence of stellar activity. Finally, we also use the linear model in a Bayesian framework to merge both traditional steps of the radial velocity method into one that estimates the exoplanet's orbital parameters directly from the time series of observed stellar light.

Statistical Estimation and Inference Improvements for Exoplanet Discovery

A Dissertation
Presented to the Faculty of the Graduate School
of
Yale University
in Candidacy for the Degree of
Doctor of Philosophy

by
Parker Hinckley Holzer

Dissertation Director: John Lafferty

December 2021

Contents

Dedicated to my wife Bethany Holzer for being my constant source of support.

Acknowledgments

From the beginning of my time at Yale University, a good number of individuals have proven pivotal in my success. Were it not for them and their selfless influence, I could not have come nearly as far as I have. First, and foremost, I would like to thank my amazing wife Bethany Holzer. Amidst all of the intense thought put towards coursework and research each day, she is always there as someone who I know I can talk to and turn to for relief and support. Her consistent kindness and selflessness has been a key factor in every step of my Ph.D. program. I would also like to express thanks to my two young sons Aaron and Isaac who, without even realizing it, provide me with a wonderful daily reminder of what truly matters most to me in life: my family.

I would also like to extend my sincere gratitude to Professor Jessi Cisewski-Kehe who provided me the opportunity to begin research in astrostatistics within my very first semester at Yale University. Were I to have begun academic research in later years, I almost certainly would not have completed this dissertation in the same time. She also gave great encouragement as she set aside time to meet approximately every week with me, giving open-minded support for nearly all my ideas and reliably suggesting ways to improve. Her example of persistence and diligence also inspired me greatly many times.

My advisor, Professor John Lafferty, is another who I wish to express deep thanks to. From attending his course on nonparametric estimation and serving as a teaching fellow for two of his machine learning courses, I have learned so many additional techniques in data science that have since proven essential in my research on exoplanet discovery. His willingness to fill the vacancy as my advisor and adapt to my field of research that was well underway demonstrated his great kindness and knowledge, making what could have been a very difficult change for me a seamless transition.

I also wish to thank Professor Debra Fischer and her entire group of researchers in the Department of Astronomy for providing constant and helpful feedback in my research. I am also deeply grateful for their willingness to freely share their precious, recently collected, data that I have used countless times in the papers included here.

Finally, I would like to thank the many members of the Department of Statistics & Data Science who have been such great friends to me throughout my time here. These include, but are not limited to, Professor Jay Emerson, Professor Andrew Barron, Professor Joseph Chang, Brandon Chow, and Soham Jana. I would also like to express my gratitude to the faculty of the University of Utah for preparing me for my graduate program, and to my parents Nelson Holzer and Susan Holzer for the constant love and support they always give.

List of Figures

List of Tables

Chapter 1

Introduction

1.1 Historical Background

Ever since the early 1500's when Nicolaus Copernicus revolutionized our understanding of the universe by concluding with data that the Earth was not the ultimate center, but instead orbited the Sun, mankind has been curious about whether other distant stars also have planetary companions. And if such extra-solar planets (hereafter referred to as "exoplanets") existed, could they host life or give us a better understanding of the Earth's origin? If so, it seemed worth every effort to discover them. Thus began the search for exoplanets, particularly those that are similar to the Earth.

But since nearly all stars in the universe are so distant from Earth, how were such worlds to be detected? Such exoplanets, if they existed, could not emit their own light and were hypothetically much smaller than most visible stars, as is the Earth. Therefore, direct detection of exoplanets was unlikely to be achieved. But astronomers reasoned that the orbital motion of such exoplanets around their host star could influence the much more easily observed light of the host star. Therefore, perhaps exoplanets could be detected indirectly by observing the light from distant stars over time.

Historically, there are two well-known ways by which an exoplanet might impose its signal on the light of its host star. First, from the perspective of the observer, the exoplanet could periodically pass in front of its host star and slightly dim the emitted light. The techniques used to detect such a signal have been given the name of “the transit method”. Second, the orbiting exoplanet would exert a gravitational force on its host star, causing the star to wobble over time. And since a moving light source causes the wavelength of its light to be rescaled (Doppler, 1842), the exoplanet’s gravitational pull would manifest itself in the stellar light’s wavelength over time. Techniques that aim to detect this signal in the star’s light are traditionally labeled as “the radial velocity method”.

Both the radial velocity and transit methods have some notable advantages. As an example, one advantage the transit method has is that it uses photometry (observing the overall brightness of light) rather than spectroscopy (observing the brightness of light as a function of wavelength). Hence, the transit method is able to observe many stars at once with the same instrument, whereas the radial velocity method must observe one star at a time. Consequently, the transit method is the method that has currently discovered more exoplanets. However, one advantage of using the radial velocity method is that the orientation of the exoplanet’s orbit around its host star is much more flexible. For example, if we assume that the orientation angle of the exoplanets orbit with respect to the line connecting the observer to the host star’s center is uniformly distributed, then the probability of a Jupiter-like exoplanet with an Earth-sized orbit transiting the light of a Sun-like star is approximately 1.3×10^{-5}.[1] But as long as the orientation of the orbital plane is not perpendicular to the line of observation, the star’s exoplanet-induced velocity will have a non-zero length component in the direction of the observer, resulting in a radial velocity signal. Another advantage of

---

[1] In this example we assume that the distance from the star to the observer is significantly greater than the radius of the star. To demonstrate the validity of this assumption, we note that the Sun is an average sized star with radius $7 \times 10^8\ m$ and that the closest star is Proxima Centauri at a distance of $4 \times 10^{12}\ m$. So observing this system from Proxima Centauri would satisfy this assumption. In this case, under the assumption that the orbit is circular, the probability can be calculated as the proportion of a half-sphere’s surface area that is above the azimuthal angle $\theta = sin^{-1}\left(\frac{r_p + r_s}{R_o}\right)$ where r_p is the radius of the exoplanet, r_s is the radius of the star, and R_o is the radius of the orbit. Overall, this proportion can be written as $\frac{2\pi R_0^2(1-\cos(\theta))}{2\pi R_0^2} = 1 - \cos(\theta)$.

the radial velocity method is that the signal is present at every point in time. On the other hand, the signal for the transit method is only present for a small time interval when the planet passes between its host star and the observer; at all other locations in its orbit, the signal is absent. Consequently, the radial velocity method is much better at finding exoplanets with relatively long orbital periods. For these reasons, as well as others, the first confirmed detections of exoplanets were made using the radial velocity method.

The first successful detection and confirmation of exoplanets was made by Wolszczan and Frail (1992). However, this was a system of exoplanets orbiting a neutron star, which is a very different type of star than the Sun. It wasn't until a few years later when Mayor and Queloz (1995) discovered the exoplanet 51 Pegasi b, a Jupiter-like planet orbiting a Sun-like star. Finally, the existence of exoplanets was no longer just hypothetical, but also supported by data. For this discovery, Michel Mayor and Didier Queloz were awarded the 2019 Nobel Prize in Physics for expanding our understanding of the Earth's place in the cosmos. Four years after this pivotal discovery, Butler et al. (1999) discovered the first multiple-exoplanet system outside the Solar System. Since then the search for, and understanding the nature of, exoplanets has grown to become a main field of study within the astronomy community.

1.2 The Radial Velocity Method

The radial velocity method of finding exoplanets is based on the realization that, although the mass of an exoplanet is often significantly less than that of its host star, the exoplanet's non-zero mass exerts a gravitational force on its host star. Therefore, as long as the orientation of the orbit is not perpendicular to the observer's line of sight, the star's motion along the line of sight changes. Hereafter, we refer to this line of sight velocity as the host star's radial velocity (RV).

Overall, the RV method is traditionally done in two sequential steps:

1. At each time of observation, estimate the RV of the star using its light.

2. Model the RV estimates vs. time to estimate the parameters that describe the potential exoplanet and its orbit.

Step 1 in this process uses our physical understanding of how light behaves when its source is moving. In what is traditionally called the Doppler effect (Doppler, 1842), the wavelength of the light gets rescaled by a factor that depends on the velocity of the source. Therefore, if we can measure how much the starlight's wavelength got rescaled, we can estimate the RV of the star.

After obtaining RV estimates for each time at which the star was observed, the RV method then proceeds to step 2 where the estimates are modeled as a function of time. Using Kepler's laws of planetary motion, one can show that under reasonable assumptions a star with a single exoplanet companion will have a RV, v, that behaves over time, t, as

$$v(t) = K\left(\cos(\omega + \nu(t; P, e, M_0)) + e\cos(\omega)\right) + C \tag{1.1}$$

where $K,\ \omega,\ P,\ e,\ M_0$, and C are the orbital parameters to be estimated. K is often referred to as the RV semi-amplitude. P is the orbital period of the exoplanet. The eccentricity of the orbit, which is a measure of how non-circular the orbit's shape is, is represented by e. The angle ω gives the orientation of the orbit with respect to the line of sight. M_0 represents where the exoplanet was in its orbit at time $t = 0$. And C gives the offset velocity that accounts for the fact that all stars are moving around the galaxy with a nearly constant velocity on the timescale that is typical of exoplanet surveys[2].

In Equation (1.1), $\nu(t; P, e, M_0)$ is often called the true anomaly and is given as the solution to the two equations

$$E - e\sin(E) = \frac{2\pi t}{P} - M_0 \tag{1.2}$$

---

[2] Most stars have so far not been observed for exoplanet detection purposes more than 10 to 20 years. For the velocity of the star around the Milky Way to change significantly, observations of it would need to span roughly thousands of years as the galaxy has a rotational period of 240×10^6 years.

$$\tan\left(\frac{\nu(t)}{2}\right) = \sqrt{\frac{1+e}{1-e}}\tan\left(\frac{E}{2}\right). \tag{1.3}$$

For a nearly circular orbit where $e \approx 0$, the true anomaly $\nu(t)$ in Equations (1.2) and (1.3) becomes linear in t and $v(t)$ in Equation (1.1) is sinusoidal in t.

If, instead, it is thought that the observed star has multiple orbiting exoplanets, the behavior of the RV over time will be more complicated. Usually, it is assumed that the exoplanet system has had enough time to become stable. Although having any more than a single exoplanet around a star results in mathematical chaos through the well-known "three body problem", on the short timescale of a few years a stable exoplanet system will impose an RV on the star that can still be well modeled over time. Such an RV signal will approximately be the superposition of individual Keplerian orbits, each of which is described by a set of orbital parameters in Equation (1.1).

1.3 The Data: Stellar Spectra

As previously mentioned, the data we have from distant stars is the light they emit. Since the RV method involves detecting a Doppler shift in the stellar light, the wavelength of the light is one critically important variable in the data. And because stars emit light at not just one wavelength but many, the relative brightness of the light at each wavelength is important. Such a two-dimensional data set of various wavelengths of light, X, and the corresponding relative brightness/intensity of each, Y, is called a stellar spectrum.

1.3.1 Data Collection

The origin of a stellar spectrum begins in the core of the star where fusion of hydrogen into helium produces light at a wide range of wavelengths. Depending on the temperature of the star, which can often be approximated as a black body, the brightness of the light will be greater at some wavelengths than others (Planck, 1901). As the light proceeds outwards from the core it passes through the outer atmosphere of the star, often referred to as the photosphere.

Here we recall some basic facts about the nature of light that play an important role in the formation of the stellar spectrum. First, light is composed of individual photons that each have a particular wavelength. Furthermore, a particular wavelength corresponds to a particular amount of energy. Next we note that individual atoms have specific energy levels on which each of its electrons must live. The values of these energy levels is determined by what element the atom classifies as. These electrons can be excited to a higher energy level by absorbing a photon containing the specific amount of energy corresponding to that particular energy level difference. Therefore, because the photosphere of stars contains many elements from the periodic table, some of the photons emitted at the core get absorbed in the photosphere depending on their wavelength. The probability of a photon being absorbed also depends somewhat on the temperature, chemical enrichment, surface gravitational acceleration, and microturbulence of the star.

After passing through the photosphere, the light has fully escaped the star itself and continues onward until reaching the observing instrument. The modern instrument used to collect the stellar spectrum is referred to as a spectrograph. A spectrograph uses a diffraction grating to separate the incoming light into its various wavelengths. Then the separated light is dispersed onto a set of pixels, each of which count the number of arriving photons in a narrow pre-assigned wavelength window. We refer to the resulting array of photon counts as the raw flux[3] $\tilde{Y}$. For pixel i centered on the raw wavelength $\tilde{X}_i$, we assume that the time between photon arrivals is exponentially distributed. Therefore, throughout the observation time, pixel i is observing a Poisson process and we have that

$$\tilde{Y}_i \sim \text{Poisson}(\lambda_i) \quad \text{for } i = 1, 2, ..., N \tag{1.4}$$

---

[3] We acknowledge that what we refer to as “flux” is not a true physical flux.

where λ_i is the mean photon count at pixel i and N is the number of pixels.

For most modern exoplanet surveys, the spectrograph is exposed to the light of the star on the order of minutes. The longer the star is observed, the higher the signal-to-noise ratio (SNR) of the spectrum. But if it is observed for too long, certain assumptions that are made for data corrections such as the barycentric correction (to be explained further in Section 1.3.2) begin to be inaccurate. Often the observation time is somewhere between five and fifteen minutes, partially depending on how far away the star is. This usually results in a raw spectrum where for each pixel i, λ_i is on the order of tens of thousands. Consequently, since a Poisson(λ_i) random variable converges in distribution to a Normal(λ_i, λ_i) random variable as $\lambda_i \to \infty$, we have that

$$\tilde{Y}_i \text{ approx. } \sim \text{Normal}(\lambda_i, \lambda_i) \quad \text{for } i = 1, 2, ..., N. \tag{1.5}$$

Overall, after observing the star M times, the full data set of raw stellar spectra has the form $\left\{(\tilde{X}, \tilde{Y})_{t_m}\right\}_{m=1}^{M}$ where $\tilde{X}$ and $\tilde{Y}$ are the vectors of raw wavelength and raw flux respectively (both of which depend on time), and t_m is the known time of observation m.

1.3.2 Data Corrections

In its raw form, the stellar spectra are not very useful for the purposes of the RV method; both the wavelength $\tilde{X}$ and the flux $\tilde{Y}$ contain physical effects that need to be corrected for.

Barycentric Correction

From the perspective of the Solar System's center of mass (i.e., the barycenter) the RV of a distant star will only be influenced by its nearly constant velocity with respect to the Sun and by orbiting exoplanets. However, because all observations of distant stars are done from the perspective of the Earth, there will always be a time-varying velocity in the data due to the Earth's rotation and orbit around the Sun. Therefore, the first correction to the data is adjusting the wavelength axis of each spectrum $\tilde{X}$ so that the effects of the Earth's motion around the Sun is removed. This is referred to as the barycentric correction.

Even though the Earth's rotation and revolution around the Solar System barycenter often lead to relativistic effects, these motions are well understood and can be corrected for with high precision (Wright and Eastman, 2014; Blackman et al., 2017, 2020). In the end we have corrected wavelength measurements X that represent the scenario of the spectrograph being at the barycenter of the Solar System instead of on the Earth.

Telluric Contamination

Since spectrographs are often ground-based, the light from the star passes through the Earth's atmosphere, causing some additional light absorption in the spectrum that is not representative of the target star. The features in the spectrum that result from this additional absorption are often referred to as tellurics. To correct for this telluric contamination, we use the model created using the approach of Leet et al. (2019). This model provides an estimate of how much light was absorbed at each wavelength by atoms and molecules in the Earth's atmostphere. Although one could potentially divide out shallow tellurics from the spectrum to approximately correct for them with such a model, we take a more conservative approach and mask out all pixels with any non-zero telluric estimate.

Continuum Normalization

In the (unrealistic) scenario where no light absorption occurs in the star's photosphere, the spectrum would appear smooth but not flat. This pattern is still visible when light absorption takes place and is referred to as the spectrum's continuum. The blackbody spectrum (Planck, 1901), together with the instrumental effect often referred to as the blaze function, are among the main reasons why the continuum is not flat in the raw spectrum. In summary, the blaze function describes how some pixels are exposed to more light than others simply due to their placement in the instrument. Because the star's temperature can fluctuate over time, it is traditional to approximately flatten the continuum. This is often referred to as "normalizing" the spectrum.

However, because stars are not exactly blackbodies and there is no known equation for the blaze function, this correction must be done by estimating the continuum. Various normalization techniques have been developed to estimate the spectrum's continuum (e.g., Xu et al. 2019; Petersburg et al. 2020). Once one has a good estimate of the continuum, c, it is simply divided out of the raw flux $\tilde{Y}$ to give

$$Y_i = \frac{\tilde{Y}_i}{c_i} \text{ approx. } \sim \text{Normal}\left(\frac{\lambda_i}{c_i}, \frac{\lambda_i}{c_i^2}\right) \quad \text{for } i = 1, 2, ..., N. \tag{1.6}$$

A spectrum where the continuum has been normalized (i.e., flattened with a maximum amplitude of one plus noise) is hereafter referred to as a *normalized spectrum*.

A small section of the Sun's normalized spectrum, as collected by the National Solar Observatory (NSO) (Rimmele and Radick, 1998), is shown in Figure 1.1. This gives an example of what the spectrum looks like after all corrections have been applied. Figure 1.1 plots the normalized flux Y as a function of wavelength X.

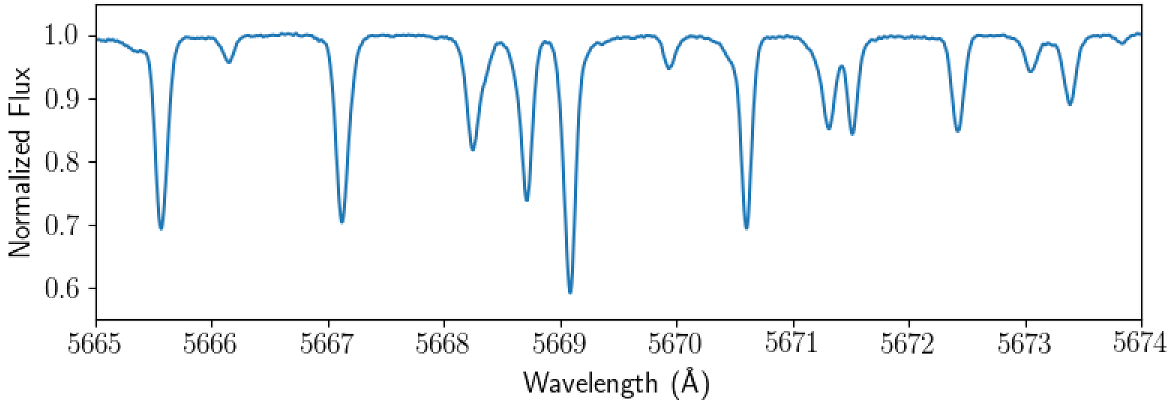

Figure 1.1: A subset of the NSO spectrum of the Sun between 5665 and 5674 $\AA$.

The narrow dips in the normalized flux are spectral absorption features which have variable intensity and frequent blending with neighboring features. Each absorption feature corresponds to a particular electron energy level difference in a particular element or molecule of the star's photosphere. One reason why the absorption features are spread across a narrow range of wavelengths instead of a sharp delta function at one wavelength value is because the gases in the photosphere are in motion. Another reason is because each spectrograph has a finite resolution which smears out the signal by a certain amount.

One could note that physically, the Doppler shift that we intend to detect happens to the raw spectrum, not the normalized spectrum. So perhaps we are losing some of the signal by applying the continuum normalization. To briefly analyze this, we introduce a couple new terms that will be used from here on out. We define the *template spectrum* τ as the normalized spectrum with no Doppler shift, noise, or other time-dependent effects. We further define the *difference spectrum* to be the difference between Y (the observed normalized flux) and τ.

With x representing the wavelength and $f(x)$ representing the normalized spectrum with no noise, we can write the actual (unnormalized) spectrum with no noise as $F(x) = b(x)f(x)$ where $b(x)$ accounts for the blackbody effect and the blaze function. As long as the underlying RV is small (in our methods only the relative RV between observations needs to be small), the corresponding Doppler shift would cause a difference spectrum that is approximately a constant multiple of $F'(x)$ (more details on this will be provided in Chapter 2) which is equal to $b'(x)f(x) + b(x)f'(x)$.

Now, under the assumption that the continuum normalization is done accurately (i.e., that $b(x)$ is well estimated), the normalized difference spectrum can be written as a constant multiple of $\frac{F'(x)}{b(x)} = \frac{b'(x)f(x)}{b(x)} + f'(x)$. This leads to an assumption, when estimating the RV, that the first term $\frac{b'(x)f(x)}{b(x)}$ is negligible compared to the second term $f'(x)$.

To check this, consider the (simplified but representative) scenario where $b(x) = -60(x-5020)^2 + 68000$ and $f(x)$ is the normalized smoothed NSO spectrum used in Figure 1.1, and x is the wavelength between 4990 and 5050 Å. The resulting unnormalized spectrum $F(x)$ is shown in Figure 1.2.

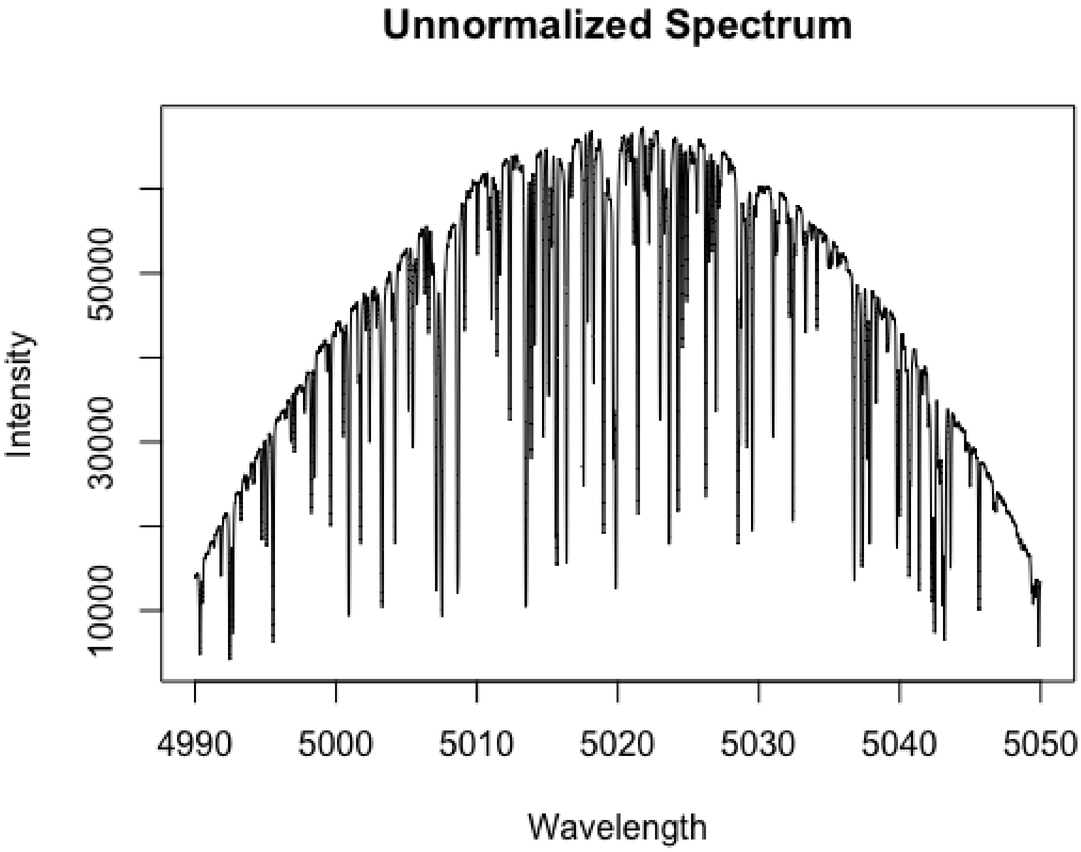

Figure 1.2: Example of unnormalized spectrum without noise.

Now in this case, we can calculate $b'(x)$ exactly and get a good estimate of $f'(x)$ with cubic splines. This in turn gives the results shown in Figure 1.3. Because the values for the first term are small compared to those of the second term, it appears (from this simple illustration) that there is not a significant Doppler signal lost by normalizing the continuum.

1.4 Current Limitations

The RV method contains some noteworthy limitations, some of which have been overcome in the twenty-five years of exoplanet discovery. Still, some limitations continue to make discovery of Earth-like exoplanets particularly difficult.

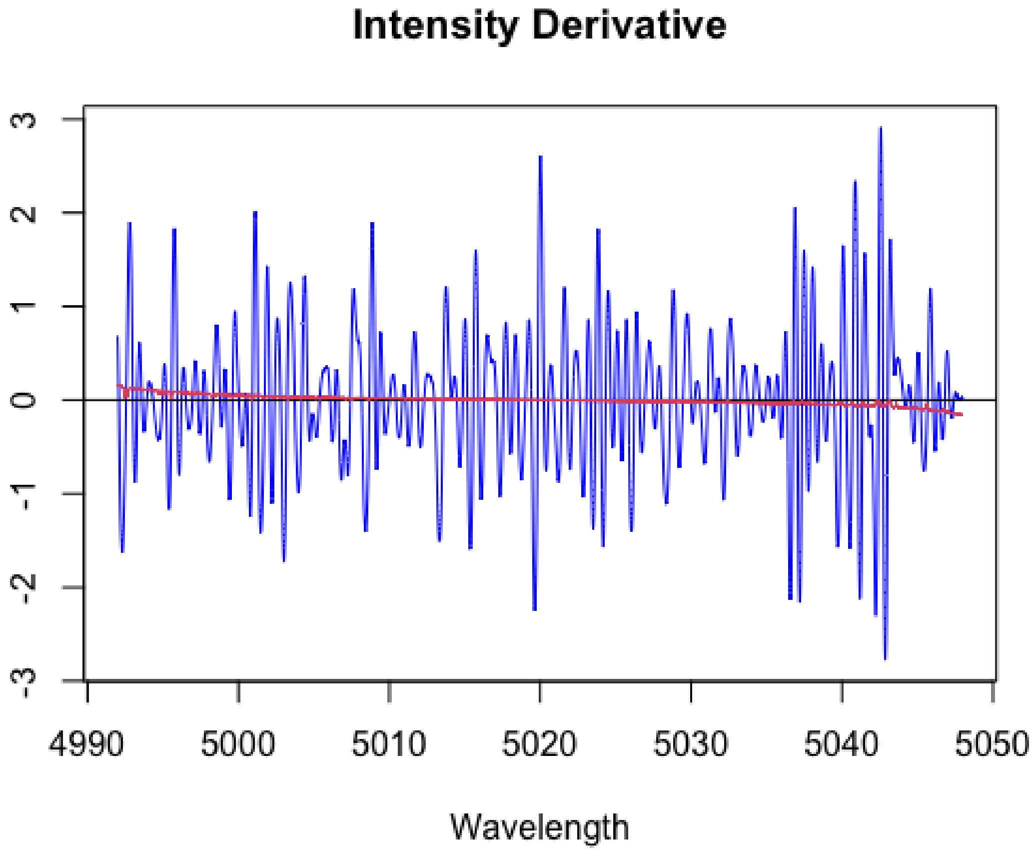

Figure 1.3: Example of the two components of the unnormalized spectrum's derivative. The derivative of the normalized flux is plotted in blue, and the remaining term is plotted in red. Note that a difference spectrum due to a small Doppler shift can be well approximated as a constant multiple of the sum of these two terms.

1.4.1 Small Signal

Perhaps the most intuitive limitation of the RV method is how small the scale of the Doppler signal in the stellar light typically is. As previously mentioned, the RV method aims to detect a periodic Doppler shift in the star's light, which is a rescaling of the wavelength. Furthermore, such a Doppler shift would be due to the gravitational pull of the orbiting exoplanet on the star. However, since the Sun is nearly 3.33×10^5 times more massive than the Earth, it should be intuitive that the Earth's (nonzero) gravitational pull on the Sun causes a very minuscule change in the Sun's motion.

In the solar system, Jupiter induces a RV with a magnitude up to about 12 m s^{-1} for the Sun while the lower mass Earth only induces a RV up to about 0.09 m s^{-1}. If observed with high spectral resolution of 1.5×10^5, one pixel on the detector spans about 500 m s^{-1}, so these RVs would only shift the solar spectrum by 0.024 or 0.00018 pixels, for Jupiter and the Earth, respectively. Further complicating the detection, these tiny shifts are merely the semi-amplitudes of nearly sinusoidal RV variations with periods of about 12 years for Jupiter and 1 year for the Earth. Because the RV signal is so tiny compared to the speed of light, detecting such a sub-pixel shift in stellar absorption features is non-trivial. The state-of-the-art Doppler precision for the past decade has been about 1 m s^{-1} (Fischer et al., 2016). This is sufficient to detect Jupiter (with 12 years of observations), but precludes the detection of Earth analogs around Sun-like stars. Because the RV amplitude increases with decreasing stellar mass (all else equal), some Earth mass planets have been detected around stars that are lower in mass than the Sun. Figure 1.4 shows the velocity amplitudes and orbital periods of exoplanets detected using the RV method over the past 25 years. Note the obvious gap between the currently known exoplanets and the Earth.

For further intuition behind this small signal, consider trying out the following exercise. An Earth-Sun system would have a RV of magnitude up to about 0.09 m s^{-1}, which is approximately 0.2 miles per hour. For this exercise we remind the reader that the wavelength of light corresponds with the color of the light. Therefore, if the wavelength gets rescaled, the color should change slightly. Now pull out your cellphone and find the app icon that is your favorite color. Focusing your eyes on that icon, hold it an arm's length away from you. Now move your phone towards your eyes at a speed that takes about 8 seconds to reach your eyes. This is a good approximation of the speed the Sun moves due to the Earth's pull. Can you see the icon's color change when you start moving it towards you?

The inability of the human eye to see such a small signal is also present in the stellar spectrum. This is demonstrated in Figure 1.5 which plots two noiseless normalized spectra

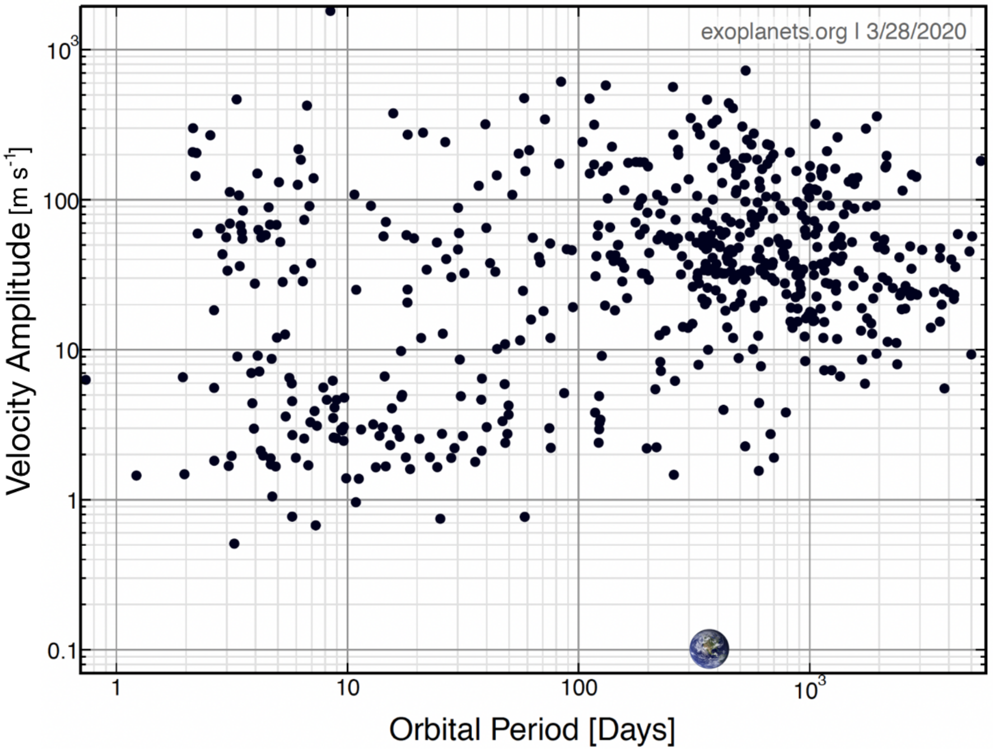

Figure 1.4: Orbital period and stellar RV semi-amplitude for all exoplanets discovered with the RV Method. Data come from Exoplanets.org (Han et al., 2014) on March 28, 2020 with a total of about 800 exoplanets. Note the symbol of the Earth at an orbital period of 365.25 days and a velocity amplitude of approximately 0.1 m s^{-1}, and that analogs of the Earth were not detectable.

on top of each other, one having no Doppler shift and the other having a 10 m s^{-1} Doppler shift. Note that the two spectra in Figure 1.5 appear visually on top of each other, even though this signal is 100 times larger than what would be produced by an Earth-Sun system.

The minuscule nature of the signals we are searching for requires very careful consideration of assumptions that go into modeling. Were an assumption to not be correct, our model could easily miss the important Doppler shift in the data.

1.4.2 Instrumental Effects

Because the Doppler signal due to low-mass exoplanets is so small, the uncertainty in the estimated RV must be carefully budgeted. The RV error budget is partially influenced by in-

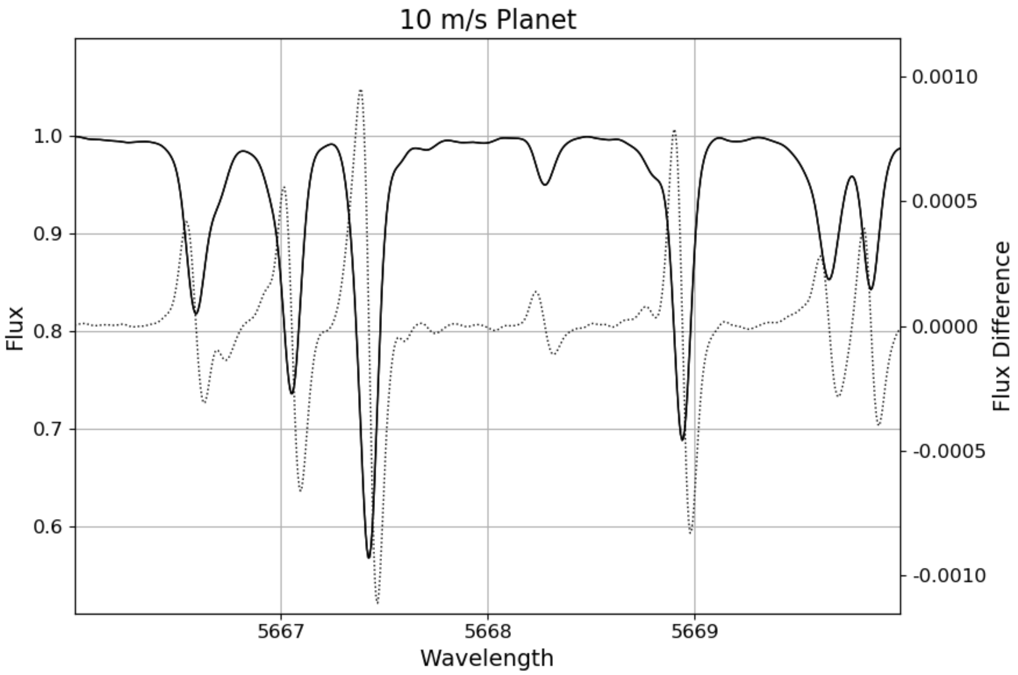

Figure 1.5: Two noiseless normalized spectra in the wavelength interval from 5666 and 5670 Å. Both spectra are plotted in solid line according to the left vertical axis. Because there is no visual difference between the two (which is the main point of this plot), the difference is also plotted in dashed line according to the right vertical axis.

strumental errors. Over the years a number of spectrographs have been developed (Baranne et al., 1996; Pepe et al., 2002; Mayor et al., 2003; Anglada-Escudé and Butler, 2012; Cosentino et al., 2012). However, these instruments have low stability and produce RV errors that both hide a true signal and give false positive detections of exoplanets. The EXtreme PREcision Spectrometer (EXPRES) (Jurgenson et al., 2016; Blackman et al., 2020; Petersburg et al., 2020) is a newly commissioned instrument that was designed to significantly reduce instrumental errors. The primary goal of the EXPRES instrument is to provide higher fidelity data (high signal-to-noise with reduced instrumental errors) and has demonstrated intrinsic instrumental measurement precision better than 0.1 m s^{-1} (Blackman et al., 2020). Consequently, the data we use in this study comes from EXPRES.

1.4.3 RV Estimation Procedure

While the first traditional step of the RV method, as described in Section 1.2, is rather straightforward in theory, there are a wide variety of methods used to implement it in practice. The traditional cross correlation function (CCF) method (Baranne et al., 1996) has long been used to measure Doppler shifts in stellar spectra by minimizing a weighted dot product between the observed spectrum and a template (Pepe et al., 2002). Various template matching algorithms have also been developed, which minimize the (interpolated) sum of squared differences between the spectrum and a template spectrum using the Doppler shift as a free parameter (Anglada-Escudé and Butler, 2012; Astudillo-Defru et al., 2015). A variant of the template matching approach assumes the Doppler shift is small and estimates the derivative of the spectrum from the template (Bouchy et al., 2001; Dumusque, 2018). The EXPRES analysis pipeline has implemented the CCF method, as well as a higher precision Forward-Modeling (FM) code that makes use of a very high signal-to-noise (S/N) stellar template to model a Doppler shift in every 2-Å segment of the observed spectrum (Petersburg et al., 2020).

Even though these techniques have been around for many years, there is still very little understanding of how they perform with respect to each other. Often one's choice of technique for RV estimation is more a matter of tradition than of minimal statistical risk. In Chapter 2 we introduce a new approach for estimating the RV and demonstrate that it has lower statistical risk, in both simulation studies and with real data, than the traditional CCF method.

1.4.4 Stellar Activity

Perhaps the most significant limitation is that of stellar activity in the atmosphere of stars, an example of which is the presence of star spots. Better understanding the activity that takes place in the atmospheres of stars is an important and ongoing goal in the astronomy community (Fischer et al., 2016; Dumusque et al., 2017; Davis et al., 2017; Jones et al., 2017; Dumusque, 2018; Cretignier et al., 2020). One reason why this is the case is because stellar activity can produce RV's that mimic, or hide, the signal induced by an orbiting exoplanet (Saar and Donahue, 1997; Queloz et al., 2001; Desort et al., 2007; Meunier et al., 2010). This is one of the main hinderances to discovering more Earth-like exoplanets around Sun-like stars (Hatzes, 2002; Lagrange et al., 2010; Isaacson and Fischer, 2010). Therefore, to discover more planetary systems similar to the Earth-Sun system, we likely need a better way to detect the presence of, and ideally remove the effects of, stellar activity in stellar spectra.

In Chapter 3 we introduce a new statistic that is shown through simulation to have higher power for detecting the presence of stellar activity than many traditional stellar activity indicators. We then detail in Chapter 4 a first attempt to extend the methodology of Chapter 2 for the purposes of correcting the effects of stellar activity. Finally, we present a novel implementation of the RV method that combines its two traditional steps in Chapter 5, and explain its potential to improve the stellar activity corrections with future work.

Chapter 2

A Hermite-Gaussian Based Exoplanet Radial Velocity Estimation Method

Parker H. Holzer, Jessi Cisewski-Kehe, Debra Fischer,

Lily Zhao

Holzer et al. (2021a)

2.1 Introduction

In this work we introduce a new method for implementing the RV-estimation step of the RV method for exoplanet discovery. The new method we propose for estimating the RV is designed to work well in the small RV regime typical of orbiting exoplanets. Additionally, the proposed method is developed to generalize well to other stars with enough discernible absorption lines. This is because the modeling is carried out on the spectra observed for an individual star, and does not require a pre-specified template. The only interpolation that takes place in the proposed method is on a high signal-to-noise (S/N), oversampled, template spectrum (derived from the data). Compared to the approach of Anglada-Escudé and Butler (2012) which requires interpolation of every (low S/N) observed spectrum, the numerical error introduced through interpolation is likely reduced in the new proposed method. Perhaps most importantly, the new method simplifies the RV estimation process to simple linear regression without the need for getting a nonparametric estimate of both the spectrum and its derivative. This allows the method to easily account for the heteroskedastic noise in spectra. Furthermore, this simplification allows for straightforward statistical inference on the estimated RV without making assumptions regarding the validity of “propagation of error” (i.e., the delta method) or other approximate estimates of the standard error.

The proposed Hermite-Gaussian Radial Velocity (HGRV) estimation method makes use of the well-known Hermite-Gaussian functions. These functions have been used extensively in solving Schrodinger’s Equation for models of quantum systems (Marhic, 1978; Dai et al., 2016), as well as in fitting emission lines in galaxy spectroscopy (Riffel, 2010). The key contribution of this paper is that shifts of spectral lines between two spectra (e.g., due to a Doppler shift) can be well estimated with the first Hermite-Gaussian function fitted to the *difference* spectrum.

The use of the Hermite-Gaussian functions is mainly motivated by the method’s assumption that absorption features are Gaussian shaped (an assumption that can be generalized). It is important to note that large optical depth, rotational broadening, collisional broadening, stellar activity, and other astrophysical effects can cause absorption features to depart from a Gaussian shape. (The model misspecification due to this Gaussian-shape assumption is explored in Section 2.3.4.)

In Section 2.2 we propose an algorithm for finding absorption features in the spectrum that will be used in the HGRV method. Section 2.3 includes details of the proposed HGRV method, and simulation study results are discussed in Section 2.4. Section 2.5 then applies the method to recently collected data of 51 Pegasi by EXPRES. A discussion is provided in Section 2.6 and we conclude in Section 2.7.

2.2 Absorption Feature Finding Algorithm

An important characteristic of the HGRV method is that, rather than modeling a Doppler shift in the spectrum as a change in the explanatory variable (wavelength) as the CCF method does, we can model the difference in normalized flux caused by the Doppler shift. This characteristic is present in various other RV detection methods (Bouchy et al., 2001; Rajpaul et al., 2020), but it is implemented rather differently with our proposed method.

Since a Doppler shift only rescales the wavelength axis, there is little RV information in the normalized continuum. Most of the information for small Doppler shifts comes from the high-derivative regions of spectral lines, so identification of the absorption features in a given spectrum is the first step for the HGRV method.

The locations, depths, and degree of blending of absorption features depend on the stellar parameters and chemical composition of the star and, therefore, vary from star to star. The HGRV method involves modeling individual absorption features so an algorithm is needed that not only identifies the central wavelength at which each feature occurs, but also the wavelength bounds that contain the feature. Were all absorption features to be well-separated, these wavelength bounds would nearly be symmetric about the central wavelengths with a nearly-constant width. However, since blends are very common, this is not the case in practice.

Designing the HGRV method to generalize across stars motivates the use of an algorithm for identifying absorption feature wavelength bounds in a way that can adapt to different spectra. The proposed absorption feature finding algorithm is a statistically-motivated heuristic algorithm. The overarching goal is to find wavelength windows of absorption features, not to perform any statistical inference on them.

Various algorithms already exist for detecting spectral features, particularly for emission lines in spectra of galaxies. However, they contain some limitations that make them unsuitable for the proposed methodology. For example, some were developed for absorption features of specific elemental species or line types[1] (Frank, 2008; Zhao et al., 2019), require experimental supervision (Labutin et al., 2013), partially consist of extensive human intervention and physical insight (Sharpee et al., 2003), or assume the features are sparse and well-separated (Tonegawa et al., 2015).

More importantly, these algorithms lack an important component needed for our analysis: estimating not just the central wavelength at which the feature occurs, but also the wavelength bounds that contain the feature. Dumusque (2018) approaches this by taking a fixed number of pixels around each feature center, but acknowledges that these windows could be further optimized. The reason for this is because a fixed pixel count for each wavelength window does not take into account different sizes of absorption features nor blends between neighboring features. Cretignier et al. (2020) improves upon this by allowing the number of pixels to vary for each feature but, by restricting the windows to be symmetric about the minimum, does not account for effects of line blends. Our proposed algorithm improves upon this by using an approach that accounts for these blends.

The algorithm has two main sequential steps: (i) identify local minima that are likely to be absorption lines and (ii) proceed outward from each local minimum until the normalized flux flattens out. This algorithm is detailed in Algorithm 1.

This algorithm requires three tuning parameters: a wavelength window size m in units of pixel count, and significance levels $\alpha,\ \eta$ where $\eta \geq \alpha$. Algorithm 1 works as follows. For a given pixel index i, let $\Lambda_{l,i}$ and $\Lambda_{r,i}$ be the wavelength regions of size m pixels to the left and right of the wavelength for pixel i, x_i, respectively. Also, let $Y_{l,i}$ and $Y_{r,i}$ be the corresponding flux regions. Algorithm 1 uses least-squares regression on each region to estimate coefficients $\beta_{0,l}$ and $\beta_{1,l}$ for the left region in addition to $\beta_{0,r}$ and $\beta_{1,r}$ for the right region (see Algorithm 1 for the model). If $\beta_{1,l}$ is found to be negative and $\beta_{1,r}$ positive

---

[1] The central wavelength of each spectral line corresponds to a particular electron state transition of atoms responsible for absorbing photons in the stars atmosphere. These central wavelengths depend on the species of the absorbing atom and its ionization state.

Algorithm 1: Absorption Feature Finder

```
Data: ordered wavelengths $\Lambda = (x_0, x_1, ..., x_n)$ and corresponding flux values
      $\tau = (\tau_0, \tau_1, ..., \tau_n)$
Initialize tuning parameters $m \in \mathbb{N}$, $\alpha \in (0, 1)$, and $\eta \in (\alpha, 1)$
for $x_i \in \Lambda$ do
    set $\Lambda_{l,i} = (x_{i-m+1}, x_{i-m+2}, ..., x_i)^T$, $\Lambda_{r,i} = (x_i, x_{i+1}, ..., x_{i+m-1})^T$,
      $\tau_{l,i} = (\tau_{i-m+1}, \tau_{i-m+2}, ..., \tau_i)^T$, and $\tau_{r,i} = (\tau_i, \tau_{i+1}, ..., \tau_{i+m-1})^T$
    model $\tau_{l,i} = \beta_{0,l}\mathbb{1}_m + \beta_{1,l}\Lambda_{l,i} + \varepsilon$ and $\tau_{r,i} = \beta_{0,r}\mathbb{1}_m + \beta_{1,r}\Lambda_{r,i} + \varepsilon'$ where
      $\varepsilon, \varepsilon' \sim N(0, \varsigma^2 I_m)$ and $\mathbb{1}_m = (1, 1, ..., 1)^T$ with length $m$
    get p-values $p_{l,i}$ for testing $\beta_{1,l} = 0$ against $\beta_{1,l} < 0$ and $p_{r,i}$ for testing $\beta_{1,r} = 0$
      against $\beta_{1,r} > 0$
end
Initialize index $j = m$ and upperbound $u = 0$
while $j \leq \text{length}(\Lambda) - m + 1$ do
    if $p_{l,j} < \alpha/2$ and $p_{r,j} < \alpha/2$ then
        set $k_{\max} = \max\{k \in \{u, u+1, ..., j\} : p_{l,k} \geq \eta\}$
        set $k_{\min} = \min\{k \in \{j, j+1, ..., \text{length}(\Lambda)\} : p_{r,k} \geq \eta\}$
        save $\left(\frac{x_{k_{\max}} + x_{k_{\max}-m}}{2}, \frac{x_{k_{\min}} + x_{k_{\min}+m}}{2}\right)$ as absorption feature
          wavelength bounds
        $j \leftarrow \lfloor (k_{\min} + m/2) \rfloor$
        $u \leftarrow j$
    else
        $j \leftarrow j + 1$
    end
end
```

with statistical significance, then x_i is considered a statistically significant minimum. At this point we apply a Bonferroni correction by using the significance level $\alpha/2$ for each slope. Algorithm 1 then proceeds outwards in wavelength until the estimates are no longer statistically significant, at which point the central wavelength of the window is taken as a feature bound. To further avoid the drawbacks of multiple testing, we eliminate any detected absorption features that do not have a depth above a certain threshold. We note, however, that multiple testing is not a concern since our goal is to find absorption features, and we do not use the statistical significance beyond the detection of the features. The algorithm is also illustrated with the flowchart shown in Figure 2.1.

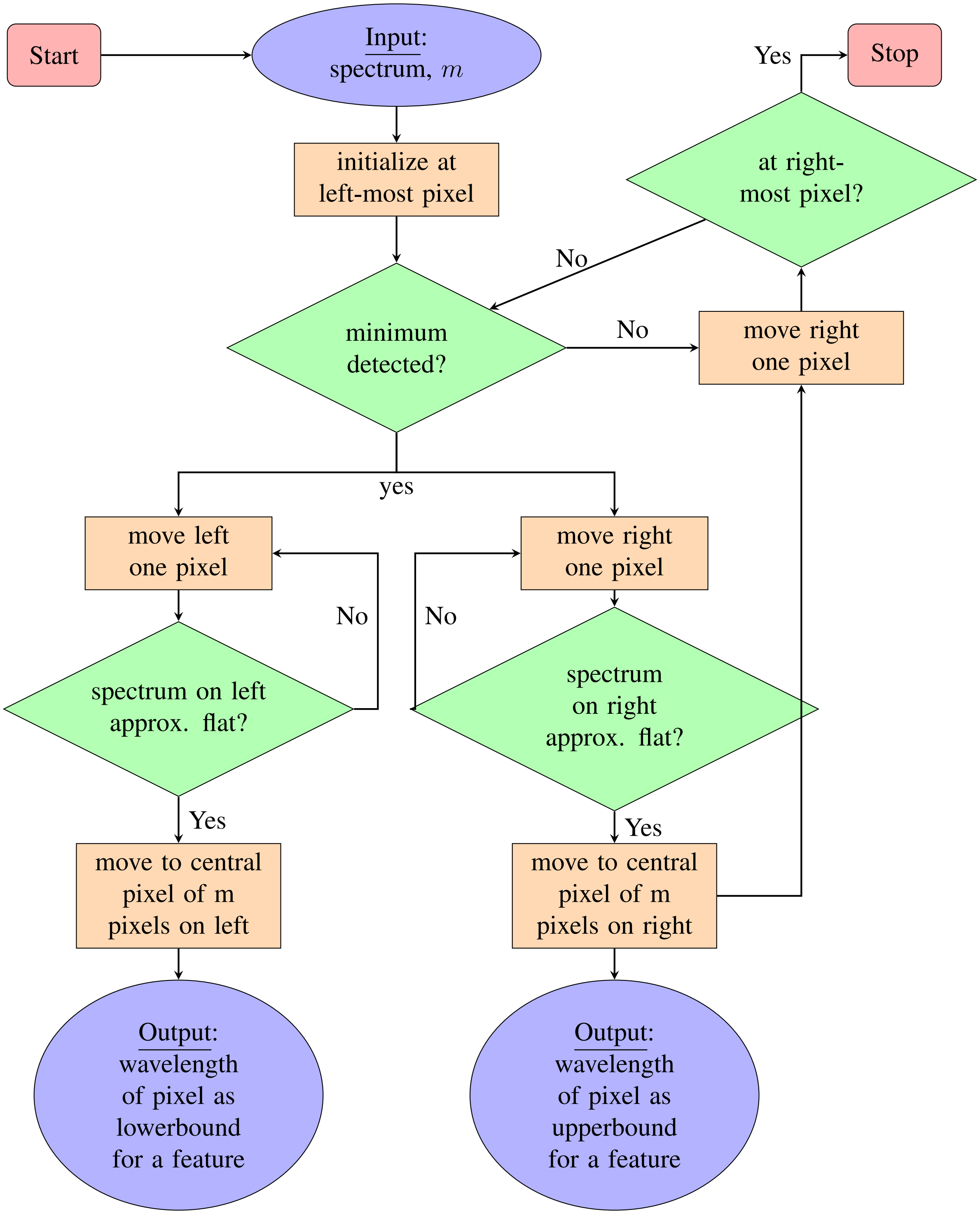

Figure 2.1: Absorption Feature Finder flowchart for Algorithm 1.

It was found that when m is too small, many false absorption features are detected. When m is too large, many small features are missed. Even though similar effects come from α and η being too large or small, the effects appeared more sensitive to m. For fixed values of α and η, we adjusted m until the number of detected features was maximized. At this point we increased or decreased α if many small features were missed or many false features were detected. If many blended features were detected as single features or the wavelength bounds did not encompass full absorption features, we decreased or increased η, respectively, and repeated the full process.

This algorithm was empirically evaluated using the NSO spectrum. After the step-by-step optimization of the three tuning parameters described in the preceding paragraph, we found that $m = 25$, $\alpha = 0.01$, and $\eta = 0.05$ found the most absorption features. Furthermore, we visually-identified no false positives remaining after eliminating features with a line depth less than 0.015. A subset of the absorption features found in the NSO spectrum are shown in Figure 2.2.

When applying Algorithm 1 to the NSO spectrum, we get the results shown in Figures 2.3 and 2.4. Figure 2.3 displays the portion of the spectrum that was not contained in any detected absorption features and compares it to the full spectrum. Figure 2.4 displays some examples of absorption features that were missed by the algorithm. These figures illustrate that 97.7% of the squared deviation from 1.0 in the normalized flux is accounted for by the 64.4% of the spectrum contained in the wavelength bounds given by the algorithm.

It is also noticeable that some absorption features are missed by the algorithm, some of which are deep. Most of these were missed because, as illustrated in Figure 2.4, the features are strongly blended in a way that makes the slope in either direction at the core statistically insignificant. There are likely ways to improve upon this aspect of the algorithm, and we leave this to future work.

To estimate the false-positive rate of this algorithm, we considered the NSO spectrum between 5000 and 6000 Å and replaced the normalized flux axis with a flat 500 S/N sim-

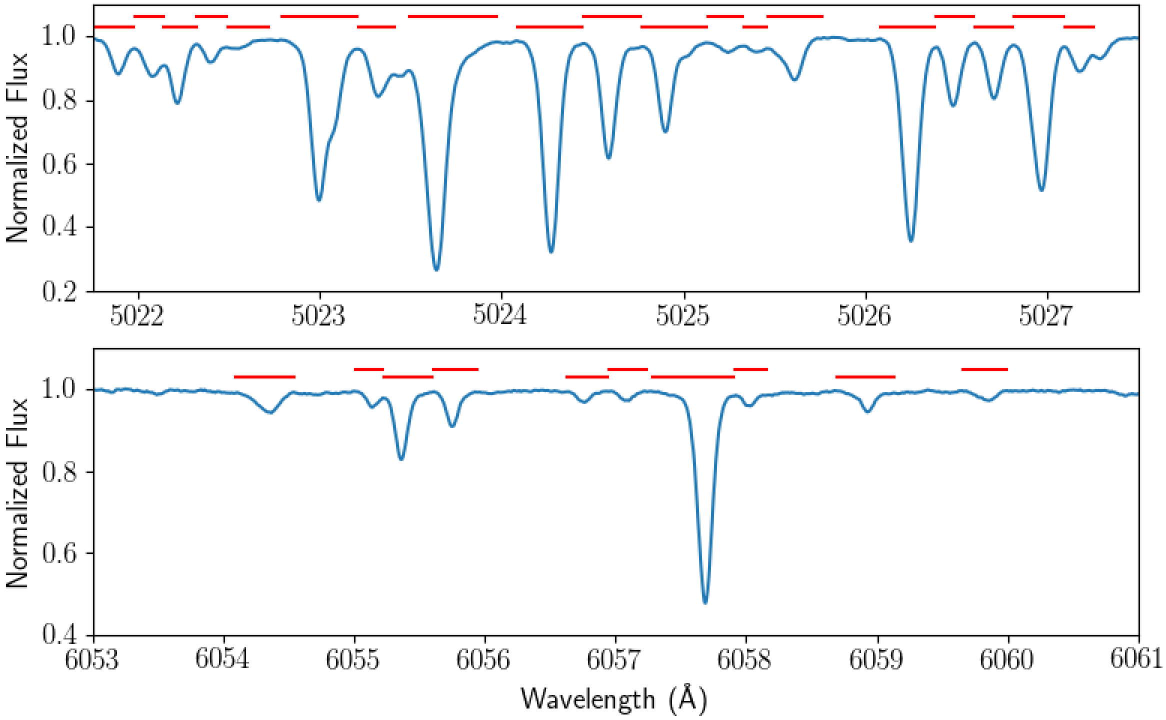

Figure 2.2: Results of using the Absorption Feature Finder algorithm on the NSO Spectrum. Red horizontal lines show the wavelength windows found to correspond to individual absorption features.

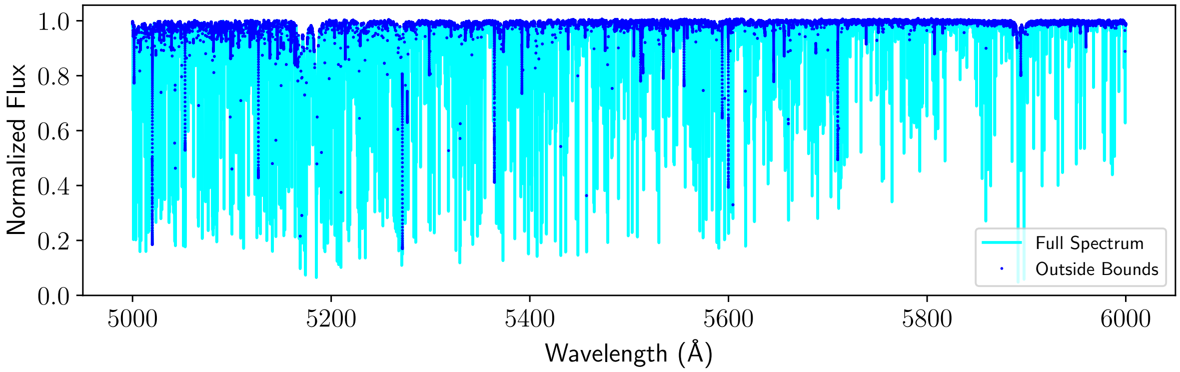

Figure 2.3: The full NSO spectrum used in testing Algorithm 1. Normalized flux is plotted against the wavelength. The full spectrum is plotted in light blue. The thick dark blue points indicate the portions of the spectrum that are not contained in any of the wavelength bounds given by the algorithm.

ulation 20 independent times. See Sections 2.3.5 and 2.4.1 for details on how we estimate a template spectrum with this level of S/N, and which we use in the Absorption Feature

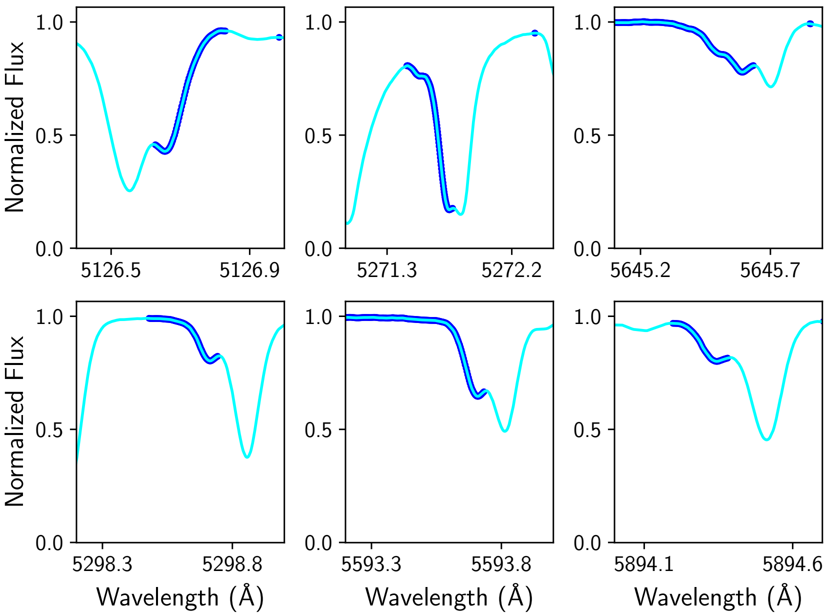

Figure 2.4: Six of the absorption features in the NSO that were missed by Algorithm 1. Normalized flux is plotted against wavelength. The full spectrum is shown in light blue, and portions not included in any of the wavelength bounds given by the algorithm is shown in dark blue.

Finder (AFF) algorithm. Applying the AFF algorithm to these simulations with parameters $m = 25$, $\alpha = 0.01$, and $\eta = 0.05$ gave a total of 55 detected features. Since the spectra did not have any absorption features, this approximates the false positive rate as 1 absorption feature per 363 Å. Additionally, the line depths of these 55 false features had mean 0.0046, standard deviation 0.0018, and maximum 0.0098 so that all the false lines would be eliminated with the minimum line depth parameter set to 0.015. Note that for spectra with either different S/N or resolution m, α, η, and the minimum line depth may need to be adjusted (e.g., a lower S/N or resolution may need higher significance levels or a higher minimum line depth). We recommend setting m to be approximately $25 \times \dfrac{R}{2 \times 10^6}$ where R is the resolution of the spectrum, and the minimum line depth to be approximately $0.015 \times \dfrac{500}{\mathrm{S/N}}$. This recommended threshold is, in part, motivated by the idea that avoiding false lines, which can corrupt the RV estimate, may be more beneficial than detecting every true line.

To analyze how the minimum line depth parameter depends on the S/N of the spectrum, we extend the false positive rate simulation done with a S/N of 500 described in the previous paragraph. For each S/N from 250 to 1500 in equal steps of 250, we take the NSO spectrum between 5000 and 6000 Å and replace the flux axis with noise 20 independent times. We then apply Algorithm 1 to each of the 20 resulting spectra with parameters $m = 25$, $\alpha = 0.01$, and $\eta = 0.05$. We then collect all detected absorption features from the 20 spectra.

The total count of false absorption features detected ranged from 51 to 56 and showed no association with the S/N level. Furthermore, the depth of these false features is illustrated in Figure 2.5. The recommended minimum line depth parameter, $0.015 \times \frac{500}{\mathrm{S/N}}$, is also shown.

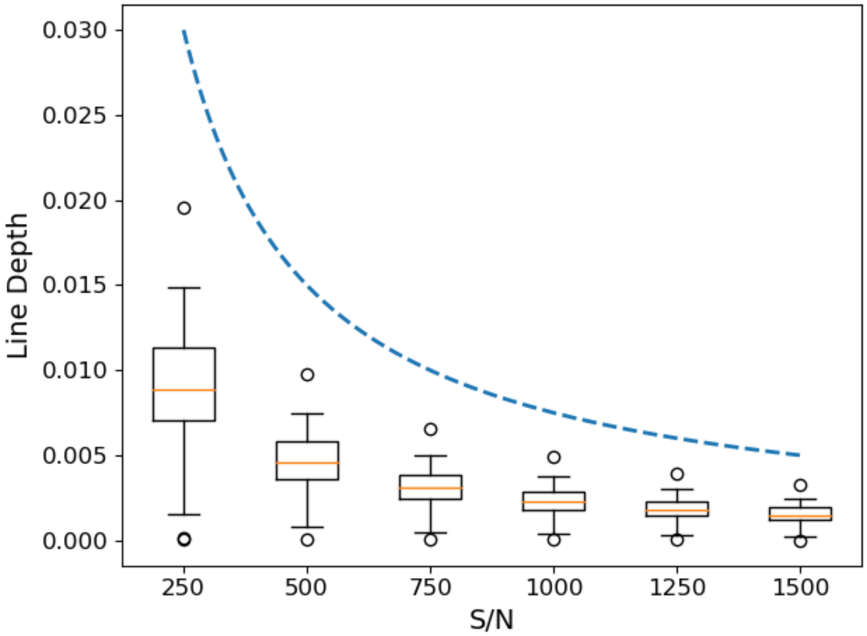

Figure 2.5: Results from our simulation of the false positive rate of Algorithm 1 at various S/N, shown on the horizontal axis. The distribution of line depths for these false positives is represented by box plots according to the vertical axis. The count of false positives remained approximately constant at 1 absorption feature per 363 Å for each S/N. The dashed line represents our recommended value for the minimum line depth parameter in the algorithm given by the expression $0.015 \times \frac{500}{\mathrm{S/N}}$.

The proposed algorithm may have difficulty distinguishing two spectral lines that are strongly blended together because the slope of the normalized flux may not flatten out between the two lines. Depending on the S/N of the spectrum, it may not be able to find small features as the noise would reduce the statistical significance of the left and right slopes. The lower the S/N is, the narrower the wavelength bounds will be for each detected absorption feature. This is because as we move outwards from the central wavelength of a feature, the slope eventually decreases in magnitude and becomes statistically insignificant sooner in the presence of more noise. We find that as long as the spectrum has a S/N above 500 the results of our algorithm are stable whether or not one accounts for the heteroskedastic nature of the noise. We use the estimated template spectrum (described in Section 2.3.5) in the AFF algorithm, and demonstrate in Section 2.4.1 that the template has a S/N above 500 as long as there are at least 11 observed spectra provided.

2.3 Hermite-Gaussian RV Method

We now introduce the HGRV method by first considering the difference imposed on a Gaussian by a multiplicative shift of its argument. We introduce a theorem that quantifies the approximation error made by using only the first-degree Hermite-Gaussian function to model this difference, and provide the proof through four lemmas. We then show that, in the context of stellar spectroscopy, this approximation error is small and the coefficient of the first-degree Hermite-Gaussian function is nearly a constant multiple of the RV. This allows us to extend to the case of multiple absorption features and reduce the problem of estimating the Doppler shift in a spectrum to linear regression.

2.3.1 Mathematics of a Doppler-shifted Gaussian

If x represents the wavelength of light and $f(x)$ represents the normalized flux of light at that wavelength, then the normalized flux of Doppler-shifted light is represented mathematically as $f(\xi x)$ where $\frac{1}{\xi}$ is referred to as the Doppler factor (Doppler, 1842). In special relativity,

ξ is given by

$$\xi = \frac{1 + v_r/c}{\sqrt{1 - (v/c)^2}} \tag{2.1}$$

where c is the speed of light (Einstein et al., 1905), v is the absolute speed of the source, and v_r is the velocity along the line of site of the observer. While the Earth's rotation and revolution around the solar system barycenter often lead to relativistic effects, these motions are well understood and can be corrected for with high precision (Wright and Eastman, 2014; Blackman et al., 2017, 2020). Furthermore, the velocity due only to orbiting exoplanets is well below the speed of light. Therefore, under the assumption that the barycentric corrections are applied accurately and $v \ll c$, ξ can be well approximated with the classical formula

$$\xi = 1 + \frac{v_r}{c}. \tag{2.2}$$

Consider the effect of a Doppler shift when $f(x)$ is a Gaussian like many of the inverted absorption features in a spectrum (Gray, 2005). To model this we propose the Hermite-Gaussian functions, $\psi_n(x)$, defined as

$$\psi_n(x) = \frac{1}{\sqrt{2^n n! \sqrt{\pi}}} H_n(x) e^{-(x^2)/2} \tag{2.3}$$

where $H_n(x)$ represents the n'th degree (physicist's) Hermite polynomial which can be written in closed form as

$$H_k(s) = k! \sum_{m=0}^{\lfloor k/2 \rfloor} \frac{(-1)^m}{m!(k-2m)!} (2s)^{k-2m} \tag{2.4}$$

with $\lfloor a \rfloor$ representing the floor function that returns the largest integer less than or equal to the real number a (Lanczos, 1938).

An illustration of the first four Hermite-Gaussian functions is shown in Figure 2.6.

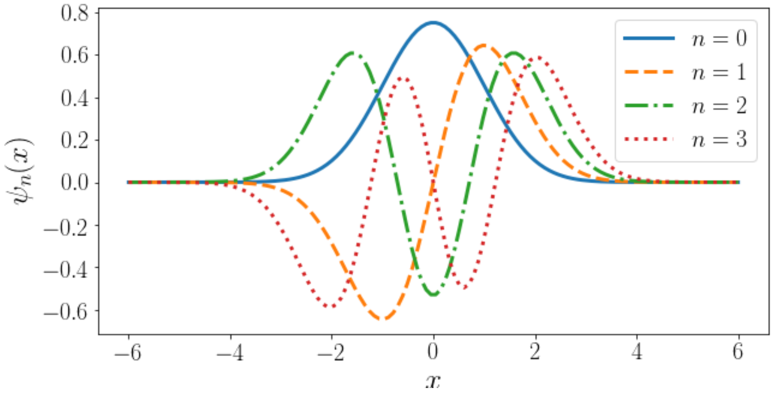

Figure 2.6: The first 4 Hermite-Gaussian functions given by Equation (2.3).

According to Johnston (2014),

$$\int_{-\infty}^{\infty} H_n(x)H_m(x)e^{-x^2}dx = \sqrt{\pi}2^n n!\mathbb{1}\{m = n\} \tag{2.5}$$

is a well known fact about the Hermite polynomials, where $\mathbb{1}\{A\}$ represents the indicator function of the event A (which is equivalent to the Kronecker delta function).

Therefore, we have by combining equations (2.3) and (2.5) that

$$\int_{-\infty}^{\infty} \psi_n(x)\psi_m(x)dx = \mathbb{1}\{m = n\}. \tag{2.6}$$

Furthermore, one can show that the set of Hermite-Gaussian functions forms a complete orthonormal basis of the set of all square-integrable real-valued functions, $L^2(\mathbb{R})$ (Johnston, 2014). One can also generalize the definition of the Hermite-Gaussian functions to have a general location, μ, and scale, σ:

$$\psi_n(x;\mu,\sigma) = \frac{1}{\sqrt{\sigma 2^n n!\sqrt{\pi}}}H_n\left(\frac{x-\mu}{\sigma}\right)e^{-\dfrac{(x-\mu)^2}{2\sigma^2}}. \tag{2.7}$$

By a simple change of variables, one can show that the set of generalized Hermite-Gaussian functions, $\psi_n(x;\mu,\sigma)$, also forms a complete orthonormal basis of $L^2(\mathbb{R})$ for any $\mu \in \mathbb{R}$

and any $\sigma \in \mathbb{R}^+$, the positive real numbers. Therefore, for such an $L^2(\mathbb{R})$ function g, we can decompose it as

$$g(x) = \sum_{n=0}^{\infty} c_n \psi_n(x; \mu, \sigma). \tag{2.8}$$

In this instance let $f(x)$ be a Gaussian with center μ and width σ, and let $g(x;\xi) = f(x) - f(\xi x)$ be the difference between $f(x)$ and its Doppler-shifted version. Decomposing this $g(x;\xi)$ as in Equation (2.8), we have Theorem 1, giving the approximation error when only $n = 1$ is used.

Theorem 1. *For any* $\sigma \in \mathbb{R}^+$ *and any* $\mu, \xi \in \mathbb{R}$ *and* $g(x;\xi) = \exp\left(-\frac{(x-\mu)^2}{2\sigma^2}\right) - \exp\left(-\frac{(\xi x-\mu)^2}{2\sigma^2}\right)$ *decomposed in the Hermite-Gaussian basis as* $g(x;\xi) = \sum_{n=0}^{\infty} c_n(\xi)\psi_n(x;\mu,\sigma)$,

$$\lim_{\xi \to 1} \frac{\int_{-\infty}^{\infty} \left(g(x;\xi) - c_1(\xi)\psi_1(x;\mu,\sigma)\right)^2 dx}{\int_{-\infty}^{\infty} \left(g(x;\xi)\right)^2 dx} = \frac{1}{1 + \frac{2\mu^2}{3\sigma^2}}. \tag{2.9}$$

Before proving Theorem 1, we interpret it in the context of stellar spectroscopy. It is well known that many absorption features in the spectrum of a star are described by the Voigt profile (Ciuryło, 1998; Gray, 2005), which is well approximated by a Gaussian for many absorption features in stellar spectra. It is also the case that the central wavelength, μ_x, is significantly larger than the width, σ_x, for each of these features. As an example, a typical wavelength in the visible spectrum is 5000 Å, and the largest features near this wavelength have a width that is upper-bounded by 0.5 Å; the maximum width of absorption features detected between 4700 Å and 5300 Å by the AFF algorithm for the data collected from 51 Pegasi by EXPRES was 0.366 Å with the 88'th quantile being 0.1 Å (more details to come in Section 5). For a feature with center 5000 Å and width 0.5 Å, the limit in Theorem 1 becomes 1.5×10^{-8}. Therefore the theorem implies that as ξ approaches 1 (i.e., at small values of RV), the proportion of the difference, $g(x;\xi)$, that remains to be modeled after using only ψ_1 *with the same width and center as the original Gaussian* is nearly zero. In other words, Doppler shifting a Gaussian absorption feature at a small RV is approximately the same as adding a constant multiple of ψ_1 (which is a scalar multiple of the Gaussian's derivative) to the feature. This is a special case of a well-known result: if a given function evaluates to zero at a given point, then the derivative is the leading term in the Taylor-expansion about that point.

Some of the RV detection algorithms, such as the template matching method described in Bouchy et al. (2001), attempt to model a Doppler shift by approximating the derivative of absorption features with a high S/N template spectrum. They then use a wavelength multiple of this derivative to create a nonlinear model of a Doppler shift with parameters to be fitted. At high wavelength values, though, rescaling across a narrow wavelength window is nearly the same as an additive shift. In fact, if the Doppler shift were additive, the limit in Theorem 1 would be 0. Furthermore, an additive shift removes the nonlinearity in the Doppler shift model. While this idea is not new (Butler et al., 1996), the approximation error of this has remained unknown. Therefore, Theorem 1 takes account of the wavelength rescaling nature of the Doppler shift, giving the value of this approximation error for assuming the shift to be additive at the limit of low values of RV.

To answer the question of how small an RV is small enough for this to be valid, we first state some Lemmas that solve for the coefficients in the decomposition shown in Equation (2.8) with $g(x;\xi)$ as defined in Theorem 1. Lemma 1 gives a useful recursive relationship of an integral quantity that arises in solving the coefficients.

Lemma 1. *For* $I_k(a,b,c) := \int_{-\infty}^{\infty} u^k e^{-\left(au^2+bu+c\right)} du$ *where* $a > 0$*, we have that*

$$I_0(a,b,c) = \sqrt{\frac{\pi}{a}} e^{\left(\frac{b^2}{4a} - c\right)}, \tag{2.10}$$

$$I_1(a,b,c) = -\frac{\sqrt{\pi}b}{2a^{3/2}} e^{\left(\frac{b^2}{4a} - c\right)}, \tag{2.11}$$

$$\text{and for all } k \geq 2,\ I_k(a,b,c) = -\frac{b}{2a} I_{k-1}(a,b,c) + \frac{k-1}{2a} I_{k-2}(a,b,c). \tag{2.12}$$

Proof. :

Choose constants $a \in \mathbb{R}^+$, $b, c \in \mathbb{R}$. Then, using integration by parts, we have that

$$I_1(a,b,c) = e^{\left(\frac{b^2}{4a} - c\right)} \left[\int_{-\infty}^{\infty} u e^{-au^2} du - \frac{b}{2a} \int_{-\infty}^{\infty} e^{-au^2} du \right] = -\frac{\sqrt{\pi}b}{2a^{3/2}} e^{\left(\frac{b^2}{4a} - c\right)} \quad . \tag{2.13}$$

$$I_0(a,b,c) = \int_{-\infty}^{\infty} e^{-\left(ax^2+bx+c\right)} dx = \frac{2a}{b} I_1(a,b,c) = \sqrt{\frac{\pi}{a}} e^{\left(\frac{b^2}{4a} - c\right)} \quad . \tag{2.14}$$

Now choose any $k \in \{n \in \mathbb{N} : n \geq 2\}$.

$$I_{k-1}(a,b,c) = \int_{-\infty}^{\infty} x^{k-1} e^{-ax^2} e^{-(bx+c)} dx \tag{2.15}$$

$$= \lim_{z \to \infty} \left[-\frac{1}{b} x^{k-1} e^{-\left(ax^2+bx+c\right)} |_{-z}^{z} \right] + \frac{1}{b} \int_{-\infty}^{\infty} \left((k-1)x^{k-2} - 2ax^k \right) e^{-\left(ax^2+bx+c\right)} dx \tag{2.16}$$

$$= \frac{k-1}{b} I_{k-2}(a,b,c) - \frac{2a}{b} I_k(a,b,c) \quad . \tag{2.17}$$

So we have that

$$I_k(a,b,c) = -\frac{b}{2a} I_{k-1}(a,b,c) + \frac{k-1}{2a} I_{k-2}(a,b,c). \tag{2.18}$$

□

Using $I_k(a, b, c)$ as defined in Lemma 1, Lemma 2 gives the mathematical solution for the coefficients.

Lemma 2. *For $g(x;\xi)$ as defined in Theorem 1 decomposed as $g(x;\xi) = \sum_{n=0}^{\infty} c_n(\xi)\psi_n(x;\mu,\sigma)$, and $I_k(a, b, c)$ as defined in Lemma 1, we have that for $\varepsilon = \xi - 1$*

$$c_0(\varepsilon) = \sqrt{\sigma\sqrt{\pi}} - \frac{1}{\sqrt{\sigma\sqrt{\pi}}} I_0\left(\frac{1+\varepsilon+\dfrac{\varepsilon^2}{2}}{\sigma^2}, -\frac{2\mu+\varepsilon\mu}{\sigma^2}, \left(\frac{\mu}{\sigma}\right)^2\right), \tag{2.19}$$

and for all $k \geq 1$,

$$c_k(\varepsilon) = -\sqrt{\frac{\sigma k! 2^k}{\sqrt{\pi}}} \sum_{m=0}^{\left\lfloor \frac{k}{2} \right\rfloor} \frac{(-1)^m}{4^m m!(k-2m)!} I_{k-2m}\left(1+\varepsilon+\frac{\varepsilon^2}{2}, \frac{\varepsilon\mu}{\sigma}(1+\varepsilon), \frac{1}{2}\left(\frac{\varepsilon\mu}{\sigma}\right)^2\right). \tag{2.20}$$

Proof. :

Since $g(x;\xi) = \sum_{n=0}^{\infty} c_n(\xi)\psi_n(x;\mu,\sigma)$ and $\psi_n(x;\mu,\sigma)$ are orthonormal, we have that

$$c_k(\xi) = \int_{-\infty}^{\infty} \psi_k(x;\mu,\sigma) g(x;\xi) dx\,. \tag{2.21}$$

Choose any $k \in \{n \in \mathbb{N} : n \geq 1\}$. By using Equation (2.4) for the k'th Hermite polynomial, we have that for $\varepsilon = \xi - 1$,

$$c_k(\varepsilon) = \int\limits_{-\infty}^{\infty} g(x;\varepsilon)\psi_k(x;\mu,\sigma)dx \tag{2.22}$$

$$= \sqrt{\sigma\sqrt{\pi}}\int\limits_{-\infty}^{\infty} \psi_0(x;\mu,\sigma)\psi_k(x;\mu,\sigma)dx - \int\limits_{-\infty}^{\infty} e^{-\frac{1}{2\sigma^2}(x-\mu+\varepsilon x)^2}\psi_k(x;\mu,\sigma)dx \tag{2.23}$$

$$= 0 - \int\limits_{-\infty}^{\infty} \frac{1}{\sqrt{\sigma 2^k k!\sqrt{\pi}}} H_k\left(\frac{x-\mu}{\sigma}\right) e^{-\frac{1}{2\sigma^2}\left[(x-\mu+\varepsilon x)^2+(x-\mu)^2\right]}dx \tag{2.24}$$

$$= -\frac{\sqrt{\sigma}}{\sqrt{2^k k!\sqrt{\pi}}}\int\limits_{-\infty}^{\infty} H_k(u)e^{-\frac{1}{2}\left[\left(u+\varepsilon\left(u+\frac{\mu}{\sigma}\right)\right)^2+u^2\right]}du \tag{2.25}$$

$$= -\frac{\sqrt{\sigma}}{\sqrt{2^k k!\sqrt{\pi}}}\int\limits_{-\infty}^{\infty} k!\sum_{m=0}^{\lfloor k/2\rfloor}\frac{(-1)^m}{m!(k-2m)!}(2u)^{k-2m}e^{-\frac{1}{2}\left[\left(2+2\varepsilon+\varepsilon^2\right)u^2+2\varepsilon\frac{\mu}{\sigma}(1+\varepsilon)u+\varepsilon^2\frac{\mu^2}{\sigma^2}\right]}du \tag{2.26}$$

$$= -\frac{\sqrt{\sigma k! 2^k}}{\sqrt{\sqrt{\pi}}}\sum_{m=0}^{\lfloor k/2\rfloor}\frac{(-1)^m}{m!(k-2m)!}\frac{1}{4^m}\int\limits_{-\infty}^{\infty} u^{k-2m}e^{-\frac{1}{2}\left[\left(2+2\varepsilon+\varepsilon^2\right)u^2+2\varepsilon\frac{\mu}{\sigma}(1+\varepsilon)u+\varepsilon^2\frac{\mu^2}{\sigma^2}\right]}du \tag{2.27}$$

$$= -\sqrt{\frac{\sigma k! 2^k}{\sqrt{\pi}}}\sum_{m=0}^{\lfloor k/2\rfloor}\frac{(-1)^m}{4^m m!(k-2m)!}I_{k-2m}\left(1+\varepsilon+\frac{\varepsilon^2}{2}, \frac{\varepsilon\mu}{\sigma}(1+\varepsilon), \frac{1}{2}\left(\frac{\varepsilon\mu}{\sigma}\right)^2\right) \tag{2.28}$$

For $k = 0$, the only difference is that the first integral in Equation (2.23) becomes 1 instead of vanishing. Therefore,

$$c_0(\varepsilon) = \sqrt{\sigma\sqrt{\pi}} - \frac{1}{\sqrt{\sigma\sqrt{\pi}}} I_0\left(\frac{1+\varepsilon+\frac{\varepsilon^2}{2}}{\sigma^2}, -\frac{2\mu+\varepsilon\mu}{\sigma^2}, \left(\frac{\mu}{\sigma}\right)^2\right) \tag{2.29}$$

□

Using Lemmas 1 and 2 we numerically calculate the first seven coefficients as a function of RV and illustrate the results in Figure 2.7. It is not hard to notice that all the coefficients go to 0 as the RV goes to 0. This is because with no RV, $g(x;\xi)$ as defined in Theorem 1 is the zero-function. More importantly, though, Figure 2.7 illustrates that as the RV approaches zero, the dominating coefficient is c_1.

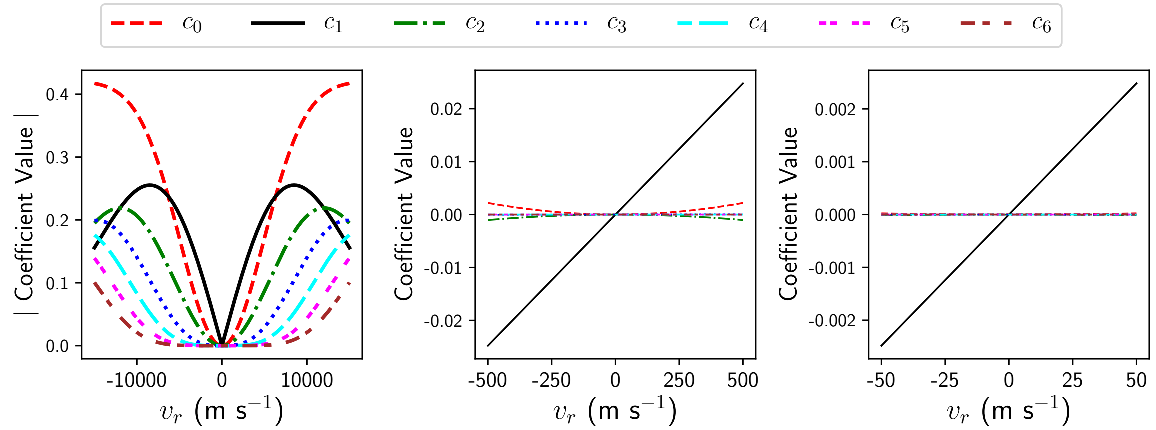

Figure 2.7: The coefficient solutions that result from modeling a Doppler-shifted Gaussian with the Hermite-Gaussian basis are plotted here as a function of v_r. The left panel has the absolute value of the coefficients on the vertical axis and illustrates that at low values of v_r, c_1 is the dominating coefficient. The middle and right panels show the exact coefficient value and illustrate that at low values of v_r, c_1 is nearly a constant multiple of it. Only the zero'th up to the sixth coefficients are shown. The Gaussian here has the parameters of $\mu = 5000$ and $\sigma = 0.1$ which is meant to represent a typical absorption feature in a stellar spectrum.

When v_r has a magnitude below 100 m s^{-1} it appears that all other coefficients besides c_1 are negligible, with c_0 and c_2 being the only possible exceptions. Furthermore, at velocities with a magnitude below 500 m s^{-1}, c_1 is approximately linear as a function of v_r. Since Figure 1.4 illustrates that a considerable number of currently known exoplanets exert a RV on their host star with a semi-amplitude less than 100 m s^{-1}, which is especially true for Earth-like exoplanets, it suggests that it is not unreasonable to ignore all Hermite-Gaussian coefficients besides c_1 in modeling a Gaussian absorption feature that is Doppler-shifted due to an exoplanet.

Now that we have the coefficient solutions, and have a sense that c_1 is the most dominant coefficient at values of RV that are of interest, we calculate the approximation error made by ignoring all other coefficients. To do so, we introduce a new quantity that we refer to as the standardized approximation error, which appears in Theorem 1. For a function φ approximated by the function ϕ, define the standardized approximation error $D(\phi||\varphi)$ as

$$D(\phi||\varphi) = \frac{\int_{-\infty}^{\infty} \left(\varphi(x) - \phi(x)\right)^2 dx}{\int_{-\infty}^{\infty} \varphi(x)^2 dx} \,. \tag{2.30}$$

In a sense, $D(\phi||\varphi)$ gives the proportion of the squared function φ that remains to be modeled after approximating with ϕ. In our case we consider $D\left(g(x;\xi)||c_1(\xi)\psi_1(x;\mu,\sigma)\right)$.[2] Lemmas 3 and 4 help us solve for the limit as ξ approaches 1 (i.e., as v_r approaches 0).

Lemma 3. *For $g(x;\xi)$ as defined in Theorem 1 decomposed as $g(x;\xi) = \sum\limits_{n=0}^{\infty} c_n(\xi)\psi_n(x;\mu,\sigma)$, we have that*

$$D\left(g(x;\xi)||c_1(\xi)\psi_1(x;\mu,\sigma)\right) = 1 - \frac{c_1^2(\xi)}{\int_{-\infty}^{\infty} \left(g(x;\xi)\right)^2 dx}. \tag{2.31}$$

Proof. :

Decompose as $g(x;\xi) = \sum\limits_{n=0}^{\infty} c_n(\xi)\psi_n(x;\mu,\sigma)$.

Then

$$\int_{-\infty}^{\infty} \left(g(x;\xi) - c_1(\xi)\psi_1(x;\mu,\sigma)\right)^2 dx \tag{2.32}$$

---

[2] Since $g(x;\xi)$ approaches the zero function as $\xi \to 1$, and for any $k \geq 0$ $c_k(\xi) \to 0$ as $\xi \to 1$, the ordinary approximation error of using any individual k would approach 0. This would tell us nothing about the relative magnitudes of the Hermite-Gaussian coefficients. The denominator of $D\left(g(x;\xi)||c_1(\xi)\psi_1(x;\mu,\sigma)\right)$ adjusts for this by standardizing the quantity.

$$= \int_{-\infty}^{\infty} (g(x;\xi))^2 dx - 2c_1(\xi) \int_{-\infty}^{\infty} g(x;\xi)\psi_1(x;\mu,\sigma) dx + c_1^2(\xi) \int_{-\infty}^{\infty} \psi_1^2(x;\mu,\sigma) dx \tag{2.33}$$

$$= \int_{-\infty}^{\infty} (g(x;\xi))^2 dx - 2c_1^2(\xi) + c_1^2(\xi) = \int_{-\infty}^{\infty} (g(x;\xi))^2 dx - c_1^2(\xi) \tag{2.34}$$

□

Lemma 4. $\lim_{\xi \to 1} \dfrac{c_1^2(\xi)}{\int_{-\infty}^{\infty} \left(g(x;\xi)\right)^2 dx} = \dfrac{1}{1 + \dfrac{3\sigma^2}{2\mu^2}}$.

Proof. :

From Lemmas 1 and 2 we have that, with $\varepsilon = \xi - 1$,

$$c_1^2(\varepsilon) = \varepsilon^2 (1+\varepsilon)^2 h(\varepsilon) \tag{2.35}$$

where

$$h(\varepsilon) := \frac{4\sqrt{\pi}\mu^2}{\sigma} \frac{1}{\left(2 + 2\varepsilon + \varepsilon^2\right)^3} e^{-\left(\frac{\mu}{\sigma}\right)^2 \frac{\varepsilon^2}{2 + 2\varepsilon + \varepsilon^2}} . \tag{2.36}$$

We also have that

$$\frac{\partial}{\partial \varepsilon} c_1^2(\varepsilon) = \left(4\varepsilon^3 + 6\varepsilon^2 + 2\varepsilon\right) h(\varepsilon) + \varepsilon^2 (1+\varepsilon)^2 \frac{\partial h(\varepsilon)}{\partial \varepsilon} \tag{2.37}$$

and

$$\frac{\partial^2}{\partial \varepsilon^2} c_1^2(\varepsilon) = \left(12\varepsilon^2 + 12\varepsilon + 2\right) h(\varepsilon) + 2\left(4\varepsilon^3 + 6\varepsilon^2 + 2\varepsilon\right) \frac{\partial h}{\partial \varepsilon} + \varepsilon^2 (1+\varepsilon)^2 \frac{\partial^2 h}{\partial \varepsilon^2} . \tag{2.38}$$

Since $h(\varepsilon)$, $\frac{\partial h}{\partial \varepsilon}$, and $\frac{\partial^2 h}{\partial \varepsilon^2}$ are all continuous at 0, we have that

$$\lim_{\varepsilon \to 0} c_1^2(\varepsilon) = 0, \tag{2.39}$$

$$\lim_{\varepsilon \to 0} \frac{\partial}{\partial \varepsilon} c_1^2(\varepsilon) = 0, \tag{2.40}$$

$$\text{and } \lim_{\varepsilon \to 0} \frac{\partial^2}{\partial \varepsilon^2} c_1^2(\varepsilon) = 2 \lim_{\varepsilon \to 0} h(\varepsilon) = \frac{\sqrt{\pi}\mu^2}{\sigma}. \tag{2.41}$$

With $g(x; \mu, \sigma)$ as in Lemma 2, we have that

$$\int_{-\infty}^{\infty} g^2(x;\xi)dx = \int_{-\infty}^{\infty} e^{-\frac{(x-\mu)^2}{\sigma^2}} dx + \int_{-\infty}^{\infty} e^{-\frac{(\xi x-\mu)^2}{\sigma^2}} dx - 2\int_{-\infty}^{\infty} e^{-\frac{1}{2\sigma^2}\left(\left(1+\xi^2\right)x^2 - 2\mu(1+\xi)x + 2\mu^2\right)} dx \tag{2.42}$$

$$= \sigma\sqrt{\pi} + \frac{\sigma}{\xi}\sqrt{\pi} - 2e^{-\frac{\mu^2}{\sigma^2}\left(1 - \frac{(1+\xi)^2}{2\left(1+\xi^2\right)}\right)} \int_{-\infty}^{\infty} e^{-\frac{1+\xi^2}{2\sigma^2}\left(x - \frac{\mu(1+\xi)}{1+\xi^2}\right)^2} dx \tag{2.43}$$

$$= \sigma\sqrt{\pi}\left(1 + \frac{1}{\xi} - \frac{2^{3/2}}{\sqrt{1+\xi^2}} e^{-\frac{\mu^2}{\sigma^2}\left(1 - \frac{(1+\xi)^2}{2\left(1+\xi^2\right)}\right)}\right) \tag{2.44}$$

$$= \sigma\sqrt{\pi}\left(1 + \frac{1}{1+\varepsilon} - \frac{2^{3/2}}{\sqrt{2+2\varepsilon+\varepsilon^2}} e^{-\frac{\mu^2}{2\sigma^2}\frac{\varepsilon^2}{2+2\varepsilon+\varepsilon^2}}\right) \tag{2.45}$$

Therefore, $\lim_{\varepsilon \to 0} \int_{-\infty}^{\infty} g^2(x;\varepsilon)dx = 0$. Furthermore, we have that

$$\frac{\partial}{\partial \varepsilon} \int_{-\infty}^{\infty} g^2(x;\varepsilon)dx = \sigma\sqrt{\pi}\left[-\frac{1}{(1+\varepsilon)^2} + 2^{3/2}\left(\left(2+2\varepsilon+\varepsilon^2\right)^{-3/2}(1+\varepsilon) + \frac{\mu^2}{\sigma^2}\left(2+2\varepsilon+\varepsilon^2\right)^{-5/2}\left(2\varepsilon+\varepsilon^2\right)\right) e^{-\frac{\mu^2}{2\sigma^2}\frac{\varepsilon^2}{2+2\varepsilon+\varepsilon^2}}\right]. \tag{2.46}$$

Hence,

$$\lim_{\varepsilon \to 0} \frac{\partial}{\partial \varepsilon} \int_{-\infty}^{\infty} g^2(x;\varepsilon)dx = 0. \tag{2.47}$$

Defining

$$h(\varepsilon) := 2^{3/2} \left(\left(2 + 2\varepsilon + \varepsilon^2\right)^{-3/2} (1+\varepsilon) + \frac{\mu^2}{\sigma^2} \left(2 + 2\varepsilon + \varepsilon^2\right)^{-5/2} \left(2\varepsilon + \varepsilon^2\right) \right), \tag{2.48}$$

we have that $h(\varepsilon)$ is continuous and differentiable at 0.

Therefore, since

$$\lim_{\varepsilon \to 0} e^{-\frac{\mu^2}{2\sigma^2} \frac{\varepsilon^2}{2 + 2\varepsilon + \varepsilon^2}} = 1 \tag{2.49}$$

and

$$\lim_{\varepsilon \to 0} \frac{\partial}{\partial \varepsilon} e^{-\frac{\mu^2}{2\sigma^2} \frac{\varepsilon^2}{2 + 2\varepsilon + \varepsilon^2}} = 0, \tag{2.50}$$

we have that

$$\lim_{\varepsilon \to 0} \frac{\partial}{\partial \varepsilon} \left(h(\varepsilon) e^{-\frac{\mu^2}{2\sigma^2} \frac{\varepsilon^2}{2 + 2\varepsilon + \varepsilon^2}} \right) = \lim_{\varepsilon \to 0} \frac{\partial h(\varepsilon)}{\partial \varepsilon}. \tag{2.51}$$

Since

$$\lim_{\varepsilon \to 0} \frac{\partial}{\partial \varepsilon} \left(\left(2 + 2\varepsilon + \varepsilon^2\right)^{-3/2} (1+\varepsilon) \right) = -3 \cdot 2^{-5/2} + 2^{-3/2} \tag{2.52}$$

and

$$\lim_{\varepsilon \to 0} \frac{\partial}{\partial \varepsilon} \left(\left(2 + 2\varepsilon + \varepsilon^2\right)^{-5/2} \left(2\varepsilon + \varepsilon^2\right) \right) = 2^{-3/2}, \tag{2.53}$$

we have that

$$\lim_{\varepsilon \to 0} \frac{\partial h(\varepsilon)}{\partial \varepsilon} = \frac{\mu^2}{\sigma^2} - \frac{1}{2}. \tag{2.54}$$

And since

$$\lim_{\varepsilon \to 0} \frac{\partial}{\partial \varepsilon} \left(\frac{-1}{(1+\varepsilon)^2} \right) = 2, \tag{2.55}$$

we have from Equation (2.46) that

$$\lim_{\varepsilon\to 0}\frac{\partial^2}{\partial\varepsilon^2}\int\limits_{-\infty}^{\infty} g^2(x;\varepsilon)dx = \frac{3\sigma\sqrt{\pi}}{2}+\frac{\sqrt{\pi}\mu^2}{\sigma}\,. \tag{2.56}$$

So

$$\lim_{\varepsilon\to 0}\frac{c_1^2(\varepsilon)}{\int\limits_{-\infty}^{\infty} g^2(x;\varepsilon)dx} = \frac{\dfrac{\sqrt{\pi}\mu^2}{\sigma}}{\dfrac{\sqrt{\pi}\mu^2}{\sigma}+\dfrac{3\sigma\sqrt{\pi}}{2}} = \frac{1}{1+\dfrac{3\sigma^2}{2\mu^2}}. \tag{2.57}$$

□

Combining Lemmas 3 and 4 completes the proof of Theorem 1.

Theorem 1 does not explicitly give a rate at which the standardized approximation error approaches its limit. But by using Lemma 3 and Equation (2.45) from the proof of Lemma 4, we illustrate the rate with Figure 2.8. Note that the standardized approximation error shown here is bounded between 0 and 1, and that the limit is actually non-zero. Figure 2.8 illustrates that as $\xi \to 1$, $D\left(g(x;\xi)||c_1(\xi)\psi_n(x;\mu,\sigma)\right)$ approaches its limit quadratically and that when $v_r < 50$ m s^{-1}, the standardized approximation error is less than 2.5×10^{-5} away from the limiting value.

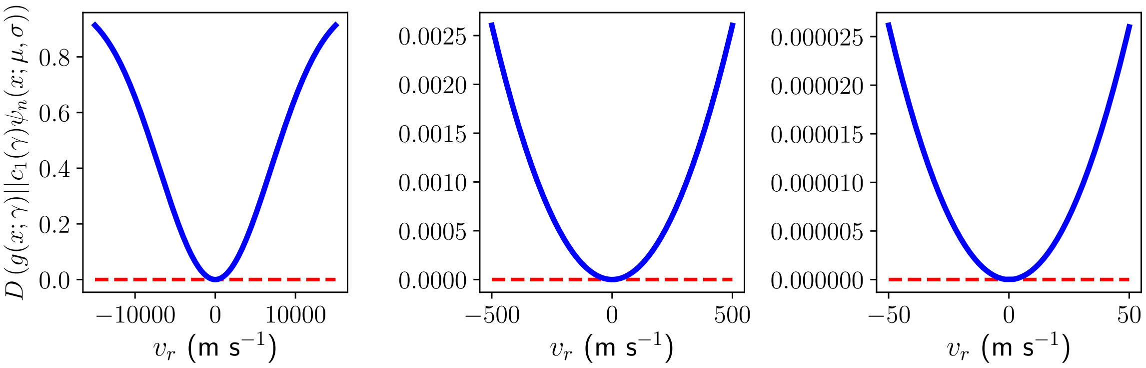

Figure 2.8: The standardized approximation error $D\left(g(x;\xi)||c_1(\xi)\psi_n(x;\mu,\sigma)\right)$ in Theorem 1 as a function of v_r with parameters $\mu = 5000$ and $\sigma = 0.1$ is plotted in bold. The limit is also shown in the horizontal red dashed line.

2.3.2 RV Estimation Method

Theorem 1 suggests a natural new method for detecting a Doppler shift in the spectrum of a star. As long as the magnitude of v_r is small enough, the absorption feature is approximately Gaussian, and the ratio μ/σ for the feature is large enough, we can do a least-squares fitting of the first-degree Hermite-Gaussian function to the difference between a template spectrum and a Doppler-shifted spectrum and map the fitted coefficient to a RV. As illustrated in Figure 2.7, c_1 at low values of v_r is directly proportional to v_r.

According to Lemma 2, $c_1(\varepsilon) = \frac{\sqrt{\sqrt{\pi}}}{\sqrt{2\sigma}}\varepsilon\mu(1+\varepsilon)\tilde{h}(\varepsilon)$, and $\lim_{\varepsilon\to 0}\frac{\partial}{\partial\varepsilon}c_1(\varepsilon) = \frac{\mu\sqrt{\sqrt{\pi}}}{\sqrt{2\sigma}}$.

Furthermore, using Equation (2.2) with $\varepsilon = \xi - 1$, we have that the mapping from ε to RV is $v_r(\varepsilon) = c\varepsilon$ and $\lim_{\varepsilon\to 0}\frac{\partial}{\partial\varepsilon}v_r(\varepsilon) = c$. Hence, $\lim_{\varepsilon\to 0}\frac{\partial}{\partial v_r}c_1\left(v_r(\varepsilon)\right) = \frac{\mu\sqrt{\sqrt{\pi}}}{c\sqrt{2\sigma}}$ which is the desired proportionality constant. So the proportionality that is valid at low values of RV, v_r, is

$$c_1 = \frac{\mu\sqrt{\sqrt{\pi}}}{c\sqrt{2\sigma}}v_r\ . \tag{2.58}$$

The strongest assumption made when applying the theorem is that the absorption features are Gaussian shaped. Because this is never exactly true, we analyze this model misspecification further in Section 2.3.4 below.

2.3.3 Extension to multiple features

Since a single absorption feature is unable to give a RV estimate that is precise enough, we need to use as many features in the spectrum as possible. Instead of fitting only a single first-degree Hermite-Gaussian function to the difference spectrum, we fit a sum of these functions to it. To construct this sum, we note that it must take into account the fact that differing absorption features will have different centers, widths, and depths. The generalized Hermite-Gaussian functions in Equation (2.7) can take account of the different centers and widths. Furthermore, according to Equation (2.21) in the proof of Lemma 2, Doppler-shifting a Gaussian with any amplitude simply multiplies the resulting coefficients by the same amplitude. In the case of stellar spectra, this amplitude is simply the line depth. Therefore, using Equation (2.58), the resulting model of the difference flux at pixel i, y_i, as a function of wavelength, x_i, to be fitted becomes

$$y_i = v_r \sum_{j=1}^{n} \frac{\sqrt{\sqrt{\pi} d_j \mu_j}}{c\sqrt{2\sigma_j}} \psi_1\left(x_i; \mu_j, \sigma_j\right) + \varepsilon_i, \tag{2.59}$$

where the sum is over all n absorption features, d_j represents the line depth of the j'th feature, and each ε_i is independent with expectation 0.

In practice, we assume that $\varepsilon_i \sim N\left(0, \varrho_i^2\right)$ and is independent for each i. Many modern stellar spectra come with uncertainties for each pixel's normalized flux.[3] This is particularly true for the normalized spectra from EXPRES that we analyze here. EXPRES estimates the uncertainty in each pixel by assuming the unnormalized flux is Poisson, estimating the red noise, and accounting for intrinsic effects of flat-fielding (Petersburg et al., 2020). Therefore, we assume that the provided uncertainties, $\hat{\varrho}_i$, are accurate estimates of each ϱ_i, and estimate v_r in Equation (2.59) through weighted least squares with weights $w_i = 1/\hat{\varrho}_i^2$.

To calculate the difference flux, y_i, at pixel i we need a template spectrum. Here we use the estimated template calculated from the set of observed spectra (see Section 2.3.5 for more details).

Since Equation (2.58) approximately holds for $v_r < 500$ m s^{-1}, which well encompasses most exoplanets of interest, we have a new Hermite-Gaussian based Radial Velocity (HGRV) estimation method. For a spectrum of Gaussian absorption features, we can create a linear model of the difference spectrum due to a Doppler-shift as a function of the sum of ψ_1 functions as given by Equation (2.59), the coefficient of which is the RV. Therefore, we have reduced the Doppler shift estimation problem to linear regression with no inter-

---

[3] If these uncertainties are not provided, weights can be defined using the standard assumption that the raw flux is Poisson. That is, the weights can be set to $w_i = \frac{\mathrm{cont}_i}{\hat{\tau}_i}$ where cont_i is the value of the raw continuum used for normalization at pixel i and $\hat{\tau}_i$ is the value of the estimated template.

cept. This method does not fundamentally require interpolation[4], treats neighboring pixels similarly, accounts for the hetroskedastic noise, and easily allows for obtaining the standard error of the estimated RV for statistical inference.

2.3.4 Model Misspecification

The HGRV method assumes that the shape of absorption features is Gaussian, which does not hold exactly. Various reasons are understood to contribute to this: a line following the Voigt profile may have a non-negligible Lorentzian component, the line may be deep enough to depart from the Voigt profile, or there may be additional effects in the star's atmosphere that are not well-encompassed by current physical models.

Since the HGRV method assumes Gaussian shaped absorption features, we now investigate the effects of applying it to non-Gaussian shaped features. We consider the absorption feature in the NSO spectrum between 5243.7 and 5244.2 Å. This feature is shown in the left panel of Figure 2.9, along with its best-fit Gaussian. For 50 equally spaced values of RV from 1 to 100 m s^{-1} we Doppler shift this feature according to Equation (2.2), use cubic splines to interpolate back to the original wavelength solution (Mészáros and Prieto, 2013), and fit the difference flux with the HGRV model from Equation (2.59) (with $n = 1$ and d, μ, and σ as the estimated parameters from the best-fit Gaussian). The ratio between the estimated and true RV is shown in the right panel of Figure 2.9.

Figure 2.9 illustrates that for this particular absorption feature, the HGRV method slightly overestimates the RV. For example, if the true RV is 1 m s^{-1}, this bias would be approximately 0.5 cm s^{-1}. Similarly, for a true RV of 100 m s^{-1} the bias would be less than 0.4 m s^{-1}.

Following the same procedure, we considered 100 additional absorption features to analyze the effect of misspecifying their profile as Gaussian, five of which are displayed below

---

[4] Interpolation is, however, used later on a high S/N, oversampled estimate of the template spectrum to give it the same wavelength solution as each observed spectrum so that the difference flux can be calculated.

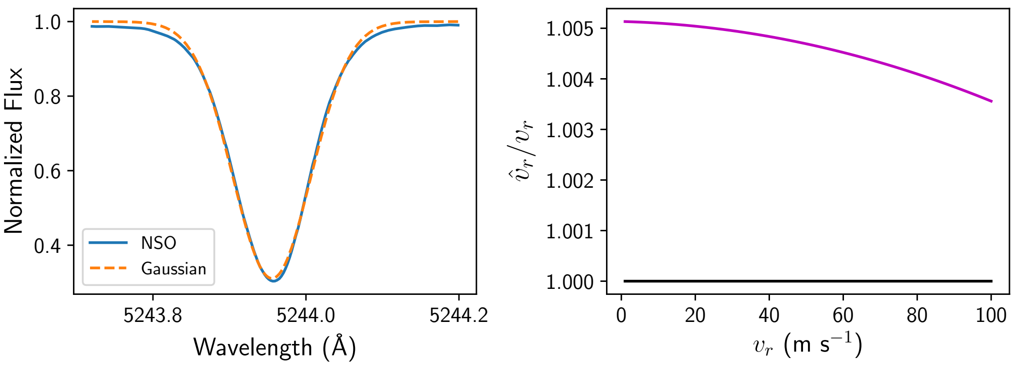

Figure 2.9: Results for analyzing the effects of misspecifying the model of the absorption feature in the NSO spectrum between 5243.7 and 5244.2 Å as a Gaussian. The left panel shows the feature in solid blue and the best-fit Gaussian in dashed orange. The right panel shows the ratio of the RV estimated with Equation (2.59) $\hat{v}_r$ (with $n = 1$) and the true RV, v_r.

in Figure 2.10. A Gaussian density shape is fit to each absorption feature, which is then Doppler-shifted by 50 equally spaced values of RV from 1 to 100 m s^{-1}. The RV is then estimated using the HGRV method. Most, but not all, of the additional features we analyzed lead to a slight overestimate of the RV. But for all 100 of these additional features, the difference for a 1 m s^{-1} RV is less than 1 cm s^{-1} away from the truth. Furthermore, the simulations in Section 2.4.2 below indicate that when combining the lines in the HGRV method, the overall bias is not greater than with individual lines.

2.3.5 Nonparametric Template Estimation

Since the HGRV method models the difference in normalized flux, we need to have a template spectrum that approximates the quiet spectrum of a star with no stellar activity. In principal, if one knows the approximate effective temperature, surface gravitational acceleration, metallicity, microturbulent velocity, and the elemental abundances of the star with high precision, a synthetic spectrum could be produced at the proper resolution to give such a template (Sneden et al., 2012). However, in practice, these stellar parameters and the atomic line transition data are not known well enough to make this feasible. Therefore, we

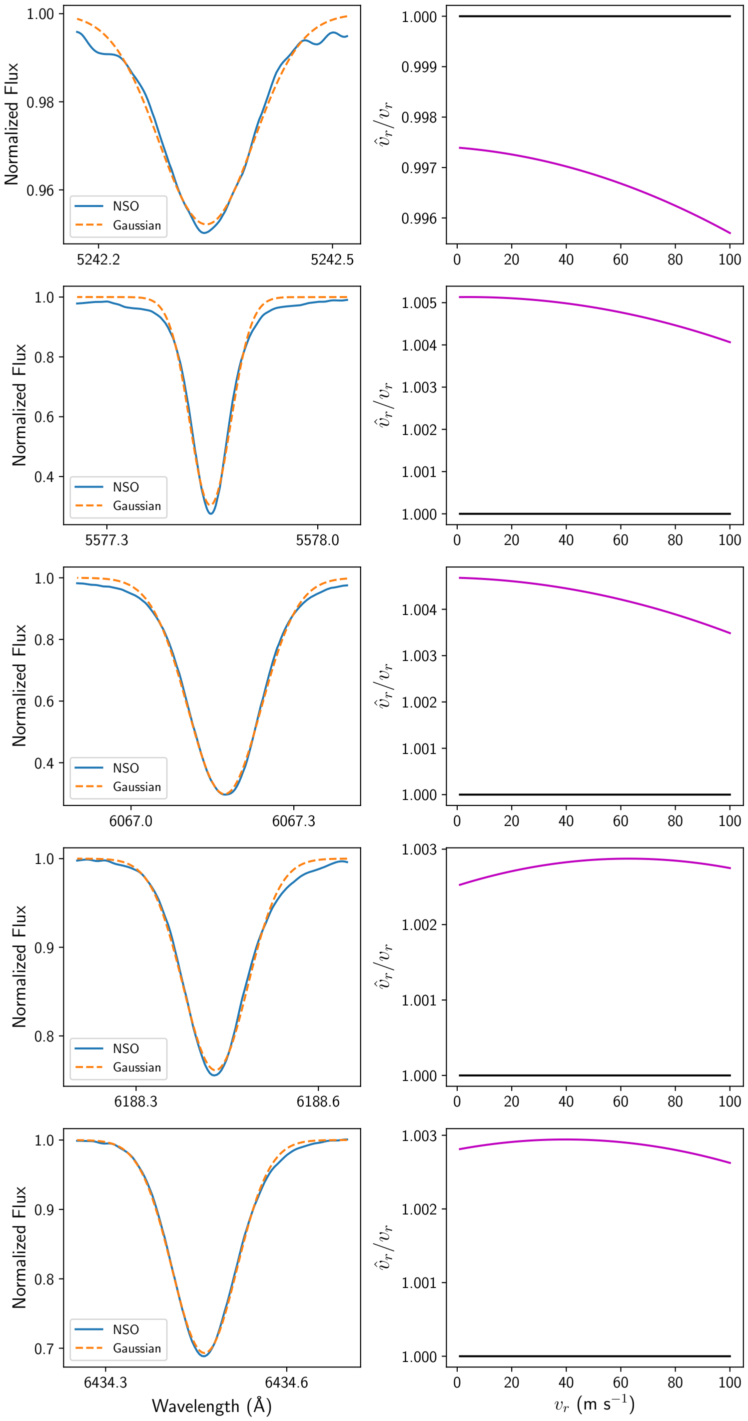

Figure 2.10: Results for analyzing the effects of misspecifying the model of five different absorption features in the NSO spectrum as a Gaussian. The left panels show the feature in solid blue and the best fitted Gaussian in dashed orange. The right panels show the ratio of the RV estimated with Equation (2.59) $\hat{v}_r$ (with $n = 1$) and the true RV v_r.

take a data-driven approach.

The method we propose for estimating the template is to combine all normalized, barycentric corrected, observed spectra across time epochs and fit a smooth curve to estimate a representative spectrum. The time sampling of the spectra can affect how well the estimated template approximates the true template. For example, two of the possible extremes in the sampling are if all the observations are at the same orbital phase or if the observations are uniform across all phases. The estimated template under these extremes are not likely to affect the end result of the HGRV approach so this template estimation method is sufficient for our purposes.[5]

All observed spectra are combined together, and we fit a local regression curve to this combined spectrum with a Gaussian kernel. We use local quadratic, instead of local linear, regression in order to better model the cores of absorption features. In practice we only fit at most 8 Å of the combined spectrum at a time, choosing an optimal bandwidth through generalized cross-validation for each section. This allows the computation to be parallelized. It also allows the bandwidth to be locally adaptive and take account of how absorption features are narrower on the blue end of the spectrum compared to the red end. An advantage of this approach is that when combining all observed spectra the wavelength solutions do not need to match across epochs, further minimizing the role of interpolation.

---

[5] Using this template estimation approach with time sampling that is approximately uniform across all phases of an exoplanet's orbit may lead to slightly broader features in the estimated template. However, broadening tends to be primarily an even effect and so would not significantly hinder the RV estimation using the HGRV method, which fits an odd function (ψ_1) to the difference flux in Equation (2.59). Time sampling carried out in such a way that the observations occur at approximately the same phase of an exoplanet's orbit should not have this broadening of features. However, a constant RV offset may be present between the estimated template spectrum and all observed spectra. Because the same estimated template is used for each observation and only relative RV estimates are needed, this offset should not influence the fitted orbital parameters.

2.4 Simulation Studies

This section includes two simulation studies based on the proposed methodology. The first is related to the template estimation approach, and the second compares properties of the RV estimation using the HGRV method with those of the commonly used CCF method.

2.4.1 Template Estimation

A nice feature of the HGRV approach is that no pre-specified template is required because the template spectrum is estimated from the full time-series of spectra using local quadratic regression (see Section 2.3.5). The estimated template contains both bias and variance, and we investigate the overall root mean squared error (RMS) through simulation. Furthermore, we consider how the RMS changes with the number of spectra and the S/N. Finally, we explore how the time-sampling cadence affects the estimated template.

For a star's true template with normalized flux τ, and estimated template with normalized flux $\hat{\tau}$, we define the RMS as

$$\mathrm{RMS}\left(\hat{\tau}\right) = \sqrt{\frac{1}{n}\sum_{i=1}^{n}(\tau_i - \hat{\tau}_i)^2}. \tag{2.60}$$

For our simulation we use a version of the NSO spectrum that we smooth through local quadratic regression that approximately represents the quiet solar spectrum with infinite S/N. We also use cubic spline interpolation to give this smoothed NSO spectrum the same wavelength solution as the 51 Pegasi spectrum observed by EXPRES on Julian Day (JD) 2458641.952. For a given number of observed spectra, N, each with a given S/N, our simulation consists of the following steps: (i) sample time epochs $t_1, ..., t_N$ where $t_k \sim \mathrm{iid\ Uniform}(0, 2\pi)$, (ii) calculate RV's $v_{r,1}, ..., v_{r,N}$ where $v_{r,k} = 10\mathrm{sin}(t_k)$, (iii) simulate N observed spectra with wavelength axis Doppler-shifted using Equation (2.2) with RV $v_{r,k}$, and normalized flux axis with independent Poisson noise at the given S/N (where the noise is added to the un-normalized flux), (iv) apply the template estimation method described in Section 2.3.5 and calculate the resulting RMS($\hat{\tau}$).

In our simulations, the number of spectra, N, ranges from 1 to 31 (in steps of 2) and the S/N ranges from 100 to 250 (in steps of 10). For each pair of values we perform the simulation 50 independent times and calculate the average, and standard deviation, of the RMS. Each of these 50 represents a different cadence. For computational purposes we do not use the entire spectrum for this simulation. Instead, we use the wavelength window $5240 - 5245$ Å for our simulation. We also ran the same simulation on the wavelength window $4965 - 4970$ Å which has a higher density of absorption features, as well as the window $6381 - 6386$ Å which has a lower absorption feature density. The results for these additional windows are similar to the first window. The results for the window $5240 - 5245$ Å are summarized in Figure 2.11 which shows the average RMS($\hat{\tau}$) on the left panel, and the standard deviation of the RMS($\hat{\tau}$) on the right, for each pair of S/N and number of spectra.[6]

The left plot in Figure 2.11 illustrates that once the number of spectra reaches approximately 21, the average RMS($\hat{\tau}$) of the estimated template is below approximately 0.001 (which represents a S/N of about 1000) for any S/N above 100. On the other hand, if all observed spectra had a S/N above 200 (which is often true of EXPRES spectra), one would only need about 11 spectra to reach this template estimation precision. Furthermore, by examining the differences between the true template and individual instances of an estimated template, the residuals showed no obvious systematic bias within the wavelength bounds of absorption features. The same plot also shows that the RMS($\hat{\tau}$) is more affected by the number of spectra than the S/N in this example. Figure 2.12 shows how the RMS indicated

---

[6] The results of this simulation did not change significantly when calculating the RMS using only the portion of the spectrum that lies inside the wavelength intervals corresponding to absorption features as given by the AFF algorithm. For instance, with a S/N of 200 and 20 observed spectra, the original RMS was 0.00078 ± 0.00003, whereas the RMS on only the portion of the spectrum pertaining to absorption features was 0.00079 ± 0.00003.

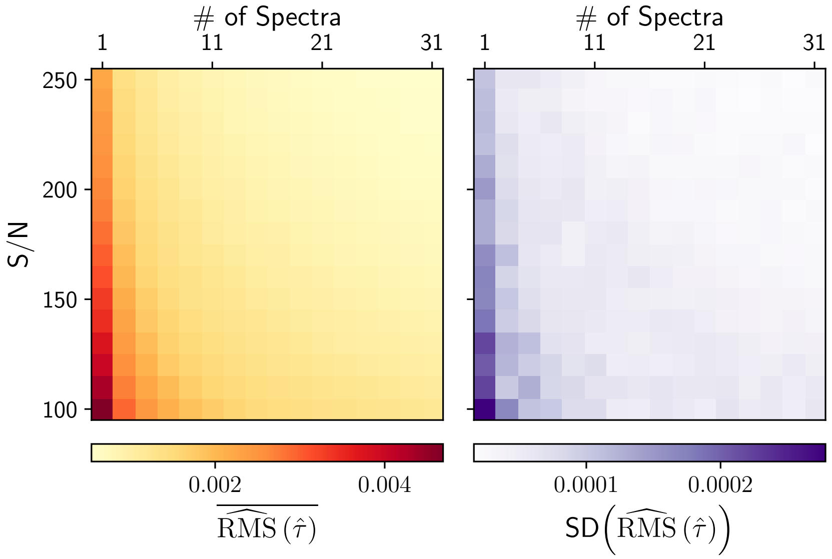

Figure 2.11: Simulation study results for estimating the template spectrum between 5240 and 5245 Å. For each S/N and number of spectra, N, 50 simulations were carried out each with a different cadence. Each simulation involved estimating the template with local quadratic regression and calculating the RMS. The left plot shows the average, and the right plot shows the standard deviation, of the RMS across the 50 simulations for each pair of S/N and N. The plots share the same vertical-axis.

on the colorbar of the left plot in Figure 2.11 maps to an effective S/N of the estimated template.

The right plot in Figure 2.11 illustrates how the RMS$(\hat{\tau})$ varies due to the differing cadences in the 50 samples used for each pair of S/N and number of spectra. The simulation suggests that, as expected, the greatest differences are found when using only one spectrum. The variation is minimal for 11 or more spectra and a S/N above 150.

We next investigate how the HGRV-estimated RV changes when using an estimated template instead of the true template. We first note that there are two main sources of a difference in the estimated RV due to template estimation for this simulation study design: (i) finite S/N of the estimated template and (ii) shape changes of absorption features due to the nonparametric smoothing and the changing cadence. The second source is what we investigate here. Since each of the observed spectra has a different RV, they all will be slightly shifted with respect to the true template and each other. Depending on the cadence,

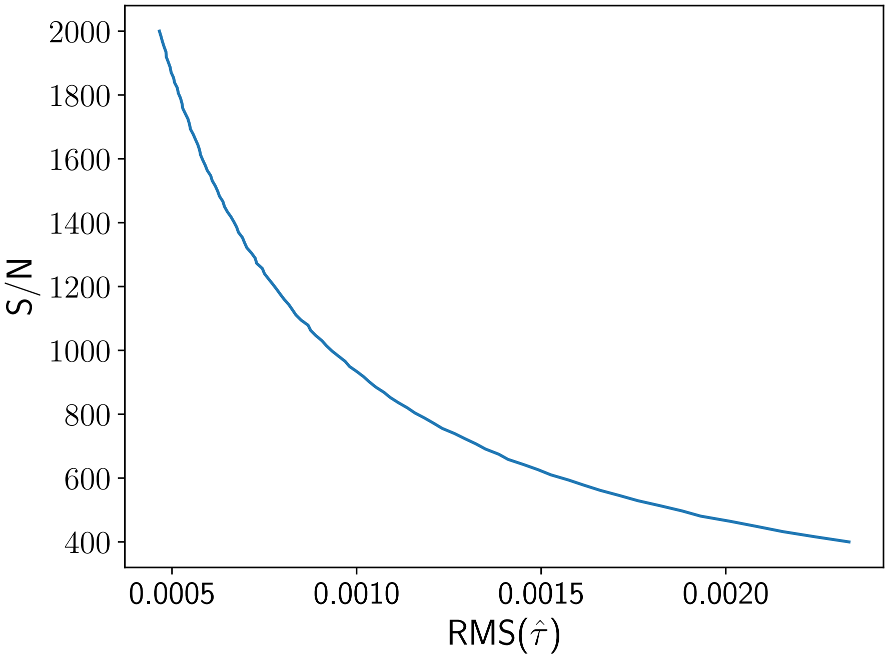

Figure 2.12: The estimated effective S/N of a spectrum as a function of the RMS as defined in Equation (2.60).

this could lead the estimated template to have some shift relative to the true template and have slightly broader absorption features. Furthermore, the bias of nonparametric smoothing may also broaden the shape of absorption features. Since the same estimated template is used for each observation, a shift with respect to the true template would only result in a constant offset of all RV's. Since this constant offset can be accounted for and removed, it is not problematic.

To see how such shape changes might influence the variance of the estimated RV, we apply a procedure similar to the one used to produce Figure 2.11. With the number of observed spectra set to 20 and a S/N of $80,000$ (essentially infinite) we simulate 50 sets of observations, each with a randomly-sampled cadence. The final result of this is a set of 50 different estimated templates with the dominant difference from the true template being the possible shape changes described above.

For each of these 50 estimated templates we use the true template to generate an observed spectrum with S/N of 300 and a 10 m s^{-1} Doppler shift. To understand how the shape changes affect the variance of the RV estimate, we calculate the difference flux using the true template and this observed spectrum. The HGRV method then returns an estimated RV for each of these 50. Using the same set of 50 observed spectra, this process is then repeated with the estimated templates in place of the true template. Each observed spectrum then has two RV estimates: one from the true template and one from an estimated template. We find that the standard deviation of the RV estimates that used the true template differs only by approximately 0.001 m s^{-1} from the standard deviation of the RV estimates that used the estimated templates. This suggests that the effect of shape changes on the variance of the estimated RV due to nonparametric smoothing and differing cadences is negligible. Furthermore, we find that the estimated relative RV differs in magnitude by approximately 0.006 m s^{-1} on average when using the estimated templates instead of the true template.

2.4.2 RV Estimation

To investigate the accuracy of the HGRV method, especially at low velocities, we simulate spectra with a known RV and estimate the RMS of $\hat{v}_r$. By design, this simulation ignores astrophysical effects on RV-precision from stellar activity, analyzing the error contribution from modeling alone. To estimate this RMS, we use

$$\widehat{\mathrm{RMS}}\left(\hat{v}_r\right) = \sqrt{\frac{1}{n}\sum_{i=1}^{n}\left(\hat{v}_{r,i} - v_r\right)^2} \tag{2.61}$$

where n is the number of simulations at RV v_r. The square of $\widehat{\mathrm{RMS}}\left(\hat{v}_r\right)$ can be decomposed into the sum of the variance and squared bias of $\hat{v}_r$ as well. To get a more detailed summary of our simulation we also estimate the standard deviation (SD) with

$$\widehat{\mathrm{SD}}\left(\hat{v}_r\right) = \sqrt{\frac{1}{n}\sum_{i=1}^{n}\left(\hat{v}_{r,i} - \bar{v}_r\right)^2} \tag{2.62}$$

where $\bar{v}_r$ is the average estimated velocity, and estimate the bias with

$$\widehat{\text{Bias}}\left(\hat{v}_r\right) = \bar{v}_r - v_r \ . \tag{2.63}$$

We explore how the RMS$(\hat{v}_r)$, Bias$(\hat{v}_r)$, and SD$(\hat{v}_r)$ vary with S/N and v_r. Our simulation takes 5 equally spaced values of S/N $100, 150, ..., 300$ and 4 values of v_r equally spaced on a log scale from 0.01 to 100 m/s. For each pair of S/N and v_r values, we use the estimated template spectrum for 51 Pegasi to simulate 2000 independent spectra with the proper Doppler shift given by Equation (2.2). Each such simulation consists of using cubic splines to interpolate the shifted, oversampled, and high S/N template to the same wavelength solution as the observed 51 Pegasi spectrum from EXPRES on JD 2458639.958 (see Section 2.5 for more details) and including Poisson noise of the specified S/N.

To approximately account for the uncertainty of the estimated template in this simulation we use the results from Section 2.4.1. Figure 2.11 illustrates that the RMS (as defined in Equation (2.60)) for a given S/N does not change significantly when increasing the number of spectra beyond about 21. Therefore, we take the column of the left plot in Figure 2.11 pertaining to 21 spectra and the results shown in Figure 2.12 to map the S/N of observed spectra to an effective S/N of the estimated template spectrum. For each of the 2000 independent spectra in this simulation, and for each pair of S/N and v_r, we add noise to the true template with the appropriately mapped effective S/N to approximate the effect of using the estimated template.

The results for obtaining each $\hat{v}_r$ with the HGRV method are shown in Figure 2.13. The left panel of Figure 2.13 illustrates that the HGRV method is able to obtain a precision less than 0.3 m s^{-1} when the S/N is approximately 250 or higher, at least in the small RV regime. Additionally, the right panel of Figure 2.13 builds upon the model misspecification simulation done in Section 2.3.4 and informs us that combining many (non-Gaussian) absorption features in the HGRV method does not lead to an amplified systematic bias. We also find

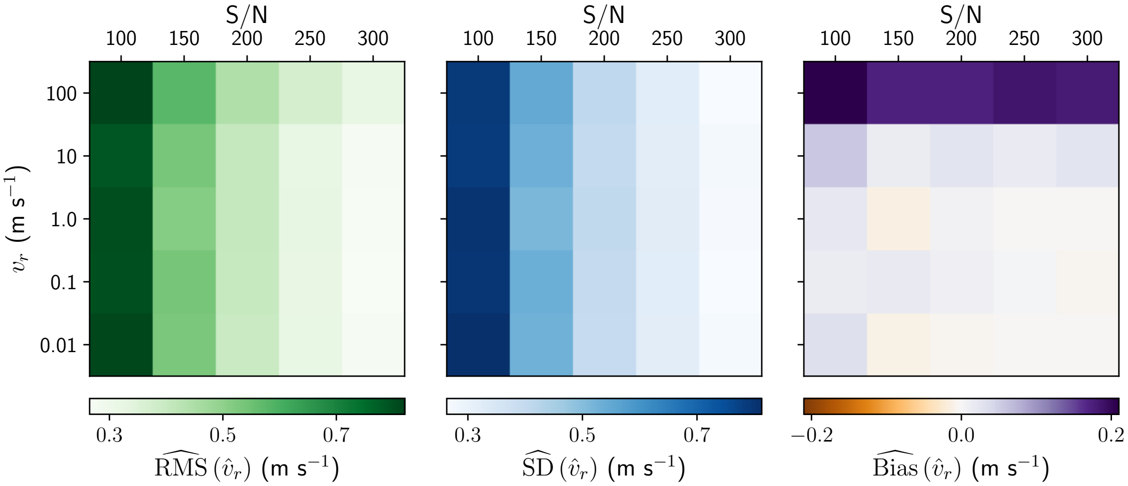

Figure 2.13: The results for applying the HGRV method to spectra simulated from the estimated 51 Pegasi template spectrum. The left, middle, and right panels show the estimated RMS, SD, and bias of the estimated RV respectively. All three panels share the same vertical axis that represents the true RV each spectrum was simulated with. The S/N of the simulated spectra are given by the horizontal axis on top of each panel. The color scale for each panel is represented by the colorbar below it. Each pair of S/N and v_r involved 2000 independent simulations to estimate the three quantities.

that the bias is somewhat proportional to the true RV. Furthermore, the SD contributes significantly more to the overall RMS than whatever bias may be present at the RV and S/N considered here.[7]

We also run the same simulation, estimating the RV with the CCF method as used in the EXPRES pipeline (Petersburg et al., 2020) with the commonly used HARPS G2 mask. Such a mask is a collection of wavelengths and weights (based on line depths) for many of the absorption features in a spectrum; the mask is designed to align with the absorption features of a star at rest (i.e., a star with zero RV.) Since the CCF method returns an absolute RV, rather than a relative RV, we first calculate the RV given for the estimated 51 Pegasi template with no noise (-33168.5399 m s^{-1}) and subtract this offset from all estimated RV's from the simulation. We then compare the estimated bias, SD, and RMS of the two

---

[7] We also performed the same simulation with a S/N of 1000 and a RV of 1 m s^{-1} (again using the estimated 51 Pegasi template spectrum and simulating 2000 independent spectra). This simulation gave an estimated RMS of 0.077 m s^{-1}, an estimated SD of 0.077 m s^{-1}, and an estimated bias of 2.5×10^{-3} m s^{-1}. This demonstrates that the HGRV method has the capability of obtaining a RV precision less than 0.1 m s^{-1}.

methods at each pair of S/N and v_r. Figure 2.14 shows the difference in RMS between the HGRV and CCF methods. Since every pair of S/N and v_r in Figure 2.14 shows a negative RMS difference, this suggests that the HGRV method has higher RV-precision than the CCF approach in this regime.

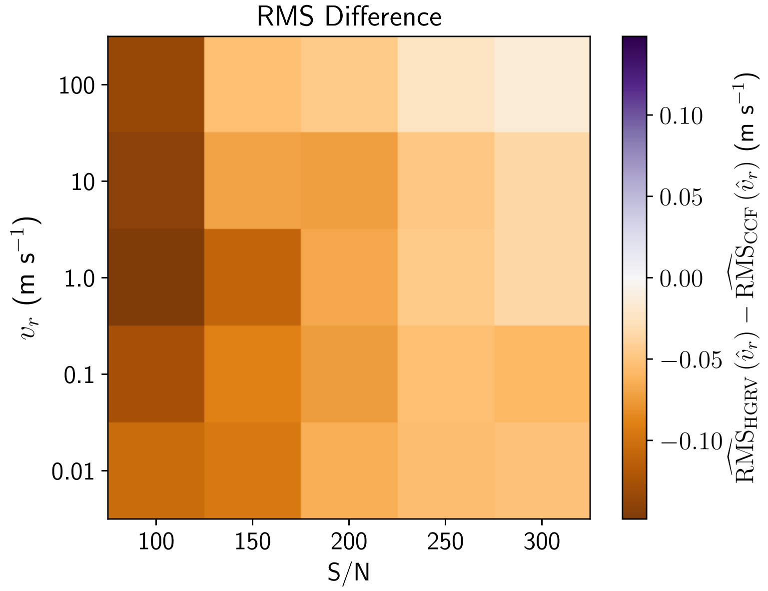

Figure 2.14: The difference between the HGRV and CCF RMS for each pair of S/N and true v_r. Each pair consisted of 2000 independent simulations for each method. The difference is indicated on the right by the color bar which is centered at 0.0 m s^{-1}, and demonstrates the higher RV-precision of the HGRV method.

As a more detailed summary of the RMS improvement of the HGRV as demonstrated by Figure 2.14, the difference in the estimated SD and absolute bias (the sum of squares of which equal the squared RMS) is shown in Figure 2.15.

Figures 2.14 and 2.15 inform us that the HGRV method is an example of the statistical phenomenon where a small increase in bias reduces the overall RMS. The greatest difference in RMS between the HGRV and CCF methods appears to be at low S/N.

We suspect that the HGRV method's reduced RMS may be connected to the pixel sampling of the wavelength. In this simulation we found that, when using the wavelength sampling of the NSO spectrum, the RMS between the CCF and HGRV methods was nearly the

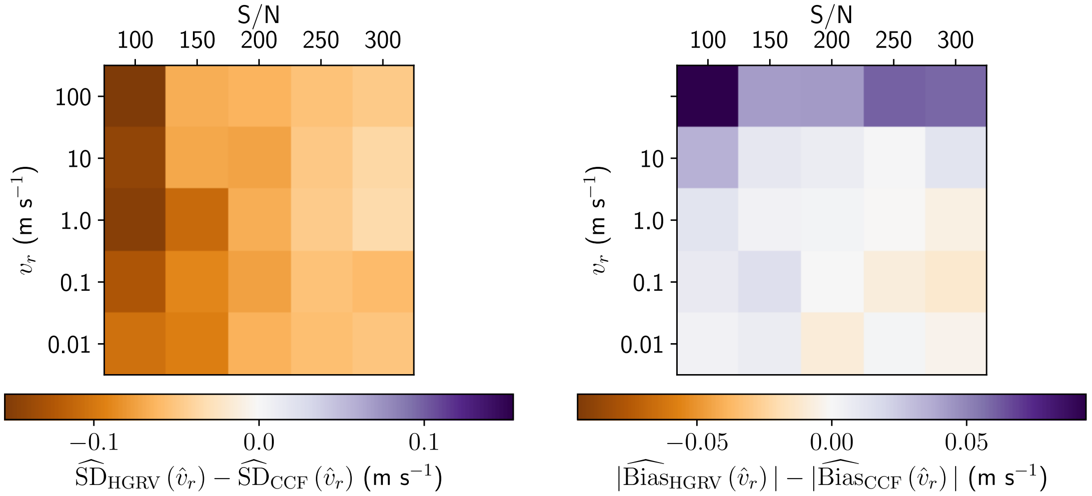

Figure 2.15: The difference between the HGRV and CCF standard deviation and absolute bias for each pair of S/N and true v_r. Each pair consisted of 2000 independent simulations for each method. The differences are indicated below each panel by the color bars which are centered at 0.0 m s^{-1}.

same at most pairs of S/N and v_r. However, when we instead interpolated to the wavelength solution of a 51 Pegasi spectrum observed by EXPRES, the obvious difference in RMS as demonstrated in this simulation study emerged. This suggests that the HGRV method may be more robust against the pixel sampling that differs across spectrographs.

To check the stability of this simulation, we used the wavelength solution for the 51 Pegasi spectrum from EXPRES observed on JD 2458804.588 instead of the wavelength solution from JD 2458639.958 used above. Running the HGRV and CCF approach each with 2000 independent simulations with $v_r = 1$ m s^{-1} and a S/N of 200 produced an RMS difference of -0.088 m s^{-1} (previously -0.067 m s^{-1}as shown in Figure 2.14). All estimated RVs from the CCF and HGRV methods for these simulations are provided in the repository $https://github.com/parkerholzer/hgrv\_method$.

2.5 Applications to 51 Pegasi data

51 Pegasi is the first main-sequence star similar to the Sun discovered to possess an exoplanet (Mayor and Queloz, 1995). The exoplanet has been found to have a RV semi-amplitude of 55.57 ± 2.22 m s^{-1}and orbital period of 4.2292 ± 0.0003 days (Mayor and Queloz, 1995; Marcy et al., 1997; Wang and Ford, 2011a; Bedell et al., 2019). To test the proposed HGRV method, we use data recently collected for 51 Pegasi by EXPRES (Jurgenson et al., 2016; Petersburg et al., 2020). The recent spectrograph of EXPRES corrects for many of the instrumental effects that prior observations of 51 Pegasi were unable to avoid, allowing for greater precision of derived RV. Our dataset consists of 56 observed spectra from JD 2458639 to 2458805 (June 5, 2019 to Nov. 18, 2019). The S/N of these spectra ranges from 89 to as high as 385, but most are close to 200 (see Table 2.1 in Section 2.5.3 for more details). These spectra have wavelength solutions that differ and do not consist of equally spaced pixels.

2.5.1 Data Corrections

The raw data collected by the spectrograph do not have a flat continuum. This is in part due to the star's temperature causing more photons to be emitted at certain wavelengths than others. It is also due to instrumental effects such as the theoretical blaze function (Barker, 1984; Xu et al., 2019). To correct for these effects, we adopt the normalization from the EXPRES pipeline provided with each spectrum (Petersburg et al., 2020).

We also correct for the effects of the Earth's motion around the Sun by adopting the barycentric corrected wavelength solution provided with each observed spectrum by the EXPRES pipeline (Blackman et al., 2017, 2020; Petersburg et al., 2020). Without the barycentric wavelengths provided by the EXPRES team, our derivation of RV would incur errors at the level of tens of cm s^{-1}.

Finally, we correct for absorption features due to the Earth's atmosphere, often referred to as tellurics. Since the spectrograph is ground-based, the light from the star passes through the Earth's atmosphere, causing the presence of additional absorption features in the spectrum that are not representative of the target star. To correct for these tellurics, we use the model provided by the EXPRES team with each spectrum that was created using the approach of Leet et al. (2019). Although one could potentially divide out shallow tellurics to approximately correct for them with such a model, we take a more conservative approach and mask out all pixels with a telluric model normalized flux less than 1.0.

While this telluric correction approach may not remove all tellurics, the HGRV method has two advantages that minimize the effect tellurics have on the estimated RV. First, because the tellurics occur at the same wavelength over time in the raw spectra, and therefore occur at different wavelengths in the barycentric corrected spectra, the nonparametric smoothing used to estimate the template averages out any tellurics missed by the telluric model. Second, any tellurics that persist after the smoothing in the estimated template and are detected by the AFF algorithm will have a very small depth. Therefore, they will have a relatively low leverage in the HGRV regression, minimally affecting the estimated coefficient.

Because a spectrum covers over 3000 Å of wavelength, the spectrograph collects the data in (partially overlapping) wavelength orders stacked onto the rectangular detector. Therefore, we begin by stitching all orders of a given epoch together to create a single array of wavelength and normalized flux. To stitch two neighboring orders together in their overlapping region, we use cubic-spline interpolation to give the same wavelength solution to both orders in the overlap region (Mészáros and Prieto, 2013). We then take the (point-wise) weighted average of the normalized flux in the overlap region of the two orders. Since the signal decreases at the edge of each order due to the instrumental blaze function, we set the weights for this averaging to decrease linearly for a given order as we get closer to the edge of the order. After applying this stitching to all neighboring orders we have a full observed spectrum for each epoch.

We then proceed to estimate the template spectrum by way of local quadratic regression as described in Section 2.3.5. A small wavelength window of the estimated template spectrum that is calculated from the 51 Pegasi data is shown in Figure 2.16.

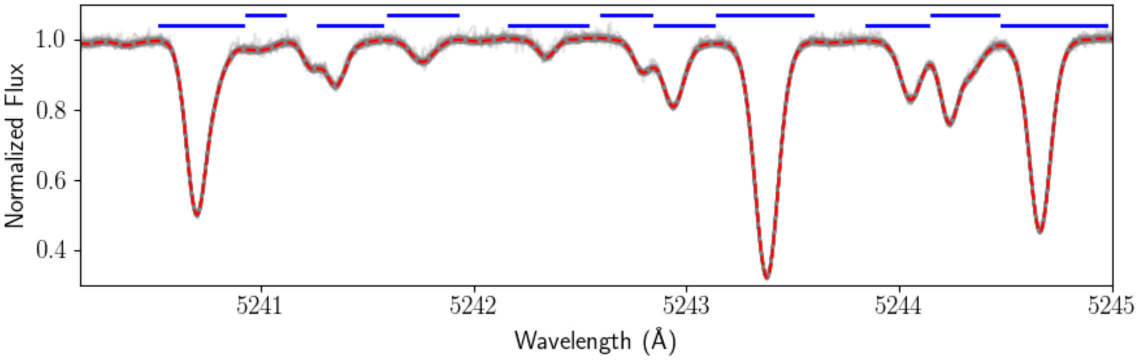

Figure 2.16: A subset of the estimated template spectrum calculated from 51 Pegasi data is shown in the red dashed line on top of all observed spectra used in the calculation (shown in gray). The feature bounds that result from running the AFF algorithm on the estimated template spectrum are also shown in blue horizontal lines. The full spectrum goes from $4470 - 6800$ Å, but for visualization only $5240 - 5245$ Å are displayed. The error bars of the estimated template between 4850 and 6800 Å (i.e., the wavelengths used in the analysis) have a median of 5.2×10^{-4} and a 99th percentile of 1.1×10^{-3}.

Once we have the high S/N estimated template spectrum we can use it in the AFF algorithm to find absorption feature wavelength bounds. The tuning parameters of the algorithm that were found through the optimization process described in Section 2.2 were $m = 7$, $\alpha = 0.05$, and $\eta = 0.07$ while eliminating any features with a line depth less than 0.015. The algorithm finds a total of 4190 features between wavelengths 4470 Å and 6800 Å. The results of this are also indicated in Figure 2.16 for the section of the spectrum displayed. Note that when neighboring features are strongly blended together, the AFF algorithm may either count both as a single feature or only pick out one of the two.

2.5.2 Absorption Feature Parameters

In order to use Equation (2.59) and estimate the RV, we need to get estimates of the Gaussian parameters d_i, μ_i, and σ_i for each absorption feature i using the high S/N estimated template spectrum. To do so we use the Trust Region Reflective algorithm (Branch et al., 1999), which allows for initialization and bounds for each parameter to be fitted in non-linear least-squares. For absorption feature i we initialize the Gaussian amplitude d_i at one minus the minimum flux attained by the estimated template spectrum within the wavelength bounds of feature i, the Gaussian center μ_i is initialized at the wavelength for which this minimum flux is attained, and the Gaussian spread σ_i is initialized at one-fifth the width of the wavelength window for feature i. The bounds on the Gaussian amplitude are set to be $[0, 1]$, the Gaussian center is restricted to be within the wavelength bounds for feature i, and the Gaussian spread is lower-bounded by 0 and upper-bounded by the width of the wavelength window for feature i.

For computational purposes, we do not optimize the Gaussian parameters for all absorption features simultaneously. Instead, we estimate the parameters of one absorption feature by simultaneously optimizing that feature with its two neighboring features. If the resulting fit has a MSE within the wavelength bounds of the feature that is high[8], which particularly happens when two strongly blended spectral lines are counted as one absorption feature, we try fitting a sum of two Gaussians to it. If this still does not give a good fit, we eliminate the respective feature so as to minimize the effects of model misspecification analyzed in Section 2.3.4. Out of the 4174 absorption features detected by the AFF algorithm, 3868 were well-fitted with one or two Gaussians. An example of the fit model spectrum is shown in Figure 2.17. Most of the features that were eliminated at this stage were strongly blended with one or more neighboring features.

---

[8] We consider a MSE to be high if it is greater than four multiples of the median MSE.

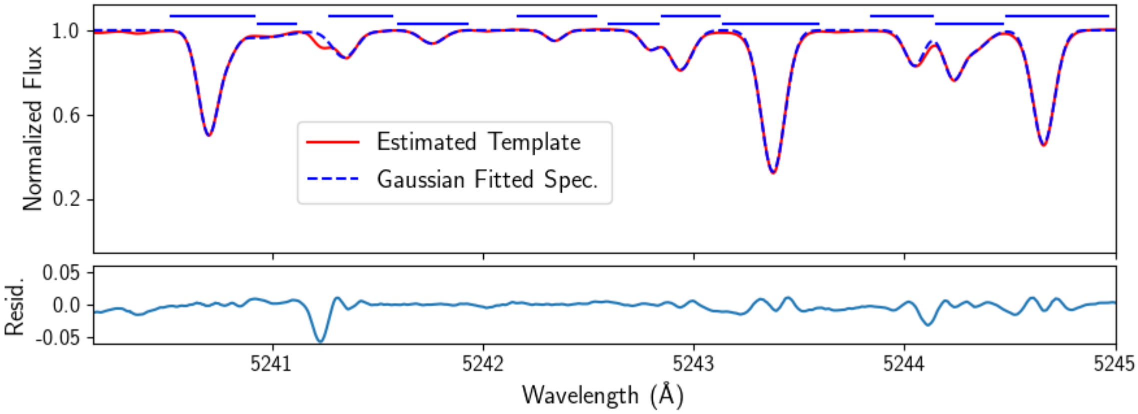

Figure 2.17: The estimated template spectrum for 51 Pegasi is shown in solid red with the spectrum that approximates it as a sum of Gaussians shown in dashed blue. The full spectra go from $4470 - 6800$ Å, but for visualization only $5240 - 5245$ Å are displayed. All absorption features in this wavelength range were well-fitted with Gaussians within the feature wavelength bounds. Portions of the spectrum that are poorly fitted with the sum of Gaussians are not contained within wavelength bounds of detected features, indicated with horizontal blue solid lines. The residual difference is shown below the main plot with the same Wavelength axis and a magnified vertical axis.

2.5.3 Results

To derive the RV for each epoch, we first limit the spectrum to the wavelength region $4850 - 6800$ Å. While the wavelength solution is excellent from 5000 to 7000 Å due to the laser frequency comb of EXPRES spanning that region (Blackman et al., 2020; Petersburg et al., 2020), and increasingly poor outside that window, we find that the spectra are acceptable for our purposes down to about 4850 Å.[9] Below 4850 Å the noise of the spectra increases and wavelengths above 6800 Å have too many strong telluric features. Limiting to this wavelength region reduces the number of absorption features from 3868 to 2796. We furthermore eliminate any pixels in the spectrum that are not contained in the wavelength windows of these 2796 features.

---

[9] The RV estimation error for the CCF and FM approaches increases when extending to wavelengths below 5000 Å. The HGRV approach does not appear to be negatively impacted when using wavelengths down to 4850 Å; the reason for this is not yet fully understood.

After using cubic-splines to interpolate the high S/N, oversampled, estimated template spectrum to the wavelength solution of the observed spectrum for a given epoch[10] (Mészáros and Prieto, 2013), we calculate the difference spectrum between the two. We then compute a new variable, which can be thought of as a transformation of the wavelength, using the sum $\sum_{j=1}^{n} \frac{\sqrt{\sqrt{\pi}}d_j\mu_j}{c\sqrt{2\sigma_j}}\psi_1\left(x_i;\mu_j,\sigma_j\right)$ from Equation (2.59). This transformation uses all fitted Gaussian parameters, after which we model the difference flux across the full stitched spectrum as a function of this new variable using weighted least-squares regression without an intercept to get the single RV estimate, $\hat{v}_r$.[11] The standard error of $\hat{v}_r$ is also easily estimated by the usual least-squares approach. On average across the epochs, this standard error is approximately 0.52 m s^{-1}. An example of what the difference spectrum looks like in the interval $5242 - 5245$ Å, together with the fitted Hermite-Gaussian model, is shown in Figure 2.18.

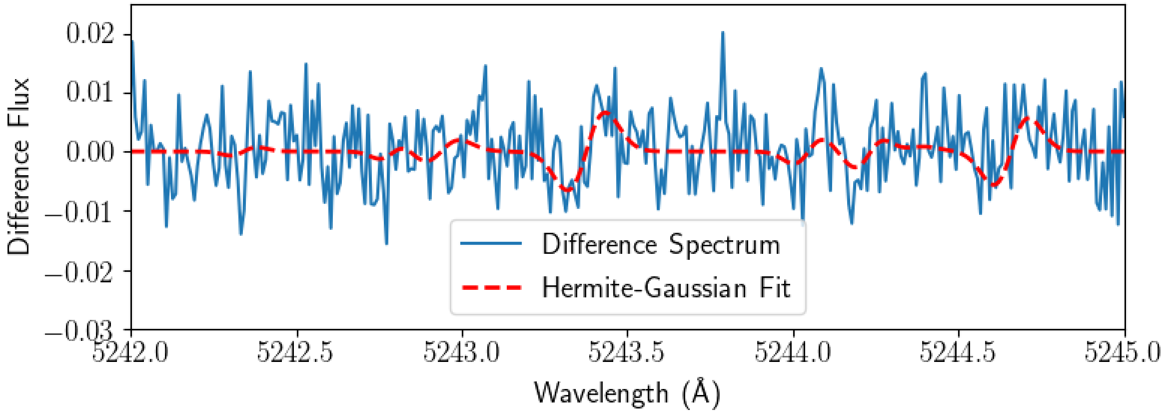

Figure 2.18: The difference spectrum between the estimated template and the spectrum observed on June 7, 2019 (JD 2458641.452) by EXPRES is shown in solid blue. The curve fitted according to Equation (2.59) is shown in dashed red. For visualization, only $5242 - 5245$ Å is shown.

For our analysis we used the same 47 observations that were analyzed by the EXPRES team in Petersburg et al. (2020) to estimate the orbital parameters. Several available obser-

---

[10] This is the only time in the proposed method that interpolation takes place.

[11] The usual regression diagnostics should be considered here (e.g., investigating extreme outliers or points with high leverage). No issues were found in this application to 51 Pegasi.

vations were excluded by the EXPRES team due to low S/N or failure of the laser frequency comb (see Petersburg et al. 2020 for details). The estimated RV's for all available 51 Pegasi EXPRES spectra using the proposed HGRV method are given in Table 2.1.

MJD (days)	**RV (m s^{-1})**	**S/N**
58639.458442	54.708 ± 0.404	385
58641.451749	−52.850 ± 0.516	179
58641.457773*	−53.662 ± 0.710	140
58643.462180	46.574 ± 0.521	225
58644.460959	33.536 ± 0.512	233
58646.455970	−43.411 ± 0.444	203
58646.461286	−42.241 ± 0.438	204
58648.456163	48.082 ± 0.505	244
58648.461529	48.711 ± 0.498	256
58650.450235	−53.092 ± 0.474	199
58650.455542	−53.741 ± 0.486	193
58651.443961*	14.317 ± 1.130	99
58651.452932	16.403 ± 0.431	284
58651.461117	16.515 ± 0.519	202
58652.456394	53.336 ± 0.653	172
58652.461797‡	52.696 ± 0.667	NA
58655.432426	−4.268 ± 0.459	220
58655.437704	−4.148 ± 0.453	222
58657.456051*	11.484 ± 0.706	142
58657.461248*	11.792 ± 0.623	157
58658.453711	−54.614 ± 0.361	230

Continued on next page

Table 2.1 – continued from previous page

MJD (days)	**RV (m s^{-1})**	**S/N**
58658.456675	-53.959 ± 0.343	247
58658.459600	-53.690 ± 0.341	243
58658.462634	-54.958 ± 0.330	257
58658.465250	-54.357 ± 0.350	236
58664.447934*	36.335 ± 1.171	94
58664.458268*	35.866 ± 1.270	89
58665.461782†	43.919 ± 0.538	214
58749.221866	47.001 ± 0.684	163
58749.227235‡	48.181 ± 0.688	NA
58763.233618	13.399 ± 0.466	230
58763.239194	12.112 ± 0.455	238
58764.311548	-53.651 ± 0.401	244
58764.318051	-53.765 ± 0.372	273
58772.315903	-36.680 ± 0.414	234
58772.321086	-37.061 ± 0.420	231
58780.114819	16.529 ± 0.464	237
58780.121270	15.728 ± 0.462	238
58787.198050	43.659 ± 0.557	194
58787.206110	44.981 ± 0.504	226
58796.099263	58.195 ± 0.546	235
58796.102083	57.456 ± 0.544	236
58796.104824	58.356 ± 0.546	235
58796.107532	57.717 ± 0.543	235

Continued on next page

Table 2.1 – continued from previous page

MJD (days)	RV (m s^{-1})	S/N
58798.128178	-52.396 ± 0.412	234
58798.129893	-55.148 ± 0.411	233
58798.131622	-53.502 ± 0.411	231
58798.133471	-51.899 ± 0.409	232
58803.110815	-34.492 ± 0.418	233
58803.114000	-33.286 ± 0.418	233
58803.116558	-34.086 ± 0.416	233
58803.118928	-32.252 ± 0.413	234
58804.076698	39.312 ± 0.503	239
58804.080907	40.058 ± 0.502	239
58804.084687	40.916 ± 0.504	240
58804.088298	41.212 ± 0.503	239

Table 2.1: Radial velocities derived from the HGRV method for 51 Pegasi. The first column gives the Modified Julian Day (MJD) which can be converted to JD by adding 2400000.5 days. The second column gives the estimated RV with its standard error, and the third column identifies the S/N. In the first column, $*$ indicates that it was not included in Petersburg et al. (2020) due to a S/N below 160. † indicates that it was not included because the laser-frequency comb of the EXPRES spectrograph failed. ‡ indicates it wasn't included due to a charge transfer inefficiency in the spectrograph detector. A machine-readable version of this table is available on the online repository for MainPaper.

Using the noted 47 EXPRES observations and the RV's estimated from the HGRV method, we compare the orbital parameters and the overall RV curve fit to those of the CCF method and the FM approach of Petersburg et al. (2020).

The exoplanet orbiting 51 Pegasi has been found to have an eccentricity that is nearly zero (Marcy et al., 1997; Wang and Ford, 2011a; Bedell et al., 2019; Petersburg et al., 2020) implying an orbit that is nearly circular. For a nearly circular planetary orbit, the host star's

RV will behave approximately as a sine curve over time. Therefore, we use the Levenberg-Marquardt optimization algorithm (Moré, 1978) to fit a sine curve to the derived RV using

$$v_r(t) = K \sin\left(\frac{2\pi}{P}t + \phi\right) + b\,. \tag{2.64}$$

The semi-amplitude (K) is initialized at 55.5 m s^{-1} and the period (P) at 4.23 days. The phase (ϕ), representing a horizontal shift of the sine curve, and the RV offset (b), giving the vertical shift, are both initialized at 0. To account for instrumental changes to EXPRES, b is allowed to be different before and after August, 2019. The optimization converges to the fit parameters given in Table 2.2[12], and the results of this fitting are shown in Figure 2.19. Therefore, the HGRV estimation method recovers the well-known parameters for 51 Pegasi. The only pair of parameters that had a significant correlation were the phase, $\hat{\phi}$, and the period, $\hat{P}$, with correlation -0.813. All other pairs had correlation magnitudes less than 0.25.

	HGRV	CCF	FM
$\hat{K}$	56.48 ± 0.16 m s^{-1}	56.20 ± 0.19 m s^{-1}	56.17 ± 0.18 m s^{-1}
$\hat{P}$	4.2308 ± 0.0001 days	4.2304 ± 0.0002 days	4.2306 ± 0.0002
$\hat{\phi}$	-1.333 ± 0.006	-1.326 ± 0.007	-1.331 ± 0.007
RMS	0.774 m s^{-1}	0.936 m s^{-1}	0.902 m s^{-1}

Table 2.2: Fit parameters of Equation (2.64) for 51 Pegasi.

Table 2.2 also gives the fit parameters from using the RV's estimated from the CCF and FM methods in Petersburg et al. (2020) for the 47 observations. Similar to the simulation study in Section 2.4.2, the reduced RMS demonstrates the ability of the HGRV method to outperform the traditional CCF approach.

---

[12] The fitted values of the two offsets are not given in Table 2.2 since they are expected to differ significantly between the three methods. The HGRV and FM methods give the RV relative to an estimated template, whereas the CCF method gives the RV relative to a pre-specified mask.

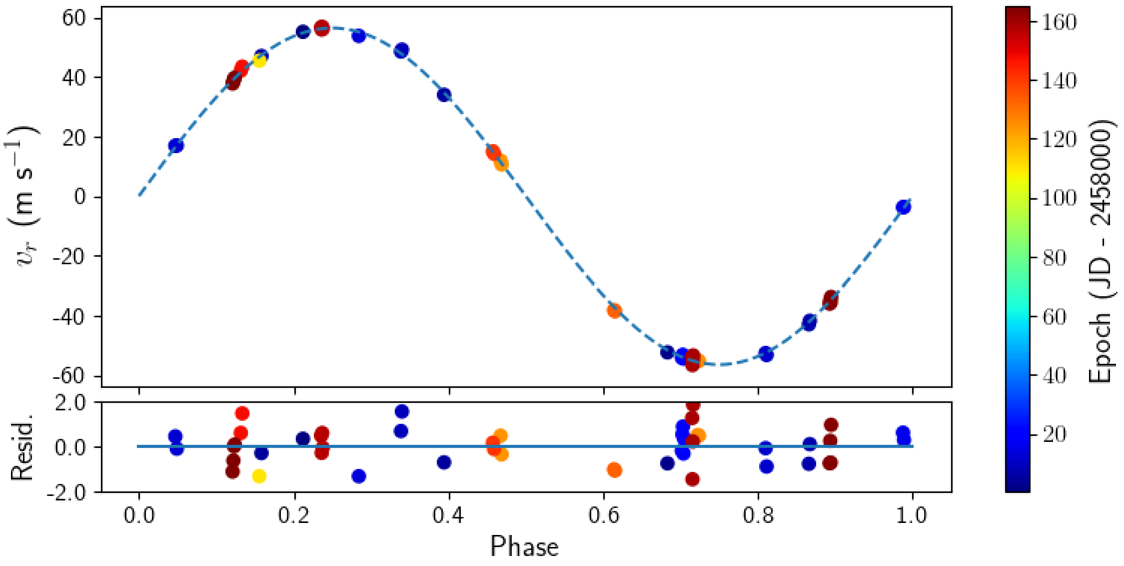

Figure 2.19: The RV's derived for 51 Pegasi by the HGRV method, plotted as a function of orbital phase with solid points whose color indicates the epoch according to the colorbar on the right. All error bars are smaller than the size of the points. The fitted sine curve from Equation (2.64) is also shown in a blue dashed curve using the HGRV values from Table 2.2. The residuals are shown in the magnified window at the bottom and have the same units (m s^{-1}) as the plotted RV's.

Including all 56 available spectra gives an estimated $\hat{K} = 56.38 \pm 0.16$ m s^{-1}, $\hat{P} = 4.2308 \pm 0.0001$ days, $\hat{\phi} = -1.327 \pm 0.005$, and an RMS$= 0.858$ m s^{-1}.

2.6 Discussion

In this paper we introduce a new approach to estimate the RV in stellar spectra for exoplanet detection that we call the HGRV method. This method works by modeling the differences between observed normalized spectra and an estimated template spectrum. Even though this difference spectrum visually appears to be nothing more than noise (e.g., see Figure 2.18), there is still an important Doppler signal present. By assuming that absorption features are approximately Gaussian and that $v_r < 500$ m s^{-1}, the HGRV method is able to identify this small signal. The application to 51 Pegasi using spectra from EXPRES provides an example of how the HGRV-estimated RV's produce a lower RMS in the overall Keplerian fit than the classical CCF approach. Furthermore, the simulation study of Section 2.4.2 demonstrates that at low RV, characteristic of Earth-like exoplanets orbiting Sun-like stars, the HGRV approach has higher RV-precision than the CCF.

Theorem 1 implies that the difference flux, imposed on a Gaussian absorption feature by a planetary Doppler shift, can almost entirely be explained as a constant multiple of ψ_1. This reduces RV estimation to linear regression with no intercept, where the estimated coefficient is the estimated RV. Therefore, the RV can be interpreted as a proportionality constant between the difference flux and an explanatory variable expressed as a linear combination of first-degree generalized Hermite-Gaussian functions (see Equation (2.59)).

One of the benefits of the HGRV method is the simplification to linear regression, allowing for straight-forward statistical inference on the estimated RV. Additionally, linear regression allows heteroskedasticity to be easily addressed with weighted least squares.

Interpolation is only used for stitching together the orders of each observed spectrum, and for getting the estimated template spectrum on the same wavelength solution as each observed spectrum. However, the interpolation for stitching orders can be fully avoided by taking each order out to the midpoint of the overlapping regions rather than using weighted averages. Alternatively, each order could be considered on its own as a way to fully avoid stitching orders. Furthermore, the template can be produced with the same wavelength solution as any observed spectrum by making these wavelengths the target in the local quadratic regression, therefore removing the need for later interpolation.

We also observed in the 51 Pegasi example that the HGRV method is relatively robust to inaccurate normalization. For example, the difference flux between the observation at JD 2458639.958 and the estimated template has a visually identifiable offset from zero, but including this observation's estimated RV in the orbital parameter estimation of Equation (2.64) slightly reduced the model's RMS. This robustness may be due to how, on the scale of individual absorption features, inaccurate normalization is approximately an even effect.

More work is needed, however, to confirm this general robustness.

An important feature of the HGRV method that also arises from its use of linear regression is its potential to be extended for disentangling Keplerian velocities due to exoplanets from atmospheric velocities due to the star itself. The convective motion and magnetic activity of stars lead to stellar activity in the form of starspots, granulation, faculae, etc. which add red noise to the spectra of stars that can hide a true Doppler-shift or temporarily mimic a RV (Saar and Donahue, 1997; Queloz et al., 2001; Desort et al., 2007; Meunier et al., 2010). Stellar activity can impose a false RV of approximate magnitude 1 m s^{-1} for quiet stars (Hatzes, 2002; Lagrange et al., 2010; Isaacson and Fischer, 2010) to hundreds of m s^{-1} for the most active (Saar and Donahue, 1997; Paulson et al., 2004). While efforts have been made to model this activity (e.g., Tuomi et al. 2013; Rajpaul et al. 2015; Delisle et al. 2018), as well as use alternative forms of the cross-correlation method to correct for activity (e.g., Queloz et al. 2001; Simola et al. 2019), these have had limited success in disentangling it from a true Doppler shift at RV's below 1 m s^{-1} (Dumusque et al., 2017).

One way the HGRV method could potentially be utilized for disentangling stellar activity from Keplerian Doppler shifts is by approximately orthogonalizing these two effects. The general idea behind this is to find a way by which stellar activity affects absorption features and a Doppler shift does not. Davis et al. (2017) uses principal components analysis to show that, at least according to simplified models of starspots and faculae on the Sun, the signals of stellar activity and a Doppler shift are distinguishable. Therefore, stellar activity would change a Gaussian absorption feature in a way that requires more Hermite-Gaussian terms than just ψ_1, whereas Theorem 1 states that (at least at low RV) a Doppler shift would not. One could then use observations from either the Sun (e.g., Dumusque et al. 2014) or a star with high stellar activity levels (e.g., Giguere et al. 2016) to model c_1 in Equation (2.8) as a function of the higher-degree coefficients, and remove the RV component that is due only to stellar activity. This is possible because the Hermite-Gaussian functions are orthogonal, and therefore as long as the blending between neighboring absorption features is small, a sum of higher-degree Hermite-Gaussian functions would be approximately orthogonal to the sum of first-degree Hermite-Gaussian functions. These ideas are the topic of future work.

The proposed method does have the limitation that at high values of RV, c_1 in Equation (2.8) is no longer the only coefficient that is significantly non-zero (see Figure 2.7), therefore, the HGRV method would not work well. Fortunately, a small fraction of detected exoplanets, none of which are Earth-like, exert such a large RV on their host star. But values of RV well above 500 m s^{-1} easily arise when considering binary star systems.

An improvement that could potentially be made to the proposed method is to relax the assumption of absorption features being Gaussian shaped. The advantage of using this assumption is that its derivative is a constant multiple of a basis function in the well known orthonormal Hermite-Gaussian basis. It is this orthogonality that potentially will allow us to identify signals that are unique to stellar activity and ultimately correct for it in the RV estimation. For M-dwarfs, however, where there is essentially no continuum and absorption features overlap significantly, this orthogonality may not be possible. Furthermore, this assumption allows us to quantify with Theorem 1 the approximation error of our model. In order to replace the Gaussian assumption with a more general shape and potentially still model out stellar activity, one may need to have the derivative of the new shape be a basis function in another orthonormal basis.

Data and Python3 code associated with this work can be found at
https://github.com/parkerholzer/hgrv_method. The HGRV method is also implemented in the open source R package *rvmethod*.

2.7 Conclusion

By using the mathematical property that Doppler-shifting a Gaussian is nearly the same as adding a first-degree Hermite-Gaussian function, we propose a new method for estimating a

Doppler shift in the spectrum of a star. Under the assumptions that the spectrum's absorption features can be well approximated by a sum of Gaussians and that the true RV is not too large in magnitude, the problem of estimating a RV in the spectrum can be simplified to weighted linear regression with no intercept. By testing this new method on recently collected, high-resolution spectra from EXPRES for the star 51 Pegasi we recover the well known orbital parameters with an overall RMS (0.774 m s^{-1}) below that of the traditional CCF method (0.936 m s^{-1}). This is only possible because the barycentric corrected wavelengths were provided by the EXPRES team. Furthermore, simulation studies demonstrate the ability of the HGRV method to outperform the CCF approach, giving an RV-prevision RMS that is up to approximately 15 cm s^{-1} lower than the CCF. This includes at the level of RV that is characteristic of Earth-like exoplanets orbiting Sun-like stars (i.e., 0.1 m s^{-1}). Unlike many other RV estimation algorithms, the HGRV method easily allows for statistical inference on the estimated RV, does not rely heavily on interpolation, takes account of the functional relationship in neighboring pixels, and has a natural extension that could potentially be used to model out the effects of stellar activity.

Chapter 3

A Stellar Activity F-statistic For Exoplanet Surveys (SAFE)

Parker H. Holzer, Jessi Cisewski-Kehe, Lily Zhao,

Eric B. Ford, Christian Gilbertson, Debra A. Fischer

Holzer et al. (2021b)

3.1 Introduction

In the exoplanet discovery community focused on extreme precision radial velocity (RV) measurements, better understanding the activity that takes place in the atmospheres of stars is an important goal (Fischer et al., 2016; Dumusque et al., 2017; Davis et al., 2017; Jones et al., 2017; Dumusque, 2018; Cretignier et al., 2020). One reason why this is the case is because stellar activity can produce RV's that mimic, or hide, the signal induced by an orbiting exoplanet (Saar and Donahue, 1997; Queloz et al., 2001; Desort et al., 2007; Meunier et al., 2010). This is one of the main hinderances to discovering more Earth-like exoplanets around Sun-like stars (Hatzes, 2002; Lagrange et al., 2010; Isaacson and Fischer, 2010). Therefore, to discover more planetary systems similar to the Earth-Sun system, we likely need a better way to detect the presence of, and ideally remove the effects of, stellar activity in stellar spectra.

Many statistics developed by astronomers aim to diagnose stellar activity, and are commonly referred to as "stellar activity indicators." Some of these are built from the cross-correlation function (CCF) commonly used to derive the RV of the star (e.g., Baranne et al. 1996; Pepe et al. 2002). Several stellar activity indicators, such as the Bisector Inverse Slope (BIS) (Queloz et al., 2001), the Bisector Slope (BiSlope) (Dall et al., 2006), Velocity span (V-span) (Boisse et al., 2011), and Bi-Gaussian (BiGauss) (Figueira et al., 2013), aim to detect a change in the asymmetry of the CCF, which would represent an asymmetric change in the shape of spectral absorption features on average. Others, such as the Full-Width Half-Maximum of the CCF (FWHM) (Queloz et al., 2001), instead aim to detect a symmetric change that results in the broadening or narrowing of the CCF. Other developed statistics, not calculated from the CCF, instead look for a change in specific absorption features that are physically known to be sensitive to the stellar magnetic field (e.g., Queloz et al. 2009; Pont et al. 2011), such as emission in the core of the Hα line (Giguere et al., 2016). More recent studies develop indicators that are primarily data-driven (Davis et al., 2017; Jones et al., 2017).

In this paper, we introduce a new stellar activity indicator developed by modeling the stellar spectrum with linear regression and calculating an F-statistic. This proposed statistic utilizes the idea in Chapter 3 that formulated the task of detecting an RV in the spectrum of a star as (weighted) simple linear regression (i.e., linear regression with a single explanatory variable). It accounts for different activity-induced shape changes in different absorption features, allows for straight-forward statistical inference, and is kept general so as to not assume a single predefined shape-change from stellar activity. We also allow this statistic to adapt to the spectral line depths across the spectrum that depend on the chemical abundance, effective temperature, and surface gravitational acceleration of the star observed.

We refer to this new stellar activity indicator as the Stellar Activity F-statistic for Exoplanet surveys (SAFE). It is an F-statistic used in a specially designed least-squares regression model. It is also designed to be robust to changes that are only due to orbiting exoplanets. Particularly, a small Doppler shift of the stellar spectrum would not affect the SAFE.

In Section 3.2 we introduce the general method of calculating the SAFE, beginning from the perspective of a single absorption feature and then extending to multiple features. The SAFE is then analyzed through simulations of stellar activity in Section 3.3. Additionally, the SAFE is applied to recently collected data from EXPRES (Jurgenson et al., 2016; Petersburg et al., 2020) in Section 3.4. Finally, a discussion of implications from the SAFE is provided in Section 3.5 and we conclude with Section 3.6.

3.2 Method

We begin by introducing the linear model used to calculate the SAFE statistic. By design, statistical inference is straight-forward with the SAFE, allowing accurate calculation of a p-value for testing the null hypothesis that there are no effects of stellar activity in the spectrum at the time of observation.

The general idea behind the SAFE is to detect any change over time in the shape of absorption features that is not simply due to a Doppler shift. Such a change is often shared across many absorption features in the spectrum. Examples of such changes would be a change in the asymmetry of the features, an altered line depth, or a broadening or narrowing of the features. Overall, the goal of the SAFE is to test the hypothesis that the only spectrum-wide change in absorption features is a Doppler shift. We note, however, that shape changes of absorption features can also be due to inaccurately correcting for instrumental effects such as the blaze function. Therefore, we assume throughout this paper that corrections for such effects have been done accurately and that the only remaining source of spectrum-wide shape changes is stellar activity.

An essential ingredient for the SAFE is a template spectrum that accurately represents a continuum normalized spectrum for the average state of the star. The need for such a template comes from how the SAFE at time t is calculated from the difference flux at time t, defined as

$$\mathrm{Diff}_t(x) = f_t(x) - \tau(x) \tag{3.1}$$

where x is the wavelength of stellar light, f_t is the observed normalized flux at time t, and τ is the template flux. If the effective temperature, surface gravitational acceleration, chemical abundances, and other stellar parameters are approximately known, one can use these to generate a synthetic spectrum as a template (Sneden et al., 2012). However, since these stellar parameters are rarely known to the precision that is likely required for the SAFE, we propose the combined non-parametric smoothing approach of Chapter 3. A second ingredient, which is primarily used in the template estimation, is an RV estimate for each observed spectrum. This estimate could come from the Hermite-Gaussian approach in Chapter 3, a CCF-based approach (Mayor and Queloz, 1995; Pepe et al., 2002; Petersburg et al., 2020), or any other method that estimates the RV well[1]. Finally, a third ingredient is a wavelength mask giving approximate wavelength intervals corresponding to absorption features. Since we do not make any assumptions about the shape of absorption features, a mask covering as many features as possible is preferred. We use the Absorption Feature Finder (AFF) algorithm described in Chapter 3 for this.

This method also requires one to pick a set of basis functions, each representing a particular shape change of absorption features in the spectrum. We propose the generalized

---

[1] We found through a simulation study that the SAFE statistic is robust to RV estimate errors within 5 m s^{-1} of the true velocity.

Hermite-Gaussian functions defined as

$$\psi_n(x;\mu,\sigma) = \frac{1}{\sqrt{\sigma 2^n n! \sqrt{\pi}}} H_n\left(\frac{x-\mu}{\sigma}\right) e^{-\frac{(x-\mu)^2}{2\sigma^2}}, \tag{3.2}$$

where μ is the location parameter, σ is the spread parameter, and H_n is the n'th degree (physicist's) Hermite polynomial which can be expressed as

$$H_n(z) = n! \sum_{m=0}^{\lfloor n/2 \rfloor} \frac{(-1)^m}{m!(n-2m)!}(2z)^{n-2m} \tag{3.3}$$

(Lanczos, 1938).

In Equation (3.3), $\lfloor a \rfloor$ represents the floor function that returns the largest integer less than or equal to the real number a. By a simple change of variables one can show that the set of generalized Hermite-Gaussian functions forms a complete orthonormal basis of the set of all square-integrable real-valued functions, $L^2(\mathbb{R})$ (Johnston, 2014). Therefore, for a general absorption feature, as long as the difference flux due to either a Doppler shift or stellar activity is such an $L^2(\mathbb{R})$ function, it can be decomposed into the generalized Hermite-Gaussian function basis. We do acknowledge, however, that there are many other choices that satisfy these properties. We prefer the Hermite-Gaussian basis because it is composed of differentiable functions that are either even or odd (with respect to μ) and are localized like spectral lines. Another motivation for this basis is that many absorption features are close to being Gaussian-shaped, and the Hermite-Gaussian basis contains both the Gaussian and its derivative.

3.2.1 A Single Absorption Feature

A large portion of the spectrum is used to calculate the SAFE; however, for simplicity we begin by considering the scenario of a single absorption feature indexed by i.

Chapter 3 show mathematically that if an absorption feature is Gaussian-shaped, the difference flux due to a Doppler shift can be well modeled by only using ψ_1. However, since absorption features are often strongly blended, and the wings of large features are more Lorenzian than Gaussian, we wish to relax the assumption of Gaussianity. To do so we instead assume that the difference flux can be written as a linear combination of all Hermite-Gaussian functions up to degree five[2]. This assumption helps to relax the assumption made in Chapter 3 that absorption features are Gaussian (i.e., that the difference flux can be written as a constant multiple of just ψ_1). Written in equation form, we model the difference flux due to a Doppler shift of absorption feature i, $\mathrm{Doppdiff}_i$, as

$$\mathrm{Doppdiff}_i(x) = \sum_{d=0}^{5} \alpha_{i,d} \psi_d \left(x; \hat{\mu}_i, \hat{\sigma}_i\right) \tag{3.4}$$

where $\hat{\mu}_i$ and $\hat{\sigma}_i$ are the location and spread estimated from fitting a Gaussian to feature i.

In practice, to get estimates $\hat{\mu}_i$ and $\hat{\sigma}_i$, we follow the approach in Chapter 3 with a template spectrum for the star. The AFF algorithm is used to identify wavelength windows corresponding to absorption features in the template. Using nonlinear optimization, a sum of three Gaussian density functions are used to fit each absorption feature and its neighboring features. As a further step to correct for inaccurate continuum normalization, the continuum value from which the fitted Gaussian is subtracted, cont_i, is also a free parameter (within the bounds of 0.9 and 1.1). Features where the optimization does not converge are eliminated. Occasionally, the optimization converges to a poor fit. Therefore, any feature is eliminated if $\hat{\sigma}_i$ is more than 1.5 multiples of the interquartile range above the 75'th percentile of all the fitted $\hat{\sigma}_i$, $\hat{\sigma}_i$ is less than 0.001 Å, $\hat{\sigma}_i$ is greater than one sixth of the feature wavelength window width, or the amplitude of the fitted Gaussian is positive. Finally, any feature where $\widehat{\mathrm{cont}}_i < 0.98$ or $\widehat{\mathrm{cont}}_i > 1.02$ is also eliminated. On average, we find that approximately 45

---

[2] The degree 5 limit was selected to make the SAFE flexible enough to detect a variety of possible shape changes of absorption features, but not so flexible that it affects the statistical power of the test due to too many additional variables in the model. We found that up to degree 5 provides a good balance of these motivations.

percent of the features identified by the AFF algorithm remain after these cuts.

If we knew how to write $\mathrm{Doppdiff}(x)$ in closed form, we could solve for the coefficients $\alpha_{i,d}$ exactly. However, since this is not the case, we use least-squares to project the discretized realization of $\mathrm{Doppdiff}_i(x)$ onto the space spanned by $\{\psi_d\left(x;\hat{\mu}_i,\hat{\sigma}_i\right)\}_{d=0}^{5}$. This gives $\hat{\alpha}_{i,0}$, $\hat{\alpha}_{i,1}$, $\hat{\alpha}_{i,2}$, ..., $\hat{\alpha}_{i,5}$ as estimates of the projection coefficients, and $\widehat{\mathrm{Doppdiff}}_i$ as the projected difference flux due to a Doppler shift.

In practice, we train $\widehat{\mathrm{Doppdiff}}_i$ by taking the template spectrum for absorption feature i, simulate a 10 m s^{-1} Doppler shift, interpolate back to the original wavelengths, and use least-squares to project the resulting difference flux onto the generalized Hermite-Gaussian functions of degree 5 or lower. $\widehat{\mathrm{Doppdiff}}_i(x)$ is similar to an estimate of the i'th absorption feature's derivative. Therefore, for any small RV the difference flux due to a Doppler shift is approximately a constant multiple of $\widehat{\mathrm{Doppdiff}}_i(x)$.

If stellar activity is present, then a Doppler shift is not the only source of the difference flux. Therefore, we would expect to have signal remaining in the residual difference spectrum, the difference flux remaining after removing a constant multiple of $\widehat{\mathrm{Doppdiff}}_i$. To test for this we model Diff_t defined in Equation (3.1) as

$$\mathrm{Diff}_t(x) = \beta_{1,i,t}\widehat{\mathrm{Doppdiff}}_i(x) \; + \sum_{\substack{d=0\\ d\neq 1}}^{5} \beta_{d,i,t}\psi_d\left(x;\hat{\mu}_i,\hat{\sigma}_i\right) \; + \; \varepsilon_t \tag{3.5}$$

where the random error ε_t has mean 0. This reduces the problem to a linear model of the difference flux as a linear combination of a small Doppler shift and the Hermite-Gaussian functions. One may notice that $\psi_1\left(x;\hat{\mu}_i,\hat{\sigma}_i\right)$ is not included in the model of Equation (3.5). Were $\psi_1\left(x;\hat{\mu}_i,\hat{\sigma}_i\right)$ to be included, the coefficients would be unidentifiable as $\widehat{\mathrm{Doppdiff}}_i(x)$ could then be written as a linear combination of the other terms. Furthermore, since most absorption features are approximately Gaussian and therefore $\widehat{\mathrm{Doppdiff}}_i(x)$ is almost the same as a first-degree Hermite-Gaussian function, including $\psi_1\left(x;\hat{\mu}_i,\hat{\sigma}_i\right)$ would potentially lead to collinearity issues.

We furthermore assume that ε_t is multivariate normal with a diagonal covariance matrix whose entries are well approximated by the squared uncertainties of the normalized flux. If these uncertainties are not provided we use the normalized template flux divided by the continuum used for normalization as the diagonal entries. This assumes that the raw flux, $F_{i,t}$, follows a Poisson$(\lambda_{i,t})$ distribution. Under this assumption, for large values of $\lambda_{i,t}$, $F_{i,t}$ approximately follows the Normal$(\lambda_{i,t}, \lambda_{i,t})$ distribution. Therefore, the normalized flux $F_{i,t}/c_{i,t}$ approximately follows the Normal$(\lambda_{i,t}/c_{i,t}, \lambda_{i,t}/c_{i,t}^2)$ distribution. Since $\lambda_{i,t}/c_{i,t}$ is well-approximated by the template flux τ_i at each time t, the difference flux at pixel i approximately follows the Normal$(0, \tau_i/c_{i,t})$ distribution. We acknowledge that a diagonal covariance matrix does not account for correlations due to the point spread function of the instrument, a potential improvement to be made in future work.

Now that we have the linear model in Equation (3.5), we can use it to perform statistical inference about the null hypothesis that no stellar variability effects are present at time t. Testing for the absence of stellar variability reduces to testing whether $\beta_{0,i,t} = \beta_{2,i,t} = \beta_{3,i,t} = \beta_{4,i,t} = \beta_{5,i,t} = 0$ in Equation (3.5). This can be done at each time t by comparing the residual sum of squares (RSS) when all five of these coefficients are used in the fit to the RSS when they are set to 0. These two quantities can be combined together to give an F-statistic that we can use to perform an F-test of the hypothesis that the only nonzero coefficient is $\beta_{1,i,t}$.

3.2.2 Multiple Absorption Features

Since the signals of stellar activity and low-mass exoplanets are so small, we need to extend the model to include nearly all absorption features in the spectrum. Using $\mathrm{Doppdiff}(x)$, the difference flux due to a Doppler shift for multiple absorption features in the spectrum, our

Doppler model from Equation (3.4) becomes

$$\text{Doppdiff}(x) = \sum_{i=1}^{m} \sum_{d=0}^{5} \alpha_{i,d} \psi_d \left(x; \hat{\mu}_i, \hat{\sigma}_i\right) \mathbb{1}\{\hat{l}_i \leq x \leq \hat{u}_i\} \tag{3.6}$$

where $\hat{l}_i$ and $\hat{u}_i$ are the wavelength bounds for feature i (with no overlap between features), and $\mathbb{1}\{A\}$ represents the indicator function that takes the value 1 if the statement A is true and 0 otherwise. In Equation (3.6), the outer sum is over all m absorption features and the inner sum is over the Hermite-Gaussian degrees up to 5. To simplify the process of estimating the values for each coefficient $\alpha_{i,d}$, the indicator function is included so that we can perform a least-squares fit on each absorption feature separately as described in Section 3.2.1. It also serves to exclude the continuum which has little relevant Doppler information. This, however, requires the assumption that the Doppler shift after applying the barycentric correction is not too large. Without an assumption of spectral line shapes, we are unable to mathematically quantify how small of a RV is small enough, but simulation suggests that less than 100 m s^{-1} is acceptable.

Once we obtain $\hat{\alpha}_{i,d}$ as least-squares estimates of the coefficients in Equation (3.6), we obtain $\widehat{\text{Doppdiff}}(x)$. Since this is trained using a Doppler shift that is small (10 m s^{-1}), $\widehat{\text{Doppdiff}}(x)$ is again an approximation of the template spectrum's derivative. So to expand our model to include all absorption features we simply need to use this term and sum over absorption features for the Hermite-Gaussian terms:

$$\text{Diff}_t(x) = \beta_{1,t} \widehat{\text{Doppdiff}}(x) \ + \sum_{i=1}^{m} \sum_{\substack{d=0 \\ d\neq 1}}^{5} \beta_{d,i,t} \psi_d \left(x; \hat{\mu}_i, \hat{\sigma}_i\right) \mathbb{1}\{\hat{l}_i \leq x_t \leq \hat{u}_i\} \ + \ \varepsilon_t. \tag{3.7}$$

Once again, this is a linear model and we can test whether $\forall_{d\leq 5,\ d\neq 1} \forall_{i\leq m} \beta_{d,i,t} = 0$. However, this is a very high-dimensional test. Since this is likely to cause the power of the test to be too small, we wish to revise the model in Equation (3.7) so that the dimension of the test is reduced.

We reduce the dimension by noting that the amplitude of the difference flux will differ across absorption features, but that the relative amplitudes are in many cases consistent. For example, Chapter 3 show that when the difference flux is caused by a small Doppler shift, the relative amplitudes of $\psi_1(x; \mu, \sigma)$ for Gaussian absorption features are given by an expression involving the line depth and width parameters, both of which can be estimated from the template. Here, we wish to fine-tune the Hermite-Gaussian terms in Equation (3.7) to effects of stellar activity rather than a Doppler shift. Since we do not assume absorption features are Gaussian, and because there is no existing parametric model for the difference flux from stellar activity, we need to estimate the relative amplitudes statistically rather than mathematically.

For this we use a set of 25 Spot Oscillation and Planet 2.0 (SOAP) spectra (Dumusque et al., 2014), designed to approximately represent the stellar activity effects of an active region rotating around the Sun. These SOAP spectra are set to have a 1% equatorial active region that starts from the back of the star and rotates around exactly once. They cover the wavelength range from 4470 to 6662 Å and have the full resolution of the National Solar Observatory (NSO) spectrum (Rimmele and Radick, 1998). Using the first of these spectra as the template, which has no activity effects present since the active region is on the back of the star, we use the AFF algorithm in Chapter 3 to identify wavelength bounds of absorption features. We then estimate the Gaussian fit parameters for each feature and project the difference flux due to a 10 m s^{-1} Doppler shift onto the space spanned by $\psi_0, \psi_1, ..., \psi_5$ according to Equation (3.6) to get the estimated $\widehat{\text{Doppdiff}}(x)$ for the represented star. For each of the 25 SOAP spectra we then subtract out the multiple of $\widehat{\text{Doppdiff}}(x)$ that minimizes the sum of squared residuals. The residual difference flux of a given feature is then projected onto the space spanned by $\psi_0, \psi_2, ..., \psi_5$ as in Equation (3.7) and the fitted coefficients for each of the m absorption features and each of the 25 SOAP epochs are stored.

This in turn gives 5 different $25 \times m$ arrays of SOAP coefficients, each corresponding to a particular Hermite-Gaussian degree. For each of these 5 arrays, the corresponding $25 \times m$

array can be viewed as 25 points in m dimensional space. We then use robust principal components analysis (rPCA) (Candès et al., 2011) which decomposes each $25 \times m$ matrix into a sum of a low-rank matrix, L, and a sparse matrix, S, allowing us to avoid being influenced by strong outliers.[3] Taking the singular-value decomposition of L gives us the first principal vector, the loadings $\hat{\gamma}_{d,i}$ of which estimate the relative amplitudes due to an active region.

Our approach towards obtaining these relative amplitude estimates is similar to the methods of Davis et al. (2017). However, instead of applying principal components analysis to the pixels, our approach applies it to the fitted Hermite-Gaussian coefficients. This allows us to account for the smooth functional relationship of neighboring pixels that belong to the same absorption feature. Furthermore, we only use the first principal vector for each Hermite-Gaussian degree. The set of relative amplitudes for each absorption feature from our approach is similar to the weighted mask used in the CCF method. However, there is more than just a single mask produced in our approach, each is obtained from dimensional reduction of SOAP simulations, and weights are replaced with relative amplitudes. Figure 3.1 gives a visualization of the relative amplitudes versus line depth.

Figure 3.1 illustrates that the shape change due to stellar activity is related to the depth of the absorption line (Cretignier et al., 2020). For degrees 0 and 2 the amplitude of the shape change appears to be roughly proportional with line depth, until reaching a depth of about 0.6. At this point the amplitude begins to decrease. Higher degrees also seem to show a relationship with depth, though not as clearly.

Using the estimates of these amplitudes, $\hat{\gamma}_{d,i}$, together with $\hat{\mu}_i$ and $\hat{\sigma}_i$ that are estimated through preprocessing, we define

$$\hat{\Psi}_d(x) := \sum_{i=0}^{m} \hat{\gamma}_{d,i} \psi_d\left(x; \hat{\mu}_i, \hat{\sigma}_i\right) \mathbb{1}\{\hat{l}_i \leq x \leq \hat{u}_i\} \; . \tag{3.8}$$

---

[3] If no strong outliers are present, this gives essentially the same results as the classical principal components analysis.

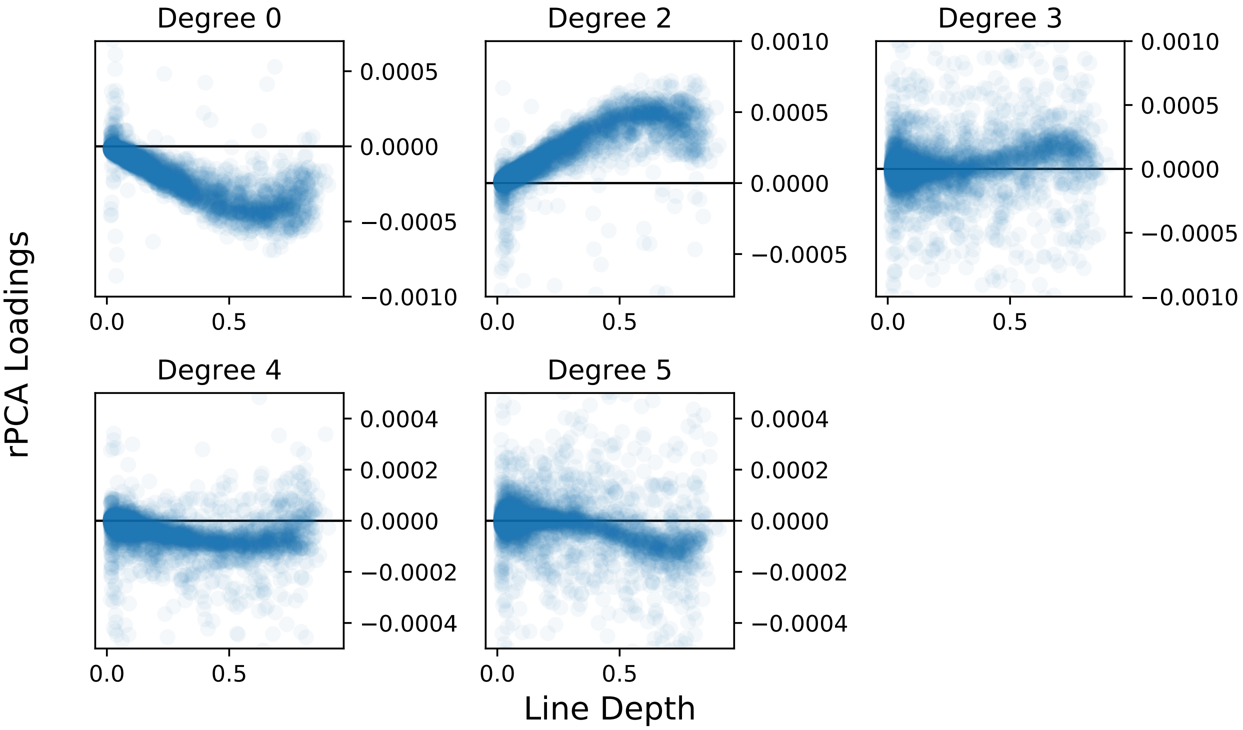

Figure 3.1: The relative amplitudes of absorption features for each Hermite-Gaussian degree. The amplitudes were obtained by applying rPCA to the Hermite-Gaussian coefficients fitted to the difference flux of SOAP spectra with a 1% equatorial active region. Each panel represents a different Hermite-Gaussian degree. The value of the relative amplitudes are given on the right of each panel, with the horizontal axis representing the line depth of the absorption feature with respect to the normalized flux 1.0.

Our final dimensionally-reduced model then becomes

$$\mathrm{Diff}_t(x) = \beta_{1,t}\widehat{\mathrm{Doppdiff}}(x) \; + \sum_{\substack{d=0\\ d\neq 1}}^{5} \beta_{d,t}\hat{\Psi}_d(x) + \; \varepsilon. \tag{3.9}$$

which is again a linear model. To account for the heteroskedasticity of the noise, we use weighted least-squares with the weights set to be the reciprocal of the squared uncertainty in normalized flux, or (if this uncertainty is not provided) the normalization continuum divided by the template flux.

Equation (3.9) is again a linear model that can be used for statistical inference about whether or not the difference flux at time t is (at least partially) due to stellar variability. The general idea behind the test statistic built for this purpose is to consider two different models: one where only the first term of Equation (3.9), $\widehat{\mathrm{Doppdiff}}$, is included in the model and a second where all the terms are included. If no stellar variability is present at time t, then the RSS of the first of these two models will not be significantly greater than the RSS of the second. Specifically, we define our test statistic as

$$\mathrm{SAFE_t} := \frac{\mathrm{RSS}_{\mathrm{dopp},t} - \mathrm{RSS}_{\mathrm{full},t}}{\mathrm{RSS}_{\mathrm{full},t}} \frac{n-6}{5} \tag{3.10}$$

where $\mathrm{RSS}_{\mathrm{dopp}}$ is the residual sum of squares when using only $\widehat{\mathrm{Doppdiff}}(x)$ in the regression, $\mathrm{RSS}_{\mathrm{full}}$ is the residual sum of squares with all the terms in Equation (3.9), and n is the number of data points included in the regression.[4] Under the null hypothesis, SAFE_t would follow the F-distribution with $(5, n-6)$ degrees of freedom, which allows us to calculate a p-value.

3.2.3 Multiple Testing Correction

Since each star is observed multiple times, each of which gives a different value of the SAFE, we need to account for multiple testing when analyzing the p-values given.[5] For a star observed N different times, we use the Bonferroni correction (Bonferroni, 1936) to control the family-wise error rate. For a given significance level, α, this entails comparing all N p-values to α/N instead of α when deciding whether or not to reject the null hypothesis of no stellar activity being present. This correction ensures that the probability of falsely concluding the presence of statistically-significant stellar activity in any of the N

---

[4] Note that $\left(\mathrm{RSS}_{\mathrm{dopp},t} - \mathrm{RSS}_{\mathrm{full},t}\right)/5$ follows the $\chi^2(5)$ distribution and is independent of $\left(\mathrm{RSS}_{\mathrm{full},t}\right)/(n-6)$, which follows the $\chi^2(n-6)$ distribution. Therefore, $\mathrm{SAFE_t}$ is a ratio of independent chi-squared random variables. This, therefore, can be easily generalized for situations where the covariance matrix of ε in Equation (3.9) is not diagonal due to effects like the points spread function.

[5] Note that this is not the same as testing the single hypothesis that none of the spectra have stellar activity signals.

observations is less than α.

For clarification, we note that in this context the p-value is the probability, when no stellar activity is present in the star, of obtaining a spectrum from the target star that gives a larger value of the SAFE than what was actually observed. We also note that when the p-value is found to not be below α/N, we do not conclude that there is no stellar activity present. Instead, we simply conclude that, whatever stellar activity might be present, we do not have sufficient evidence to detect it.

3.3 Simulation Studies

To test the proposed method, we begin by using a set of spectra simulated from SOAP. Our simulated sample consists of a time-series of 25 observations of the solar spectrum. The sample includes a 1% equatorial active region that begins at the back of the star and, at each successive observation, rotates around the star by a fixed angle. For the first seven, and the last six, epochs the active region is behind the star and, therefore, the spectrum is the same as the quiet solar spectrum.

3.3.1 SAFE Null Distribution

Since we have full knowledge of when the active region is present or not in SOAP, we use this knowledge to check the null-distribution of SAFE and to estimate the power of the SAFE test[6]. To simulate data for a true null, we use one of the SOAP spectra where the active region is behind the star. We begin by creating 13000 simulations of adding independent Poisson noise to the spectrum that gives a Signal-to-Noise Ratio per pixel (SNR) of 150. We use the quiet solar spectrum from SOAP as a template and follow the procedure described in

---

[6] The null distribution of the SAFE is the probability distribution it follows when no stellar activity is present (i.e., the null hypothesis is indeed correct). Since the SAFE is an F-statistic, this null distribution is an F-distribution. The power is the probability of concluding that the SAFE is statistically significant when there is indeed stellar activity present.

Section 3.2. The AFF algorithm finds a total of $4,114$ absorption features that remain after filtering out those for which convergence of Gaussian fit parameters was not reached or the spread was outside a reasonable range. After estimating the $\mathrm{Doppdiff}$ variable according to Equation (3.6), we use the SOAP amplitudes obtained above through rPCA to define all other covariates of the model in Equation (3.9). The estimated Gaussian fit parameters are obtained through the process described near the beginning of Section 3.2.1, using the quiet SOAP spectrum as the template.

For each simulation we calculate SAFE and it's associated p-value with the proper F-distribution. Since each set of simulated spectra has different noise realizations, each will produce a different p-value. If the distribution of the SAFE under no stellar activity is indeed the F-distribution used to calculate each p-value, then the p-values will follow the Uniform$(0,1)$ distribution. The distribution of the p-values given by this simulation study is illustrated in the histogram of Figure 3.2. Since this distribution is approximately uniform, this supports the F$(5, n-6)$ as the null distribution of SAFE (i.e., the distribution that describes the behavior of the SAFE when white noise and a small Doppler shift are the only sources of variation in the spectrum). If the true distribution of the SAFE, under no stellar activity, had a fatter right tail or were shifted upwards more than the F$(5, n-6)$ distribution, the p-values in Figure 3.2 would be more concentrated close to 0.0 than 1.0. Similarly, if the right tail of the true null distribution decreased faster than the F$(5, n-6)$ tail, the p-values in Figure 3.2 would be more concentrated near 1.0.

To check if the SAFE still follows the theoretical F-distribution in the presence of a Doppler shift, we follow the same procedure with a time-dependent RV $v_t = 10\sin(2\pi t/25)$ for $t = 1, 2, ..., 25$, which simulates the effect of an exoplanet completing exactly one circular orbit around the Sun. In a separate analysis we use the 25 SOAP spectra that represent a 1% equatorial active region. For each of the 25 phases in both of these data sets, we run 5000 independent simulations of adding SNR 150 Poisson noise to the spectrum and calculate SAFE and its associated p-value. Figure 3.3 illustrates the distribution of p-values at

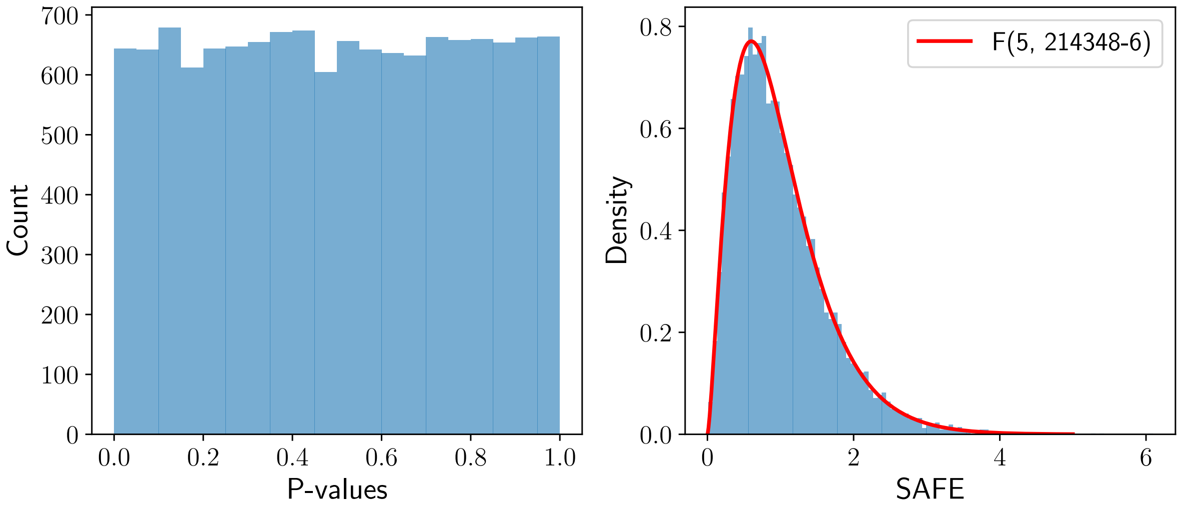

Figure 3.2: The left panel shows the distribution of p-values calculated with SAFE from 13000 independent simulations of a quiet SOAP spectrum with SNR 150. The right panel shows the distribution of the SAFE. Under the null hypothesis of no stellar activity, which is true here, the SAFE follows the $\mathrm{F}(5, n-6)$ indicated by the solid red curve and the calculated p-values should be $\mathrm{Uniform}(0,1)$, which is supported by the results.

each phase for both the true Doppler shift and the 1% equatorial active region.

For the simulated data that represents a true Doppler shift, the distribution of p-values should be approximately uniform at every time instance as the null hypothesis is true regardless of the RV. The top panel in Figure 3.3 illustrates that this is indeed true. The data representing the equatorial active region begins and ends with the null hypothesis being true as the active region is behind the star. But once the active region comes around the star the p-values should become more concentrated near zero. This scenario is also represented in Figure 3.3.

3.3.2 SAFE Power

We investigate the power of the SAFE test as a function of the active region's phase, and how it changes for different levels of noise. For each phase beginning when the active region comes around the star's edge to where it again goes behind, and for each SNR from 50 up to 200 in steps of 10, we add independent Poisson noise to the spectrum and calculate the

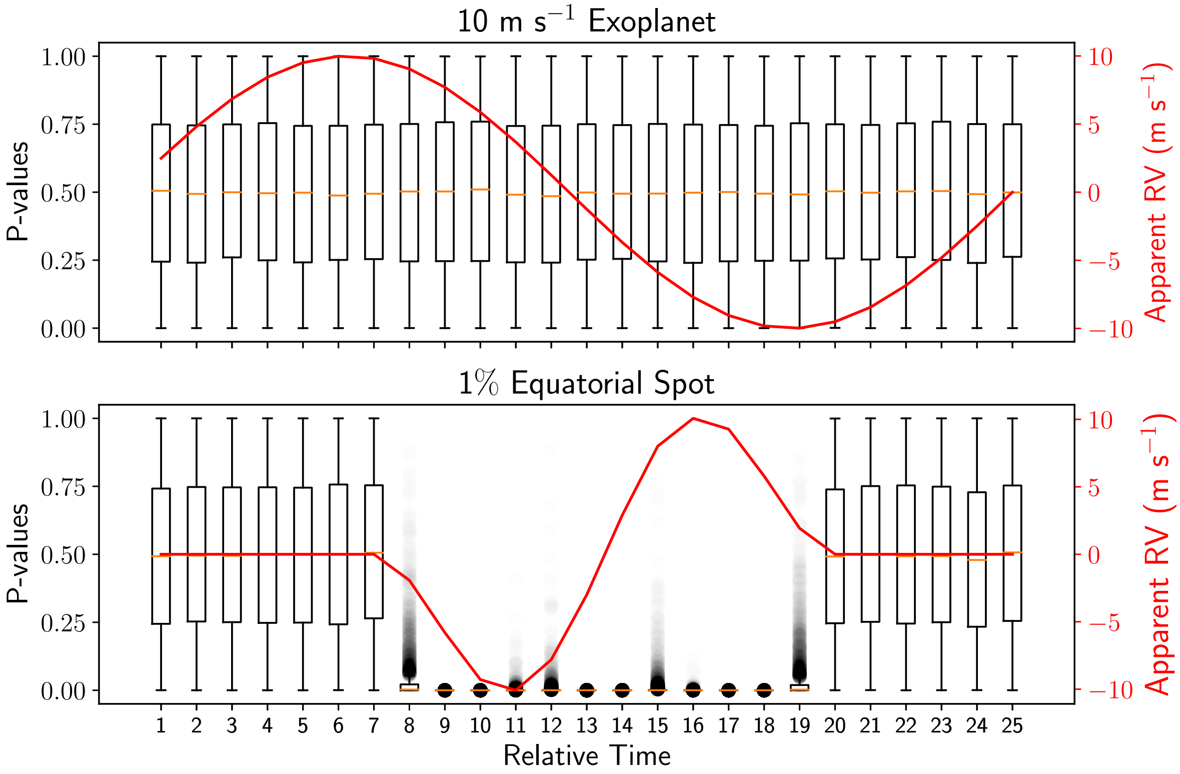

Figure 3.3: Results of doing $5,000$ simulations of adding SNR 150 noise to the spectrum at each time instance. The top panel is for the case of the only effect being due to a 10 m s^{-1} semi-amplitude Doppler shift from an exoplanet going through one complete circular orbit. The bottom panel is for the case of a 1% equatorial active region rotating around the star. At each relative time instance for both cases, the distribution of p-values is shown according to the left vertical axis. The detected radial velocity for each case is indicated with a smooth curve according to the right vertical axis as a way to indicate the phase of the orbit/rotation. The black circles indicate outliers, defined as points that are above the 75'th percentile by more than 1.5 multiples of the interquartile range of the p-values at the specified time.

SAFE and its corresponding p-value from the F-distribution 1000 times. We then estimate the power from the proportion of p-values that are below the 0.01 significance level. The results are shown in Figure 3.4.

Figures 3.3 and 3.4 illustrate that when the active region is near phase $120°$, $180°$, or $240°$, the power of the SAFE test is the highest. For further understanding of these phases, Figure 3.5 shows the estimated value of each coefficient in Equation (3.9) as a function of rotational phase according to a 500 SNR simulation of SOAP.

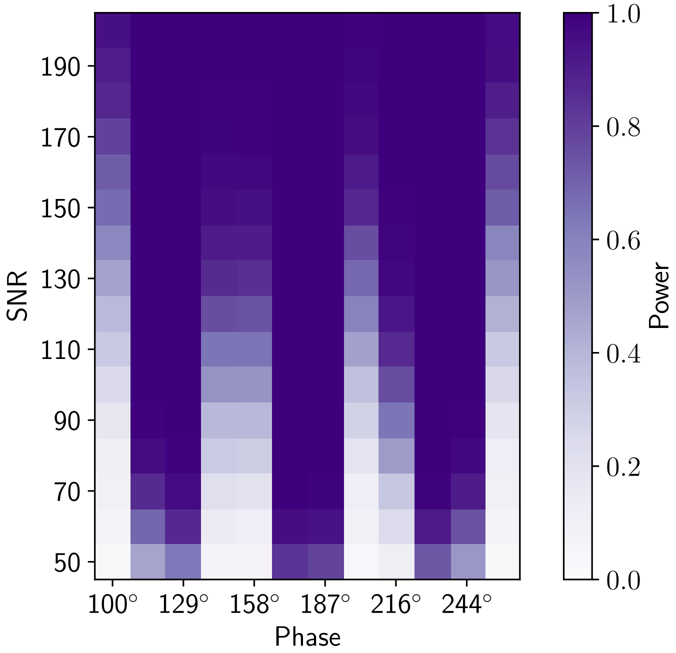

Figure 3.4: The power of the SAFE test, estimated by 1000 Poisson noise simulations, is plotted as a function of SNR and active region phase. The phases where the active region is behind the star are not included. The power is indicated by the colorbar on the right.

As illustrated in Figure 3.5, we find that the coefficients in Equation (3.9) with the largest t-statistic when fitted to these simulations are β_0 and β_2, which reach local extrema at the three phases $120°$, $180°$, and $240°$. This suggests that, after accounting for a Doppler shift, the most statistically significant characteristic of stellar activity according to SOAP is a symmetric change of absorption features.

We now compare the SAFE statistic to various other stellar activity indicator statistics in the literature, namely the BIS, BISlope, BiGauss, V-span, and FWHM. To do so we use the same spectra and simulation approach as we do for the SAFE above. Since these other indicators have not previously been used as hypothesis-test statistics for stellar activity in individual spectra, our first step is to estimate their null distribution. To do so we use 13000 independent simulations of adding Poisson noise to the SOAP spectrum where no stellar activity is present.

For a given phase and SNR level, we estimate the power of using each indicator specified

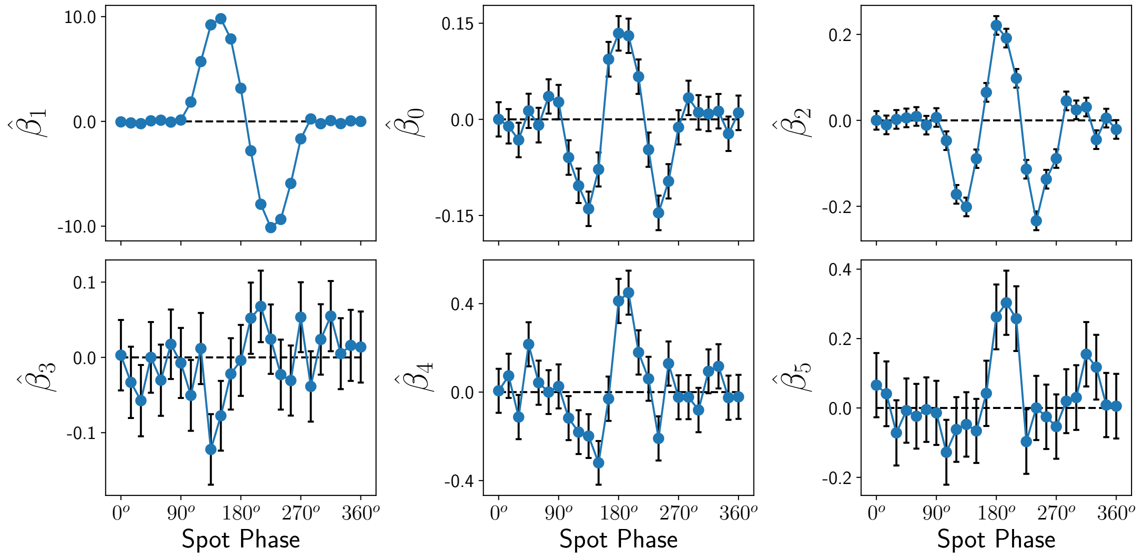

Figure 3.5: The values of the fitted coefficients in Equation (3.9) for a 500 SNR simulation of SOAP, plotted as a function of the rotational phase of the 1% equatorial active region. Each panel corresponds to one of the coefficients, beginning in the top left with $\hat{\beta}_1$ which represents the estimated RV in m s^{-1}. All five other coefficients are those included in the F-test that produces the SAFE. Error bars are also shown for each coefficient and phase. Note that the error bars for $\hat{\beta}_1$ are plotted, but small enough to not be visible.

above to conclude that there is statistically significant stellar activity present. We do so with the proportion of 1000 simulations that were either below the 0.5 percentile, or above the 99.5 percentile of the estimated null distribution (except in the case of the SAFE which is only statistically significant at large values, for which we calculate the proportion above the 99 percentile. The power results are illustrated in Figure 3.6.

Clearly, the FWHM and SAFE statistics have more power for detecting stellar activity than the BIS, BiSlope, BiGauss, and V-span in this simulation setting. This suggests that the most prominent effect of stellar activity, after accounting for an apparent Doppler shift, is a symmetric change to absorption features. Figure 3.7 gives a power comparison of the SAFE to that of the FWHM by showing the power difference.

Figure 3.7 illustrates that at various phases and low SNR the FWHM has higher power than the SAFE. But as the SNR increases to about 200, the SAFE becomes more powerful for most phases.

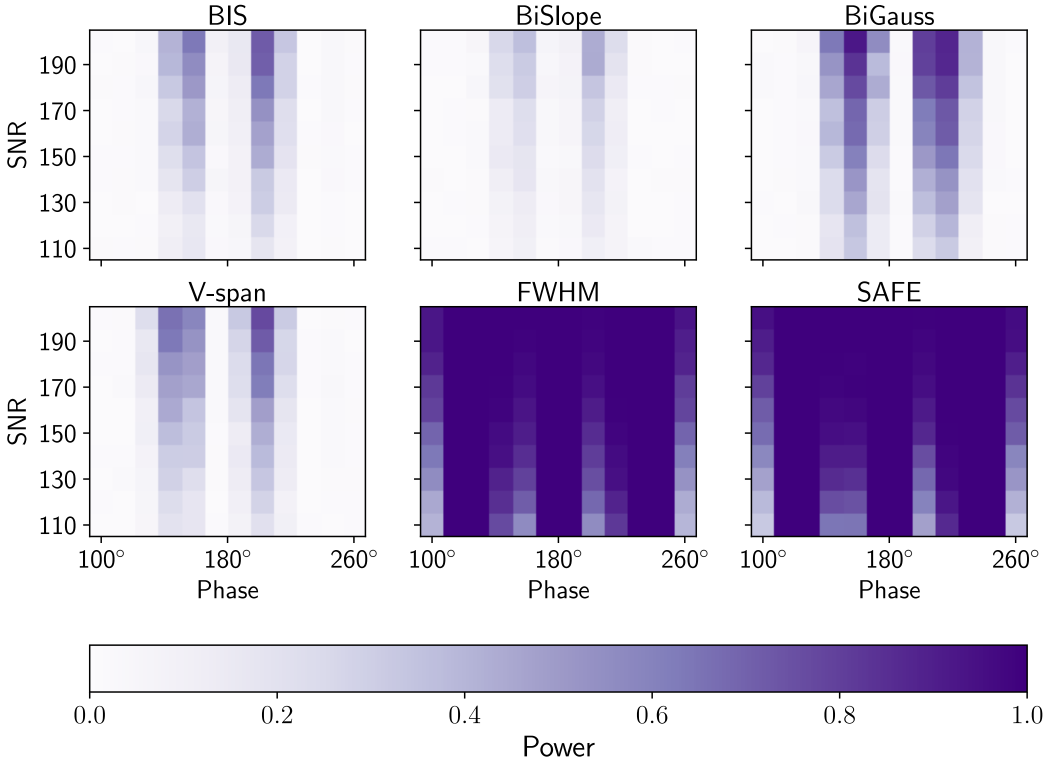

Figure 3.6: Power comparison of the BIS, BISlope, BiGauss, V-span, and FWHM stellar activity indicators to the SAFE. For each indicator, we show the power as a function of the active region's phase and SNR. The phases where the active region is behind the star are not included.

3.3.3 Template Estimation

We next simulate a set of spectra with the goal to check whether the SAFE null distribution is impacted by using an estimated template spectrum in place of the true template. To do so, we take the 106 observed spectra of Tau Ceti (described below in Section 3.4) and, for each time instance, replace the flux of each order with that of the corresponding wavelength region of a SOAP spectrum. The SOAP flux used for replacement has poisson noise with the same SNR as the corresponding Tau Ceti epoch. Depending on the epoch, these SNR range from

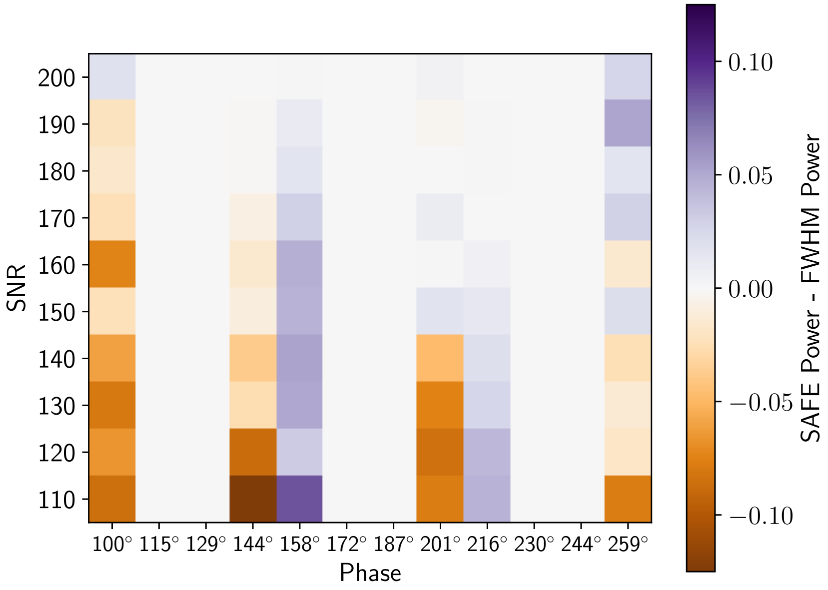

Figure 3.7: Power comparison of the SAFE and the FWHM stellar activity indicators. The difference in statistical power between the SAFE and FWHM is indicated by the color bar on the right (that is centered at zero), and is shown as a function of the active region's phase and SNR.

120 to 250, most of which are around 200. It also has a Doppler shift representing the same RV as estimated by the CCF for the corresponding Tau Ceti epoch. After applying the full method to this simulation, the p-values shown on the vertical axis of the uniform quantile-quantile plot of Figure 3.8 are given.[7] Since the coordinates do not step outside the 99% confidence bands, this gives support that the p-values for our simulation are approximately uniform. Therefore, we conclude that the template estimation does not significantly impact the null distribution of the SAFE. If the imperfect template estimation procedure had a strong influence on our ability to perform statistical inference about the SAFE, the data in Figure 3.8 would depart significantly from the diagonal.

---

[7] A uniform quantile-quantile plot shows the empirical quantiles of the sorted data on the vertical axis, plotted against the corresponding theoretical quantiles of the Uniform$(0, 1)$ distribution. The closer the data lie to the diagonal in the plot, the more the data resemble a uniform distribution. For sorted p-values $p_{(1)} \leq p_{(2)} \leq \ldots \leq p_{(N)}$, the corresponding theoretical quantile of $p_{(i)}$ is $q_i = (i - 0.5)/N$. The values of the $100(1 - \alpha)\%$ confidence band at q_i are given by the $\alpha/2$ and $1 - \alpha/2$ quantiles of the Beta$(i, N - i + 1)$ distribution.

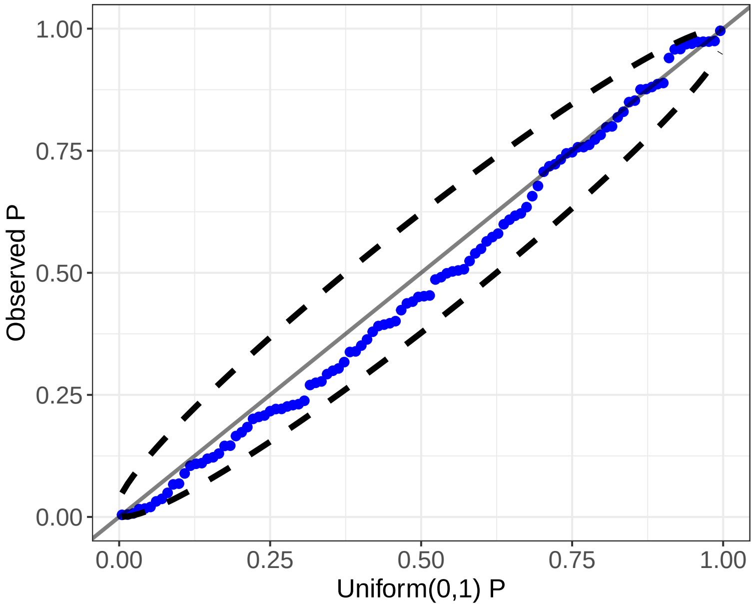

Figure 3.8: Uniform quantile-quantile plot with the empirical p-value quantiles from the SAFE simulation on the vertical axis, and the corresponding Uniform(0,1) quantiles on the horizontal axis. 99% confidence bands are shown in dashed black.

3.3.4 Realistic Stellar Activity

Activity on stars often include multiple active regions with variable sizes that change dynamically. We apply the proposed method to simulated spectra from Gilbertson et al. (2020a) that were generated using a more realistic active region model. The apparent RV induced by these models is on the scale of about 1 m s^{-1}, characteristic of stellar variability of the Sun. We randomly sample 100 of the 730 available epochs, reduce the resolution of each to 137500 to match the reported resolution of EXPRES (Petersburg et al., 2020), limit to the wavelength region between 5000 and 6500 Å, and decrease the SNR to 250. Using these 100 spectra we estimate the template spectrum and calculate the SAFE after subtracting off the fit of the median estimated coefficients over time. Figure 3.9 compares the SAFE to the area in micro-solar hemispheres (msh) of the visible stellar surface covered by active regions, projected onto the visible disk.

Figure 3.9 demonstrates that, under more realistic active region effects on Sun-like stars,

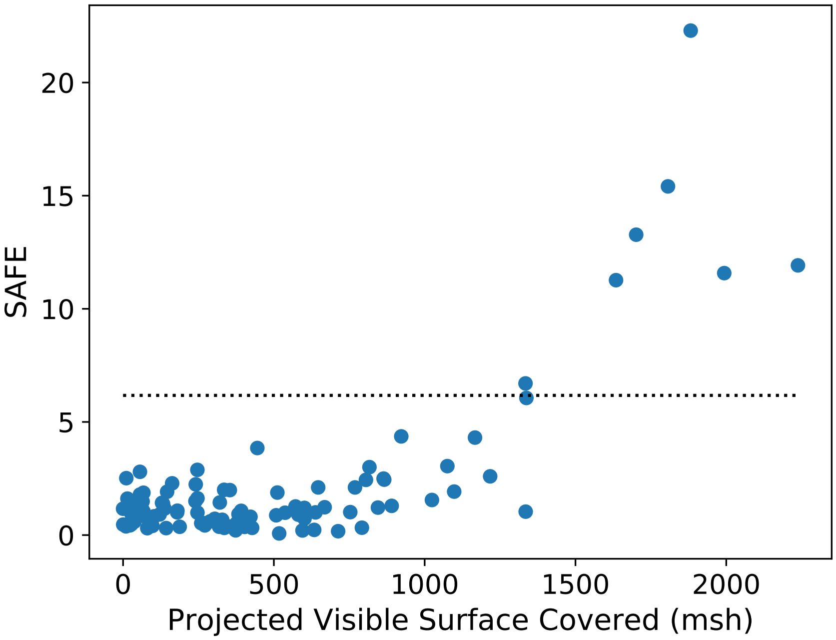

Figure 3.9: The calculated value of the SAFE plotted against the true projected micro-solar hemispheres (msh) on the visible surface of the star covered by active regions. The horizontal dashed line represents the critical value of SAFE after correcting for multiple testing, above which the p-value is less than 0.001.

the SAFE becomes statistically significant when the percent of the visible projected disk of the star covered by active regions is greater than approximately 0.15%. It also shows a noticeable monotonic association between the SAFE and the projected visible surface covered.

3.4 Applications to EXPRES Data

To test the performance of the SAFE on real data we use spectra recently collected by EXPRES for the stars HD 10700 (Tau Ceti), HD 22049 (Eps Eri), and HD 3651. Eps Eri is known to be a star with relatively high stellar variability (Kelch, 1978; Simon et al., 1980; Thatcher et al., 1991; Gray and Baliunas, 1995), whereas Tau Ceti (Gray, 1984; Saar and Donahue, 1997; Frick et al., 1997) and HD 3651 (Frick et al., 1997) are known to be relatively quiet. Our dataset consists of 106 spectra for Tau Ceti, 60 spectra for Eps Eri, and 52 spectra for HD 3651. These spectra were all collected in the later half of 2019.

Each of these spectra come with a barcentric corrected wavelength solution, normalized flux, and telluric models. Uncertainties for the normalized flux are also provided, which we use to determine the weights in the linear model for the SAFE.

3.4.1 Data Preprocessing

To mitigate the effects of tellurics, we mask out all pixels of each spectra where the telluric model normalized flux generated from selenite (Leet et al., 2019) is less than 1.0. We also use cubic spline interpolation to stitch the orders together, giving a single two-dimensional array of normalized flux and wavelength for each spectrum. We further limit the stitched spectra to be between 5000 and 7000 Å as the wavelength solution is known to be increasingly less accurate outside this range.

Although the spectra are provided with the continuum normalized, we find that an additional normalization step is needed to remove remaining trends in the continuum, particularly near the edges of orders. To further adjust the normalization the Absorption Feature Finder (AFF) algorithm of Chapter 3 is used with a small width parameter to identify as many potential absorption features as possible. The portions of the spectra that do not lie inside any of the detected absorption feature wavelength bounds are then used as windows of the continuum. Because the AFF algorithm can sometimes miss absorption features, any of the remaining pixels that have a normalized flux more than one multiple of the interquartile range below the 25th percentile of the remaining subset are removed. A running median is then applied to estimate the remaining continuum to be divided out. Finally, we adjust the wavelength axis of each spectrum by dividing out the apparent Doppler shift using the RV estimated by the EXPRES pipeline which, as previously noted, need only be within 5 m s^{-1} of the true velocity. This allows for a more accurate estimation of the template spectrum (described in Section 3.3.3) that has minimal broadening of absorption features.

3.4.2 Calculating SAFE

For each of the spectra we first estimate a template spectrum using the nonparametric approach described in Chapter 3. Because replacing hardware or other components of the instrumentation can effect the spectrum in ways that lead to a statistically significant value of SAFE, separate estimates of the template spectrum before and after such changes is recommended. Such changes took place in August 2019 following 47 (of the total 106) observations of Tau Ceti. These updates helped improve the stability of the laser frequency comb by replacing the photonic crystal fiber and changing the polarization of the light. (All observations of Eps Eri and HD 3651 came after these changes.) Therefore, we estimated two separate template spectra for Tau Ceti using the approach described in Section 3.3.3.

For each of these template spectra, we obtain estimates $\hat{\mu}_i$ and $\hat{\sigma}_i$ for each feature using the process described at the beginning of Section 3.2.1.[8]

We then perform weighted least squares with the difference flux according to Equation (3.9). Occasionally, we find that there are strong outliers present in the regression, mostly due to absorption features with a poor algorithmic convergence of fitting a Gaussian and failing to be eliminated as described in the preceding paragraph. Consequently, we also remove points at time t that have an influence[9] greater than 50 multiples of the interquartile range above the 75'th percentile of all the influence values at time t. We find that such strong influence points rarely occur and are usually due to cosmic rays. Before calculating the

---

[8] For the HD 10700 template spectrum before the instrumental changes in August 2019, 1191 of the 2297 features remained after these criteria. For the HD 10700 template spectrum after the instrumental changes, 1128 of the 2172 features remained. Out of the 2302 features for HD 3651, 871 remained. And HD 22049 had 877 of its 2309 features remain.

[9] For a linear model $Y = X\beta + \varepsilon$, with design matrix X and response vector Y, the vector of fitted values is $\hat{Y} = X\left(X^TX\right)^{-1}X^TY = HY$. The influence of the i'th data point, which will be relatively far from zero if $X_{i,\cdot}$ is an outlier, is given by the expression $\dfrac{\left(Y_i - \hat{Y}_i\right)H_{i,i}}{1 - H_{i,i}}$.

SAFE according to Equation (3.10) for all observed spectra we make one final adjustment to the template spectrum by taking the median value of each fitted coefficient $\hat{\beta}_{i,t}$ across time, calculating the median difference flux from the median coefficients, and subtracting the median difference flux from the estimated template. This helps to further correct for the bias present in the estimated template spectrum. Using this adjusted template to calculate the difference flux for each normalized spectrum, we then fit the coefficients and calculate the SAFE_t at each time t.

3.4.3 Results

Figure 3.10 shows the distribution of the (log) SAFE for Eps Eri, Tau Ceti, and HD 3651. This illustrates that, as expected, Tau Ceti and HD 3651 mostly have values of SAFE that are not statistically significant, occasionally showing a significant stellar activity signal. On the other hand, the large majority of Eps Eri observations gave a value of SAFE above the critical value.

As further evidence that the SAFE statistic is detecting stellar activity in the spectra for Eps Eri, Figure 3.11 shows the SAFE plotted against the Modified Julian Date (MJD). Since stellar variability in the form of active regions changes on the order of days, we would expect to find similar values of SAFE for observations taken in the same night.

For Eps Eri we find that the standard deviation of the SAFE between nights (34.5) is approximately six times larger than the standard deviation within nights (5.78). Furthermore, we did not find any noticeable association between the SAFE statistic and any of the weather conditions provided by EXPRES: cryostat temperature, cryostat pressure, angular distance of the moon, angular distance of the Sun, airmass, and exposure time.

We also analyzed the star HD 34411, one of the most frequently observed stars in the EXPRES pipeline. With a total of 173 spectra ranging from (barycentric) MJD 58437 to 59135 we calculated the SAFE with the same procedure previously described with initial

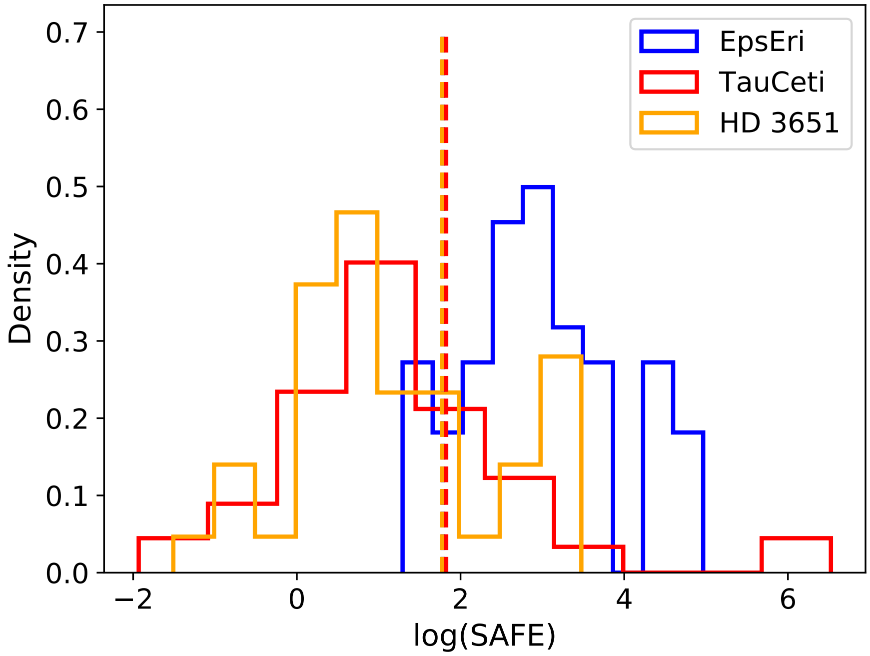

Figure 3.10: Histograms representing the distribution of the natural log of SAFE for the three stars Eps Eri (blue), Tau Ceti (red), and HD 3651 (yellow). The (multiple testing corrected) critical value for a significance level of 0.001, above which represents statistically significant values of SAFE, is shown by the vertical dashed line. Note that all three stars appear to have approximately the same critical value in this plot.

RV estimates given by the method of Chapter 3. A total of 24 of the observations produced a statistically-significant value of the SAFE.

As a first step of extending the use of the SAFE for correcting the RV measurements to be less influenced by stellar activity, we suggest simply removing observations that we conclude have a statistically-significant stellar activity signal present.[10] For HD 34411, by eliminating the 33 observations where the SAFE is above the critical value or occur on the same night as an observation with a very large value of SAFE (i.e., greater than 10), we find that the root mean squared deviation from the average RV decreases from 2.08 m s^{-1} to 1.72 m s^{-1}. This represents an improvement of estimated RV precision of approximately

---

[10] We acknowledge that this approach of simply eliminating observations is likely to not work well on very active stars where nearly all observations have a statistically-significant stellar activity signal.

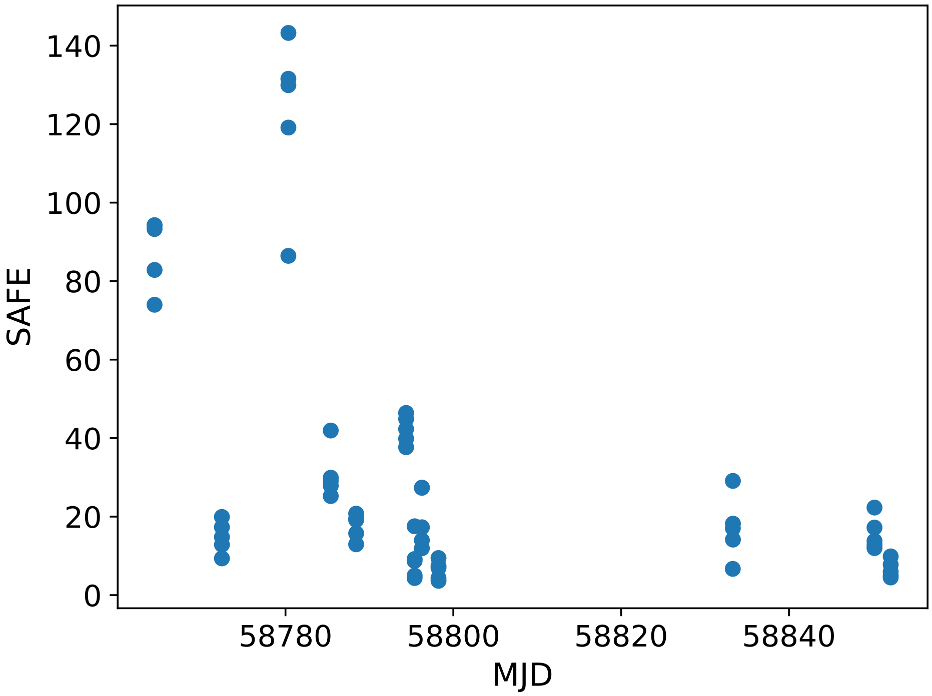

Figure 3.11: Scatterplot of the SAFE against the (barycentric) MJD for observations of Eps Eri (HD 22049). The scatter between nights is greater than the average scatter within nights, which is expected for stellar activity indicators.

17%.

3.5 Discussion

The proposed SAFE statistic aims to detect any shape change in spectral absorption features that is not due to a Doppler shift. Under the assumption that the line spread function is stable and all instrumental effects have been properly corrected for, the only remaining source of absorption feature shape changes is stellar variability in the observed star. In this sense, the SAFE can be thought of as a combination of many classical stellar activity indicators. This is because it is composed of a linear combination of Hermite-Gaussian functions, ψ_n. For a single absorption feature a change in the line depth would be characterized with ψ_0. ψ_2

would represent a change in the line width, similar to the FWHM. A change in skewness would result in some linear combination of ψ_3 and ψ_5, similar to the BIS, BiSlope, V-span, and BiGauss. And ψ_4 helps to represent a change in line kurtosis. Therefore, instead of trying to detect a specific type of change due to stellar activity, the SAFE aims to detect any change in line shape that is not due to a simple Doppler rescaling of the wavelength axis.

Compared to the many other stellar activity indicators, the SAFE is unique in that it's null distribution is well known. Consequently, it allows for testing the hypothesis that no stellar activity is present.

One of the benefits of building the SAFE with a linear model comes from the fact that rarely, if ever, is there just one active region or form of stellar activity on a given star. Under the assumption that the cumulative effect of multiple active regions is just the superposition of each individual active region, a linear model allows for not knowing the number of active regions in advance. Active regions are also known to vary in size. Assuming that the effect of a different sized active region would just be a rescaling of the difference flux imposed on each absorption feature, a linear model also allows for not knowing the size of each active region.

Unlike in Chapter 3, we do not assume absorption features are Gaussian. This allows for using spectral lines with significantly broadened wings. It also means we do not need to avoid blended spectral lines. Instead we assume that each absorption feature's difference flux due to a Doppler shift can be decomposed as a linear combination of the Hermite-Gaussian functions up to degree 5. Consequently, we are unable to mathematically quantify how small of an RV is small enough for our assumptions to be met; our simulations suggest that a RV of 10 m s^{-1} is within the acceptable range. Furthermore, the Hermite-Gaussian functions are not the only basis one could choose for calculating the SAFE. We prefer this basis because it is smooth, localized, and composed of even and odd functions.

As mentioned above, the SAFE is calculated from using a large portion of the spectrum. By dropping the assumption of Gaussian-shaped absorption features, we are able to use more features found by the AFF algorithm compared to when the Gaussian-shape assumption is used. While we do use the continuum in our renormalization as part of the data preprocessing, only pixels corresponding to absorption features are used in the regression model used for calculating the SAFE.

The dimensional reduction we perform using rPCA over each degree of Hermite-Gaussian coefficients for SOAP spectra can be considered a way of quantifying how strongly certain absorption features are affected compared to others. The ability of the SAFE to detect statistically-significant stellar activity signals in Eps Eri spectra indicate that the relative amplitudes given by rPCA on SOAP spectra are accurate enough to extend to real data. However, it remains unknown how well such relative amplitudes will do at detecting stellar variability in stars that are very different than the Sun. Furthermore, the amplitudes may need to be adjusted if one aims to detect other forms of stellar variability than active regions. For example, since very few of the observations of Tau Ceti gave a statistically significant SAFE, but all were (intentionally) collected in a short time interval that likely did not wash out the signal of pressure mode oscillations (Chaplin et al., 2019), this suggests that the relative amplitudes are not tuned to detecting this type of stellar variability.

For the simulation studies of SAFE, as well as the applications to stars observed by EXPRES, we find that the coefficient of Ψ_2 is the most statistically significant when calculating the SAFE. This suggests that the most noticeable difference between a Doppler shift and a signal from an active region is the symmetric change represented by a multiple of ψ_2. Therefore, as illustrated in Figure 3.12, we do not expect the SAFE to be correlated with the apparent RV due to an active region.

Because the SAFE is not expected to be correlated with the apparent RV, it is primarily designed to detect, rather than directly correct for, the presence of stellar activity. However, the SAFE or the individual fitted coefficient values of Equation (3.9) may still be used to help correct the apparent RV by including it in a time-series model such as that of Rajpaul et al. (2015) or Jones et al. (2017).

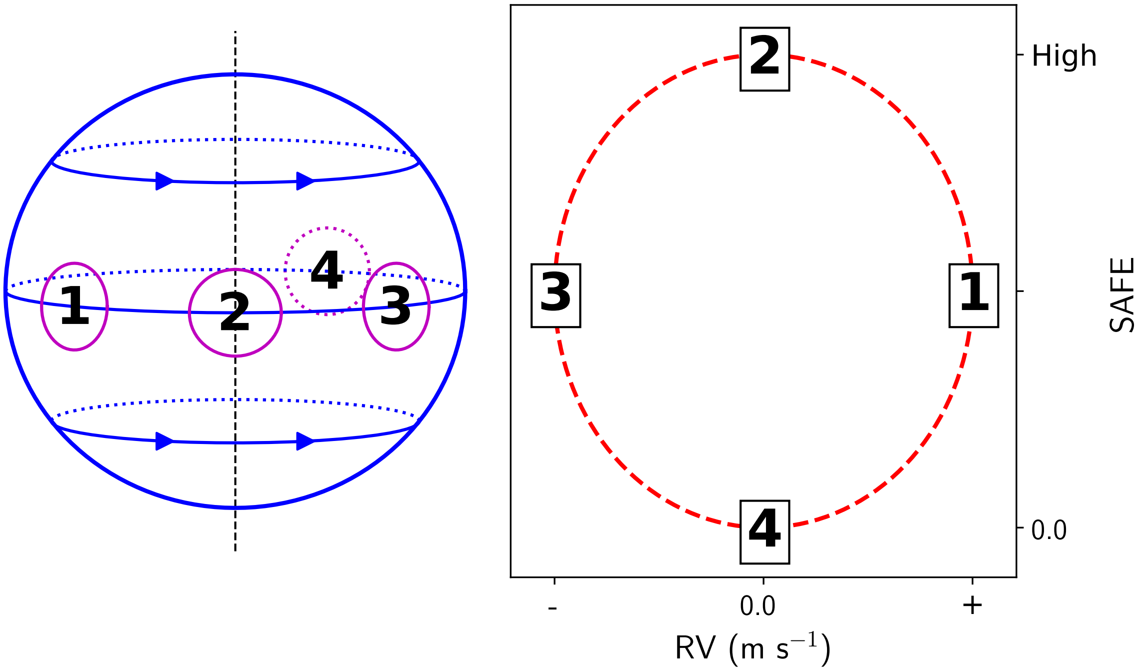

Figure 3.12: Visual graphic representing qualitatively why we do not expect the SAFE to be correlated with the apparent RV due to an active region. The sphere on the left represents a star with four sequential phases of an equatorial active region. Solid lines represent the visible side of the star and dotted lines represent the back. The plot on the right shows the expected behavior of the SAFE and RV for each of the four phases. For a different sized active region, the coordinates of the four points in the right panel would simply be scaled by a certain factor. Note that state **4** is for when the active region is completely on the non-visible side of the star.

While the approach for cleansing the RV measurements of stellar activity by simply removing observations with a large value of SAFE may be useful for stars with intermittent activity, it would result in rejecting a large fraction of data for other stars that frequently have detectable levels of stellar activity. Therefore, future studies should investigate whether the SAFE statistic or the $\hat{\beta}_d$ coefficients could be used to predict the RV perturbation due to stellar activity and provide an improved estimate for the RV. As a first step in this direction, we investigated the ability of these coefficients calculated from half a year of simulated solar data (Gilbertson et al., 2020a) to perform this task. It is unclear how the coefficients will map onto RV contamination, so we fit a version of the multivariate GP model described in

Gilbertson et al. (2020b) to the $\hat{\beta}_1$ coefficients (which represent initial RV estimates) and the first two series of PCA scores created from the $\hat{\beta}_0$, $\hat{\beta}_2$, and $\hat{\beta}_3$ components. We found that, once the model hyperparameters were fit, conditioning the posterior of the model on only the stellar activity information (i.e., no RV information) removed over half of the variance in the RV measurements contributed by the stellar variability. Thus, the use of SAFE coefficients to improve the precision of RV measurements in the presence of stellar variability appears to be a promising avenue for future research.

A number of improvements could potentially be made to the methodology of calculating the SAFE. The assumption made about the noise being independent is not necessarily true due to the point spread function of the spectrograph. Adjusting for this by using a non-diagonal covariance matrix in the linear model of Equation (3.9) would help account for this. Another improvement would be to include Ψ_1 in the model and test if the coefficient of this additional term is also simultaneously zero. This would potentially allow the SAFE to more easily detect antisymmetric shape changes in absorption features due to stellar variability. While Ψ_1 is not included due to potential collinearity, this issue may be avoidable by formulating the regression in a Bayesian framework. Including Ψ_d for $d > 5$ may also help improve the SAFE.

While a good number of absorption features were removed in this work, the SAFE has the potential to be calculated from nearly all spectral features. If the continuum normalization were to be done with high accuracy, and complicated absorption features could be well modeled, then many more such features could be included in the linear model. This could increase the statistical power of the SAFE even further.

Finally, an improvement that we suspect will greatly improve upon this work is to account for effects of stellar activity that are not shared across most absorption features. Our use of relative amplitudes in building the explanatory variables for the regression model of Equation (3.9) essentially limits the SAFE to detecting spectrum-wide effects. But it is well known that some absorption features are much more sensitive to stellar activity than others (Dumusque, 2018; Wise et al., 2018; Ning et al., 2019). Including additional terms in Equation (3.9) for such activity-sensitive spectral lines could allow the SAFE to detect both spectrum-wide and feature-specific effects simultaneously.

3.6 Conclusion

We introduce a new stellar activity indicator called the SAFE, which is an F-statistic for a linear model of a spectrum's difference flux on sums of Hermite-Gaussian functions centered on absorption features. Through simulation we demonstrate that the SAFE follows the assumed F-distribution, is not affected by a Doppler shift, and is associated with the area of the visible projected surface covered by active regions. We also compare the statistical power of many classical stellar activity indicators and find that the SAFE and FWHM perform the best. Furthermore, the SAFE is estimated on a set of spectra recently collected by EXPRES from HD 22049, HD 10700, and HD 3651. HD 22049 is known to be very active and results in statistically significant values of SAFE in almost all of the spectra. Additionally, the other two stars, known to be relatively inactive, only occasionally have statistically significant stellar activity detected by the SAFE. Overall, the SAFE is a new stellar activity indicator that detects stellar variability with high power and appears to show promise of being useful in disentangling such signals from exoplanet-induced Doppler shifts. Data and code associated with this work is accessible in the following repository: https://github.com/parkerholzer/safe_statistic.

Chapter 4

Doppler-Orthogonalized Regression for Correcting Stellar Activity

4.1 Motivation

In Chapter 3 we introduced a general method designed to at least partially correct for the effects that stellar activity signals impose on radial velocity estimates. This involved adding higher-degree Hermite-Gaussian functions to the regression model introduced in Chapter 2 that are orthogonal to the main variable representing a Doppler shift. But even though adding these higher-degree functions to the model produces an F-statistic that we found to be more powerful than traditional stellar activity indicators, it is only designed to detect the presence of stellar activity. Ideally, we would have a statistic that helps to remove the stellar activity signal, preventing the need to eliminate entire spectra that are found to have significant stellar activity.

One way this may be accomplished is by adding a variable to the linear model introduced in Chapter 2 that is (i) orthogonal to the original Doppler variable and (ii) linearly associated with the effect of stellar activity. While the approach of Chapter 3 accomplishes the first of these two criteria, it does not appear to accurately fulfil the second. This is primarily because the SAFE statistic is primarily driven by the even-degree Hermite-Gaussian functions which are symmetric across individual absorption features. On the other hand, the effect of a small Doppler shift can be almost completely modeled as an asymmetric change to absorption features. Therefore, the portion of a stellar activity signal that we wish to remove is also composed of asymmetric effects. Even though it is possible that a symmetric effect of stellar activity might be able to predict the false RV signal induced, it is much more likely that an asymmetric effect would serve this purpose. Overall, it is likely that the full asymmetric effect of stellar activity on individual absorption features is not exactly the same as that of a Doppler shift. Therefore, we wish to use the portion of this asymmetric effect that is orthogonal to a Doppler shift to predict and remove the apparent Doppler shift that is only due to stellar activity.

4.2 Simulation Studies

4.2.1 Individual Absorption Features

We begin by first analyzing a single absorption feature in the quiet spectrum of the Spot Oscillation and Planet 2.0 (SOAP) simulations (Dumusque et al., 2014). With $\tilde{x}$ representing the wavelength of light, let $f(\tilde{x})$ represent the normalized flux of $\tilde{x}$ with no noise or astrophysical effects. Here we relax the assumption made in Chapter 2 that f is a Gaussian, and replace it with the assumption that its derivative $f'(\tilde{x})$ can be accurately estimated. It is well known that the difference flux y due to a small Doppler shift from a RV v is given by

$$y = \frac{v}{c}\tilde{x}f'(\tilde{x}) \tag{4.1}$$

where c is the speed of light. Defining $x_1 = \frac{1}{c}\tilde{x}f'(\tilde{x})$, let $\boldsymbol{x}_1 = (x_{1,1}, x_{1,2}, ..., x_{1,n})^T$ be the vector of transformed wavelengths for a particular absorption feature. If a Doppler shift were the only astrophysical effect on the stellar spectrum, then we could apply simple linear regression without an intercept to $\boldsymbol{y} = (y_1, y_2, ..., y_n)^T$, the vector of observed difference flux, using Equation (4.1) and estimate v. However, since stellar activity can also affect the $\boldsymbol{y}$ in a way similar to $\boldsymbol{x}_1$, we wish to include an additional variable in the linear model that accounts for stellar activity.

To still allow the model to accurately detect a true Doppler shift, the additional variable must be orthogonal to $\boldsymbol{x}_1$. Furthermore, its coefficient must be correlated with that of $\boldsymbol{x}_1$ in the case of only stellar activity being present. Since $f(\tilde{x})$ is approximately symmetric usually, $f'(\tilde{x})$ is nearly asymmetric. And since $\tilde{x}$ changes very little across a single absorption feature compared to $f'(\tilde{x})$, $\boldsymbol{x}_1$ is nearly asymmetric about the central wavelength μ of the absorption feature. Therefore, we construct the additional variable so that it is also asymmetric about μ.

We begin by defining $\boldsymbol{w} = (\tilde{x}_1 - \mu, \tilde{x}_2 - \mu, ..., \tilde{x}_n - \mu)^T$, where $\tilde{x}_i$ is the raw wavelength of pixel i. The vector $\boldsymbol{w}$ can be viewed as the identity function about the central wavelength of an absorption feature, evaluated at a set of discrete wavelengths. This identity function is the simplest variable that accomplishes the asymmetric property we desire. To orthogonalize $\boldsymbol{w}$ with $\boldsymbol{x}_1$ we use the Gram-Schmidt method. Overall, we define

$$\boldsymbol{x}_2 = \boldsymbol{w} - \frac{\boldsymbol{w} \cdot \boldsymbol{x}_1}{||\boldsymbol{x}_1||_2^2} \boldsymbol{x}_1 \tag{4.2}$$

which is also nearly antisymmetric about μ since the difference between two odd functions is also odd. An example of an absorption feature in the quiet SOAP spectrum, together with $\boldsymbol{x}_1$ and $\boldsymbol{x}_2$ as defined above, is shown in Figure 4.1.

Our final model for the difference flux of an absorption feature then becomes

$$\boldsymbol{y} = v\boldsymbol{x}_1 + \beta \boldsymbol{x}_2 + \varepsilon \tag{4.3}$$

where $\varepsilon \sim \text{Normal}(0, \sigma)$.

Upon fitting the model in Equation (4.3) and getting estimates $\hat{v}$ and $\hat{\beta}$, we intend to use $\hat{\beta}$ to help remove the false RV from $\hat{v}$. Because stellar activity in the form of starspots

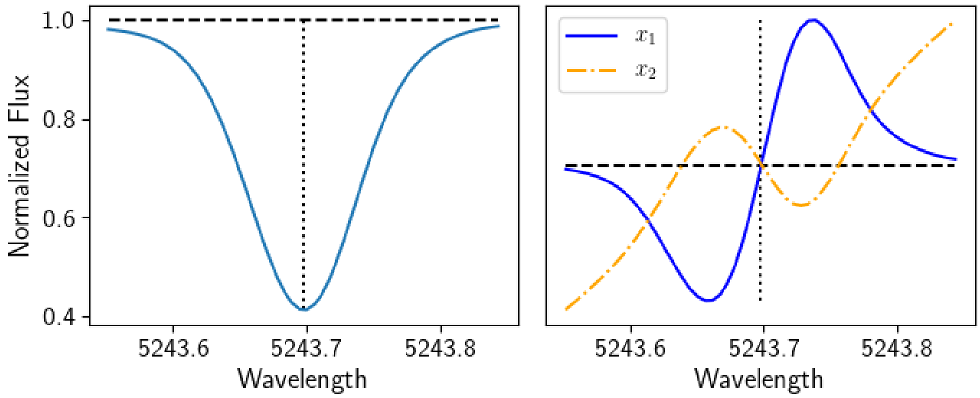

Figure 4.1: A single absorption feature from the quiet SOAP spectrum is shown on the left panel with the continuum indicated by a dashed line. The constructed explanatory variables $\boldsymbol{x}_1$ and $\boldsymbol{x}_2$ are visualized in the right panel with the horizontal dashed line indicating zero. The dotted vertical line is drawn at the feature's central wavelength μ.

can take a wide variety of sizes, and therefore impose different amounts of false RV signals on the stellar light, we wish to make our method of correcting $\hat{v}$ general enough to account for this. Furthermore, we wish to allow for the presence of any number of starspots, the combined effect of which we assume is the superposition of each individual spot. Allowing for these realistic scenarios, we focus the remainder of this work on removing the portion of the false RV that is a constant multiple of $\hat{\beta}$. Figure 4.2 illustrates how $\hat{v}$ and $\hat{\beta}$ change over time with respect to each other. The results for using the best constant multiple of $\hat{\beta}$ to correct $\hat{v}$ are also shown in Figure 4.2 for the two scenarios of an exoplanet-induced Doppler shift and a equatorial star spot.

Figure 4.2 demonstrates that correcting $\hat{v}$ using $\hat{\beta}$ does not affect the signal of a true exoplanet-induced Doppler shift; the sum of squares of the corrected RV's in the exoplanet scenario is less than 0.01% different from that of the raw RV's. On the other hand, while the correction does not remove all the RV signal, the sum of squared RV's is reduced by 57.05% when using the corrected RV's instead of the raw estimates in the scenario of a star spot. While the amount by which the RV estimate is corrected depends on the phase of the star spot, the overall signal is significantly reduced. Figure 4.2 suggests that the RV

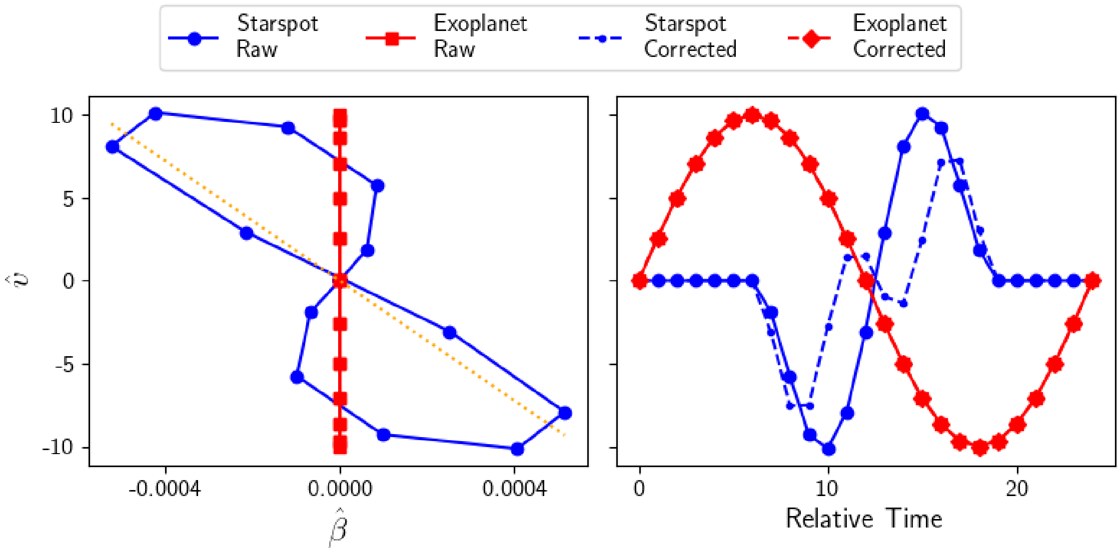

Figure 4.2: Using the single absorption feature shown in Figure 4.1, the left panel shows how $\hat{v}$ and $\hat{\beta}$ change over time with respect to each other in the two scenarios of an exoplanet and a star spot. The best approximation of $\hat{v}$ as a constant multiple of $\hat{\beta}$ is also shown in dotted orange. With the same vertical axis, the right panel shows how $\hat{v}$ changes over time in both scenarios, as well as what the behavior of the estimated RV corrected using the constant multiple of $\hat{\beta}$ is. The exoplanet scenario is indicated by solid squares and dashed diamonds for the raw and corrected RV's respectively. The raw and corrected RV's from a star spot are shown in solid large circles and dashed small circles respectively.

correction from a star spot is most difficult when the spot is near the limbs of the star. This likely is due to the well-known astrophysical effect referred to as limb darkening, where the observed light of the star's limbs is physically dimmer than that of the center (as seen by the viewer).

We then apply the same approach to all the absorption features identified in the quiet SOAP spectrum by the Absorption Feature Finder (AFF) algorithm from Chapter 2. For the majority of the absorption features we get results that are quite similar to those shown in Figures 4.1 and 4.2. However, while all features avoid removing any of the RV signal in the case of a exoplanet-induced Doppler shift, there are a number of features that do not appear to help remove the false RV signal from a star spot. Suspecting that this may be due to many absorption features being blended with neighboring features, we define three external blend indexes[1]:

$$B_{\text{full}} = \frac{f\left(\max \mathcal{X}\right) - f\left(\min \mathcal{X}\right)}{\max\limits_{\tilde{x} \in \mathcal{X}} f(\tilde{x}) - \min\limits_{\tilde{x} \in \mathcal{X}} f(\tilde{x})}, \tag{4.4}$$

$$B_{\text{left}} = \frac{1 - f\left(\min \mathcal{X}\right)}{1 - \min\limits_{\tilde{x} \in \mathcal{X}} f(\tilde{x})}, \tag{4.5}$$

$$\text{and} \quad B_{\text{right}} = \frac{1 - f\left(\max \mathcal{X}\right)}{1 - \min\limits_{\tilde{x} \in \mathcal{X}} f(\tilde{x})} \tag{4.6}$$

where $\mathcal{X}$ is the set of wavelengths corresponding to the absorption feature of interest and f is the normalized flux. Calculating B_{full}, B_{left}, and B_{right} for each feature with Equations (4.4), (4.5), and (4.6) respectively, we compare them to the ratio of corrected and uncorrected sum of squared RV's in the star spot scenario with Figure 4.3.

Figure 4.3 demonstrates that often when the RV correction from our method is poor, the feature has a blend index that is far from zero. Consequently, we remove absorption features where any blend index is high.[2] The distribution of the ratio of corrected and uncorrected sum of squared RV's for the remaining features is shown in Figure 4.4.

The histogram for the exoplanet scenario in Figure 4.4 demonstrates that the RV correction hardly affects the signal for all absorption features considered. On the other hand, especially for the features with low blend index values, the correction reduces the star spot RV signal by roughly $40 - 60\%$ for most features.

---

[1] A blend between two absorption features is considered "external" when the wavelength intervals of the features overlap significantly, but the AFF algorithm can still distinguish them as different features. Such a blend could lead to (i) a difference between the normalized flux measurements at the highest and lowest wavelengths of the feature that is significantly nonzero or (ii) the normalized flux of the feature being well below 1.0 at either endpoint of the feature's wavelength interval. These provide some intuition for our definitions of external blends. If the overlap is significant enough that the AFF algorithm detects only one feature, then the blend would be considered "internal".

[2] An absorption feature where either $|B_{\text{full}}| > 0.25$, $B_{\text{left}} > 0.5$, or $B_{\text{right}} > 0.5$ is considered to have a high blend index. These cutoffs were not chosen rigorously, however, and could potentially be improved.

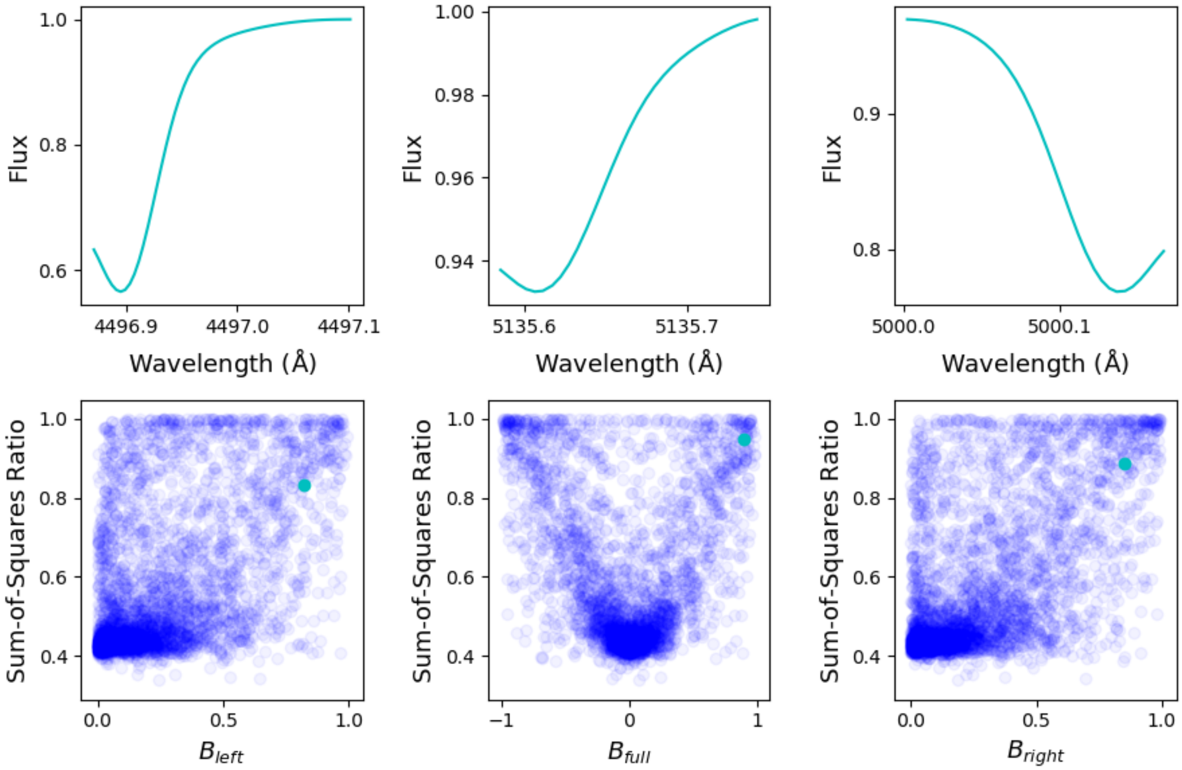

Figure 4.3: Comparison of the sum-of-squares ratio between corrected and uncorrected RV estimates for an equatorial star spot and the three blend indexes B_{full}, B_{left}, and B_{right}. The bottom three panels show the sum-of-squares ratio plotted against each blend index, each point representing a single absorption feature in the quiet SOAP spectrum. The top three panels give an example of a feature with a high blend index, the point of which is also shown in the panel below in cyan.

4.2.2 Full Spectrum

Ultimately, both the Doppler signal and the star spot signal are too small to estimate in individual absorption features with realistic noise. Consequently, we must combine absorption features when estimating the RV. Furthermore, we adjust the model in Equation (4.3) so that the coefficient v is the corrected, instead of the raw, RV estimate.

With $\boldsymbol{x}_{1,k}$, $\boldsymbol{x}_{2,k}$, and $\boldsymbol{y}_k$ representing the Doppler variable, stellar activity variable, and difference flux respectively for absorption feature k as above, we first define $\boldsymbol{X}_1 = \left(\boldsymbol{x}_{1,1}^T, \boldsymbol{x}_{1,2}^T, ..., \boldsymbol{x}_{1,K}^T\right)^T$, $\boldsymbol{X}_2 = \left(\boldsymbol{x}_{2,1}^T/\gamma_1, \boldsymbol{x}_{2,2}^T/\gamma_2, ..., \boldsymbol{x}_{2,K}^T/\gamma_K\right)^T$, and $\boldsymbol{Y} =$

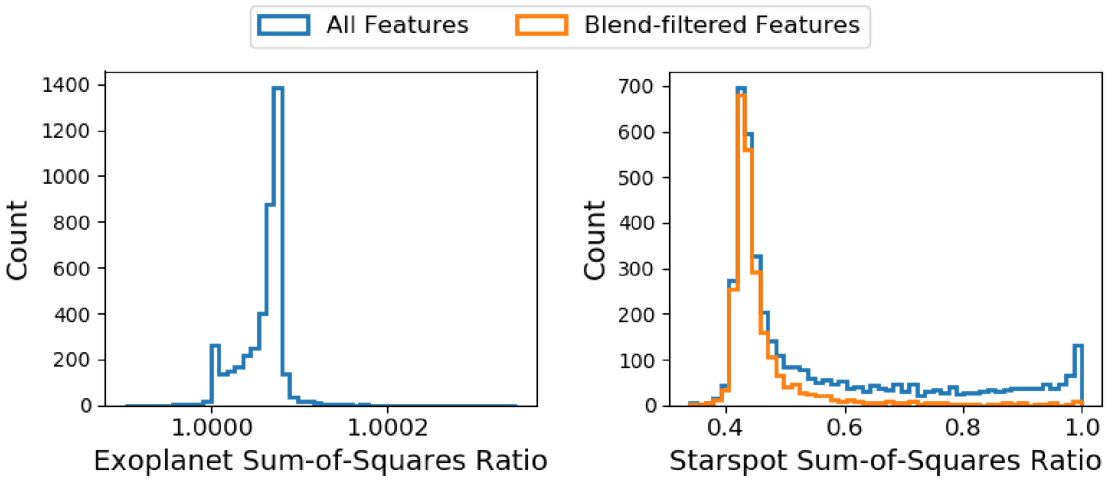

Figure 4.4: The distribution of the ratio between corrected and uncorrected sum-of-squared RV's in the case of an exoplanet-induced RV signal is shown in the left panel. For the RV signal due to a star spot the distribution of the ratio is shown on the right, which compares the cases of including all absorption features and only those with low blend index values.

$\left(\boldsymbol{y}_1^T, \boldsymbol{y}_2^T, ..., \boldsymbol{y}_K^T\right)^T$. Here, γ_k is the constant multiple that best relates the coefficient of $\boldsymbol{x}_{2,k}$ to that of $\boldsymbol{x}_{1,k}$ from Section 4.2.1, an example of which is shown in the left panel of Figure 4.2. Now, by setting $\boldsymbol{X}_3 = \boldsymbol{X}_1 + \boldsymbol{X}_2$, we have the combined model

$$\boldsymbol{Y} = v_{\text{Dopp}} \boldsymbol{X}_1 + v_{\text{spot}} \boldsymbol{X}_3 + \boldsymbol{\varepsilon} \tag{4.7}$$

where $\boldsymbol{\varepsilon}$ is multivariate normal. The coefficients v_{Dopp} and v_{spot} now represent the RV due to an exoplanet-induced Doppler shift and a star spot respectively.

Using the quiet SOAP spectrum, we simulate a set of spectra with a sinusoidal RV signal from an exoplanet. We then add Poisson-like noise to each spectrum at various SNR levels. Using the features with low blend index values to construct $\boldsymbol{X}_1$ and $\boldsymbol{X}_3$, we fit the model in Equation (4.7) which gives the results shown in Figure 4.5.

Similarly, we use the time series of SOAP spectra that simulates a 1% equatorial spot rotating around the Sun beginning and ending at the back. Using the same model, the estimated coefficients in Equation (4.7) for various SNR levels are shown in Figure 4.6.

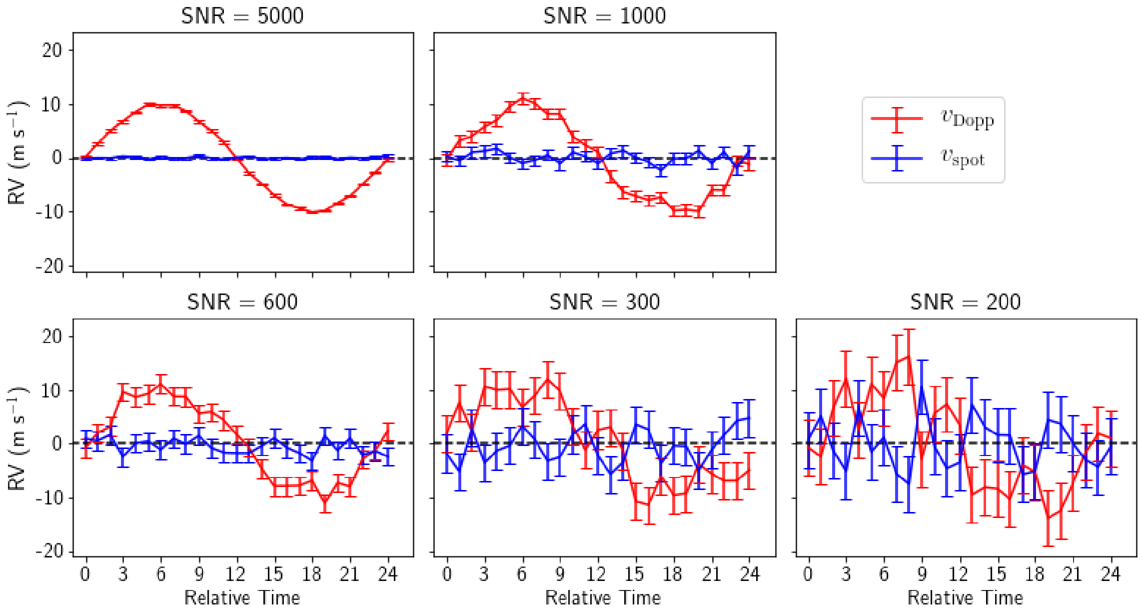

Figure 4.5: The estimated coefficients in Equation (4.7) and their uncertainties over time for a true exoplanet-induced RV signal with semi-amplitude 10 m s^{-1}. Each panel represents a different SNR indicated in the title. The uncertainty for each coefficient value is indicated with vertical error bars.

Both Figures 4.5 and 4.6 demonstrate that when the SNR of the spectra decreases below 300 distinguishing what proportion of the RV signal is due to a Doppler shift vs. a star spot becomes rather difficult. Since most modern exoplanet surveys have a SNR in the $200 - 300$ range, this likely means that the model would not accurately disentangle the signals of exoplanets and star spots. Furthermore, both the Doppler signal used in Figure 4.5 and the spot signal in Figure 4.6 are rather large compared to that of Earth-like exoplanets and star spots on the Sun.

While this suggests that the model is lacking in ability to disentangle stellar activity and Doppler shifts, it also sheds some light on why this problem has persisted for many decades. We find that the angle between the vectors $\boldsymbol{X}_1$ and $\boldsymbol{X}_3$ is approximately $2.6°$, which indicates a strong collinearity between these two variables. Furthermore, this is a collinearity that is not just due to a poor modeling choice, but is instead set by nature itself. The overall reason for why this strong collinearity is present is the fact that the stellar activity

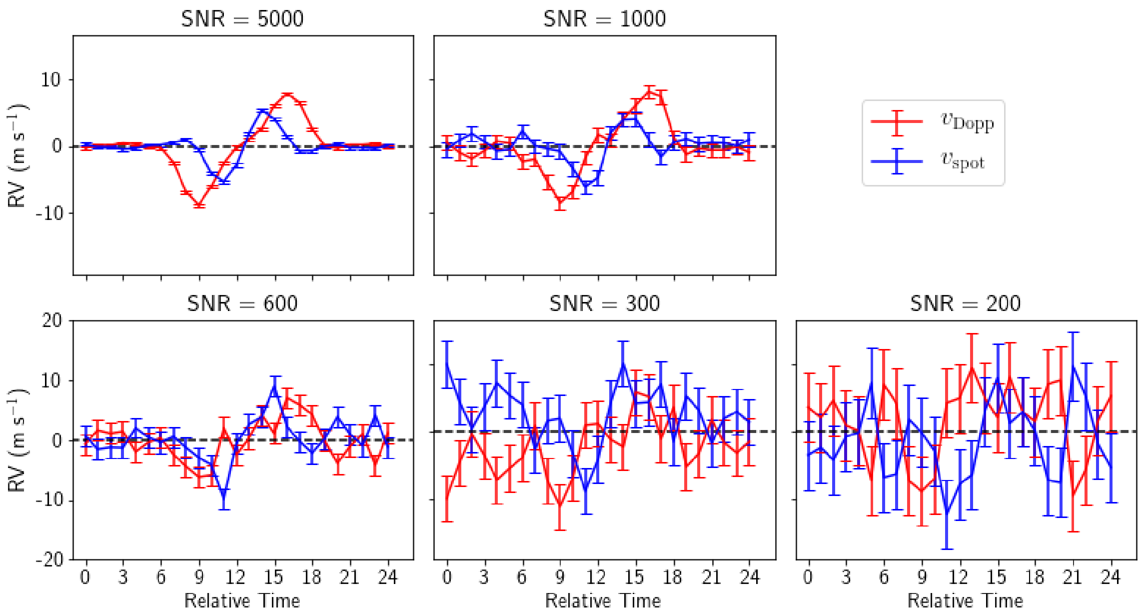

Figure 4.6: The estimated coefficients in Equation (4.7) and their uncertainties over time for a RV signal due to a 1% equatorial star spot. Each panel represents a different SNR indicated in the title. The uncertainty for each coefficient value is indicated with vertical error bars.

signal orthogonal to the Doppler signal (represented by $\boldsymbol{X}_2$) usually leads to a difference flux in the spectrum that is significantly smaller than that caused by a Doppler shift.

For future work, we suggest studying the realistic scenario where both a star spot and a Doppler shift are present in the data. Since we use linear models throughout this work, we suspect that this will produce similar results to what we find here, at least under the assumption that the combined effect of a star spot and a Doppler shift is the superposition of the two.

4.3 Conclusion

We conclude that at a single instance in time the signals of a Doppler shift and a star spot in the stellar spectrum are strongly collinear and that below a realistic SNR of 300 the two are very difficult to disentangle. Therefore, disentangling stellar activity from Doppler shifts likely requires one to utilize the behavior of the two astrophysical effects over time.

Chapter 5

A Single-Step Implementation of the Radial Velocity Method

5.1 Introduction

The first method successfully used to find extra-solar planets (hereafter referred to as exoplanets) around Sun-like stars was the radial velocity (RV) method (Mayor and Queloz, 1995). This method is traditionally applied in two sequential steps: (i) estimate the target star's RV from the stellar spectrum collected at each time of observation, and (ii) model the estimated RV's as a function of time with parameters that describe the oscillatory motion imposed on the target star by an orbiting exoplanet.

While the RV method has been fairly successful at discovering hundreds of exoplanets (Han et al., 2014), it is well known that it faces a number of limitations in discovering Earth-like exoplanets (Fischer et al., 2016). One reason these limitations exist is because the collected spectrum of a star contains many signals, such as light absorbed by the Earth's atmosphere (often referred to as tellurics) (Cunha et al., 2014; Halverson et al., 2016) and stellar activity in the target star's atmosphere (Saar and Donahue, 1997; Queloz et al., 2001; Desort et al., 2007; Meunier et al., 2010), that can distort the estimated RV. While great efforts have been made to correct for the effect these signals impose on the estimated RV, they have not yet reached the level required for discovering Earth-like exoplanets.

One potential improvement for applying such corrections lies in the nature of the RV method traditionally consisting of the two-step sequence mentioned above. While there are a number of different approaches for the step of estimating the RV from each spectrum, they can all be viewed as a dimensional reduction of the data. One set of approaches estimates the RV directly from the stellar spectrum (Bouchy et al., 2001; Anglada-Escudé and Butler, 2012; Astudillo-Defru et al., 2015; Holzer et al., 2021a), which is essentially reducing approximately 10^5 pixel measurements to a single number. Other approaches, which tend to be more popular, calculate a cross-correlation function from the spectrum and estimate the RV from it. This can also be viewed as a dimensional reduction from thousands of spectral absorption features to one. While great efforts have been made to correct for non-exoplanet effects using this dimensionally-reduced data, there is likely some crucial information that is lost in the dimensional-reduction as these effects are known to affect separate portions of the spectrum differently (Dumusque, 2018; Cretignier et al., 2020).

Furthermore, the nature of the RV method's two-step procedure requires not only estimating the RV in the first step, but also obtaining an accurate estimate of its uncertainty. While this is straight-forward with some approaches that use least-squares (Holzer et al., 2021a), other approaches require more assumptions that may not necessarily be true such as the validity of error propagation.

Here we demonstrate that it is not necessary for the RV method to be split into two sequential steps. Instead, one can estimate the exoplanet orbital parameters directly from the time series of stellar spectra without needing to explicitly calculate the RV at each time. This avoids the issue of needing to accurately estimate the RV standard error, and also allows for using all the spectral information to correct for unwanted effects.

In Section 5.2 we introduce the methodology that combines both traditional steps of the RV method into one. The new approach is then analyzed through simulation studies in Section 5.3 and on recently collected data from EXPRES (Jurgenson et al., 2016; Petersburg et al., 2020) for three stars with known planetary companions in Section 5.4. We then provide a brief discussion of the methods implications and potential improvements in Section 5.5 and conclude in Section 5.6.

5.2 Methods

In the RV method, a target star is typically observed at known times $T_1, T_2, ..., T_{\mathcal{T}}$. At each observation time T_t the spectrograph collects a realization of the stellar spectrum which, after correcting for the Earth's motion (Wright and Eastman, 2014; Blackman et al., 2017, 2020) and various instrumental effects such as the theoretical blaze function (Barker, 1984; Xu et al., 2019), has the form of $\{(\tilde{X}_{i,t}, \tilde{Y}_{i,t}, \varrho_{i,t})\}_{i=1}^{N}$ where $\tilde{X}$ is the wavelength measurement, $\tilde{Y}$ is the normalized flux, ϱ is the standard deviation of the normalized flux, and i indexes the pixels in the spectrograph. The full data set then takes the form of $\left\{\left(T_t, \{(\tilde{X}_{i,t}, \tilde{Y}_{i,t}, \varrho_{i,t})\}_{i=1}^{N}\right)\right\}_{t=1}^{\mathcal{T}}$. In words, this is a data set of $\mathcal{T}$ known observation times and, at every time, N measurements of wavelength, normalized flux, and normalized flux standard deviation.

5.2.1 Likelihood Specification

Instead of modeling the normalized flux $\tilde{Y}_{i,t}$ we prefer to use the difference flux $Y_{i,t} = \tilde{Y}_{i,t} - \tau_i$ where τ is the template flux which represents the normalized flux with no noise, Doppler shift, or other time-dependent astrophysical effects. While such a template spectrum is not truly accessible, it can be accurately estimated from a set of observed spectra (Holzer et al., 2021a).

Holzer et al. (2021a) showed that at observation time t_m, under reasonable assumptions, the effect of a small Doppler shift due to a RV v_t on the difference flux of a stellar spectrum can be written as

$$Y_{i,t} = v_t X_{i,t} + \varepsilon_{i,t} \quad \text{where} \;\; \varepsilon_{i,t} \sim \text{iid N}\left(0, \varrho_{i,t}^2\right) \;\; \text{for} \;\; i = 1, 2, ..., N \tag{5.1}$$

where $X_{i,t} = \sum_{j=1}^{n} \frac{\sqrt{\sqrt{\pi}} d_j \mu_j}{c\sqrt{2\sigma_j}} \psi_1 \left(\tilde{X}_{i,t}; \mu_j, \sigma_j\right)$ is a transformation of the wavelength, c is the speed of light, and n, d_j, μ_j and σ_j are parameters of the star that do not change over time and are well-estimated from the derived template spectrum.

It is well understood that the RV of a host star due to an orbiting exoplanet behaves over time as

$$v_t = K(\cos(\omega + \nu_t(T_t, P, e, M_0)) + e\cos(\omega)) + C \tag{5.2}$$

where K is the RV semiamplitude, ω is the argument of periastron, C is the RV offset, and ν is the true anomaly which changes over time depending on the orbital period P, the orbital eccentricity e, and the mean anomaly M_0 of the exoplanet at time $T = 0$. In Equation (5.2), ν_t is the solution to the following three equations:

$$M_t = \frac{2\pi T_t}{P} - M_0 \tag{5.3}$$

$$M_t = E_t - e \cdot \sin(E_t) \tag{5.4}$$

$$\tan\left(\frac{\nu_t}{2}\right) = \sqrt{\frac{1+e}{1-e}} \tan\left(\frac{E_t}{2}\right). \tag{5.5}$$

In the special case of $e = 0$ (i.e., a circular exoplanet orbit), we have from Equations (5.3) - (5.5) that $\nu_t = E_t = M_t$ and therefore ν_t is linearly related to the reciprocal of P for every T_t. However, when e is not equal to 0, Equation (5.4) becomes transcendental and ν_t must be approximately solved for numerically. This is traditionally done using Newton's algorithm, initializing E_t to be equal to M_t and updating E_t with the update step

$$E_{t,new} = E_{t,old} - \frac{E_{t,old} - e \cdot \sin(E_{t,old}) - M_t}{1 - e \cdot \cos(E_{t,old})}. \tag{5.6}$$

We find that in the worst case scenario where e is nearly equal to 1.0, convergence is reached for any M_t after about 7 repetitions of the update step in Equation (5.6)[1]. Therefore, we approximately solve for E_t by defining

$$g(\xi) = \xi - \frac{\xi - e \cdot \sin(\xi) - M_t}{1 - e \cdot \cos(\xi)} \tag{5.7}$$

and setting

$$E_t = g^{(7)}(M_t) \tag{5.8}$$

where $g^{(k)}$ notates the function g composed with itself k times.

This then allows us to approximately write ν_t in closed form as

$$\nu_t(T_t, P, e, M_0)) \approx 2\tan^{-1}\left(\sqrt{\frac{1+e}{1-e}}\tan\left(\frac{g^{(7)}(\frac{2\pi T_t}{P} - M_0)}{2}\right)\right) \tag{5.9}$$

by combining Equations (5.3), (5.5), and (5.8).

So by substituting Equation (5.2) into Equation (5.1) we have that the likelihood function of the exoplanet parameters of interest $(K, P, e, \omega, M_0, C)$ is

---

[1] With e set to 0.97 we take a set of 630 values of M_t equally spaced by 0.01 between 0 and π. For each of these values of M_t we initialize E_t at M_t and update E_t fifteen times according to Equation (5.6). We find that the maximum absolute difference between the seventh and fifteenth updates is approximately 3.2×10^{-10}. Approximately, 95% of the absolute differences were less than 3.3×10^{-17}.

$$L(K, P, e, \omega, M_0, C) = \prod_{t=1}^{\mathcal{T}} \prod_{i=1}^{N} \left(2\pi \varrho_{i,t}^2\right)^{-1/2} \cdot$$
$$\exp\left(-\frac{1}{2}\left(\frac{Y_{i,t} - \left(K(\cos(\omega + \nu_t(T_t, P, e, M_0)) + e\cos(\omega)) + C\right) X_{i,t}}{\varrho_{i,t}}\right)^2\right) \quad (5.10)$$

with ν_t as in Equation (5.9).

5.2.2 Likelihood Maximization

While we ultimately intend to apply statistical inference on the exoplanet parameters $(K, P, e, \omega, M_0, C)$ through Markov Chain Monte Carlo (MCMC) sampling from a posterior distribution, we find that the Markov chain rarely converges in a reasonable amount of steps with naive initialization. Therefore, we begin by calculating the maximum likelihood estimator (MLE) of $(K, P, e, \omega, M_0, C)$. While calculating the MLE has long been included in the two-step process of the RV method (Ford, 2005), it is implemented rather differently in our single-step process.

Nevertheless, there are some similarities that our approach has with the traditional two-step approach. Similar to Ford (2005) and Ford (2006), we reparameterize before optimizing. Instead of maximizing the likelihood in $(K, P, e, \omega, M_0, C)$, we instead optimize with the reparameterization

$$\theta_0 = \log(K), \quad \theta_1 = \log(P), \quad \theta_2 = \sqrt{e}\sin(\omega), \quad (5.11)$$
$$\theta_3 = \sqrt{e}\cos(\omega), \quad \theta_4 = M_0, \quad \theta_5 = C$$

which can be inverted as

$$K = \exp(\theta_0), \quad P = \exp(\theta_1) \quad e = \theta_2^2 + \theta_3^2, \tag{5.12}$$
$$\omega = \tan^{-1}\left(\frac{\theta_2}{\theta_3}\right) - \pi \cdot \mathbb{1}\{\theta_3 < 0\}, \quad M_0 = \theta_4, \quad C = \theta_5$$

For every set of values of θ_1, $-1 < \theta_2 < 1$, $-1 < \theta_3 < 1$, and θ_4 it is straightforward to show that the likelihood in Equation (5.10) has a unique global maximum with no other local maxima in both K and C (and therefore the same is true for θ_0 and θ_5). However, the same is not true for the other four parameters, which is particularly true for θ_1 representing the orbital period P.

The traditional two-step approach first optimizes P by using RV estimates at each observation time $\{(T_t, \hat{v}_t)\}_{t=1}^{\mathcal{T}}$ in the Lomb-Scargle periodogram (Scargle, 1982). The period with the highest power is then taken as an initial estimate of P. Then, the Levenberg-Marquardt algorithm (Moré, 1978) is used to further optimize all parameters, initializing P at its initial estimate.

In our single-step approach, however, we do not use a periodogram as its use is not straightforward without first getting RV estimates for each observation. Instead, we proceed directly to local optimization of all parameters, taking advantage of modern computing by parallelizing across different initializations in a grid-search manner. We find that initializing at $\theta_0 = 0$, $\theta_5 = 0$, and every combination of $\theta_1 \in \{\theta_{1,\min}, \theta_{1,\min} + 0.07, \theta_{1,\min} + 0.14, ..., \theta_{1,\max} - 0.07, \theta_{1,\max}\}$, $\theta_2 \in \left\{-\frac{1}{2}, 0, \frac{1}{2}\right\}$, $\theta_3 \in \left\{-\frac{1}{2}, 0, \frac{1}{2}\right\}$, $\theta_5 \in \left\{-\pi, -\frac{3\pi}{4}, -\frac{\pi}{2}, ..., \frac{\pi}{2}, \frac{3\pi}{4}\right\}$ almost always results in finding the MLE. In the instance when it does not find the MLE (a situation that we comment on later in Section 5.2.3), increasing the refinement of the grid for either θ_1 or θ_4 may be necessary.

Upon calculating the MLE, we intend to take account of the additional information provided by the risk landscape about the MLE before proceeding to posterior sampling. Not only does the value of the log-likelihood inform us about an optimal estimator $\hat{\theta}$, but the second derivative of the log-likelihood landscape about $\hat{\theta}$ provides an estimate of its covariance. Formally, we estimate the covariance matrix, Σ, using an estimate of the Fisher Information matrix, $\mathcal{I}$ as

$$\hat{\Sigma} = \hat{\mathcal{I}}^{-1}(\hat{\theta}) \quad \text{where} \quad \hat{\mathcal{I}}_{i,j} = -\frac{\partial^2}{\partial \theta_i \partial \theta_j} \log L(\theta)|_{\hat{\theta}} \tag{5.13}$$

where L is the likelihood given in Equation (5.10) (or a reparameterized version of it). Since the second derivatives in Equation (5.13) can be rather tedious to calculate, we again take use of the power of modern computing through automatic differentiation (Wengert, 1964; Rall, 1986).[2]

5.2.3 Posterior Sampling

While one could choose to apply statistical inference on the exoplanet parameters using just the MLE $\hat{\theta}$ and estimated covariance matrix $\hat{\Sigma}$, we prefer to do inference through sampling of a posterior distribution. One reason for this is because Ford (2006) notes that the posteriors often depart significantly from normality.

While we calculate the MLE with the reparameterization of Equation (5.11), we find that the Markov Chain Monte Carlo (MCMC) works better when sampling in $(\log(K), \log(P), e, \omega, M_0, C)$ rather than θ. We find that this is particularly true for exoplanets with a low eccentricity.

Before proceeding with MCMC sampling, we specify a prior distribution on each parameter based on data of presently confirmed exoplanets. Using data from the NASA Exoplanet Archive (Akeson et al., 2013) obtained in January, 2021 we found that there were 477 confirmed exoplanets with parameter values $(K_{\text{conf}}, P_{\text{conf}}, e_{\text{conf}}, \omega_{\text{conf}}, M_{0,\text{conf}}, C_{\text{conf}})$. To allow for the likely scenario of certain exoplanets remaining undiscovered, such as those that are Earth-like, we use priors that are wider than the range of currently confirmed exoplanets.

---

[2] Even though an estimate of the covariance matrix is returned by the function used for optimization (`scipy.optimize.minimize` in Python), we find that this is significantly different and not as accurate as the estimate we obtain by calculating the Fisher Information matrix ourselves and inverting it.

For the sampling parameter $\log(K)$ we use the Normal distribution with mean $\overline{\log(K_{\text{conf}})}$ and variance $1.5 \times s^2_{\log(K_{\text{conf}})}$ where $\overline{\log(K_{\text{conf}})}$ denotes the average of the 477 confirmed exoplanet values of $\log(K)$ and $s^2_{\log(K_{\text{conf}})}$ denotes their sample variance. Using this same denotation, we put a $\text{N}\left(\overline{\log(P_{\text{conf}})}, 1.5 \times s^2_{\log(P_{\text{conf}})}\right)$ prior on $\log(P)$, a $\text{N}(\overline{e_{\text{conf}}}, 2 \times s^2_{e_{\text{conf}}})$ prior on e truncated between 0 and 1, and a $\text{Unif}(0, 2\pi)$ prior on both ω and M_0. These priors are shown, together with a comparison to the distribution of confirmed parameter values, in Figure 5.1.

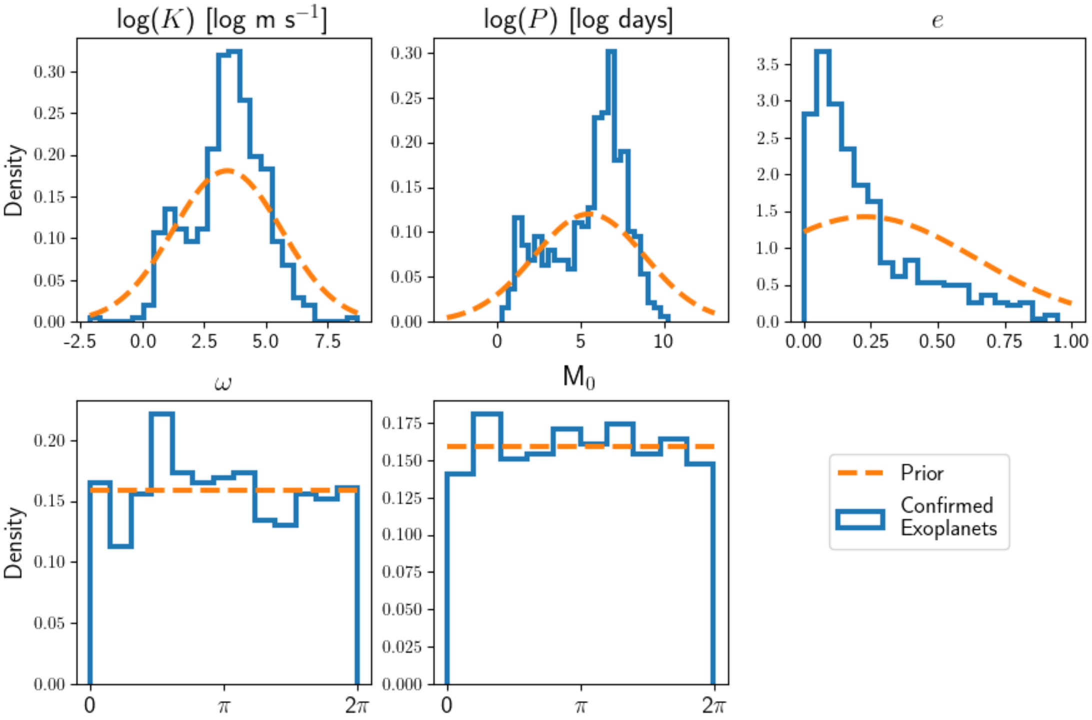

Figure 5.1: Visualization of the prior distributions put on the sampling parameters $\log(K), \log(P), e, \omega$, and M_0. These are shown in the dashed line of each panel. For comparison, a normalized histogram of these same parameters for presently confirmed exoplanets (according to the NASA Exoplanet Archive in January, 2021) are also shown in solid lines.

For C we use a $\text{N}(0, 10^2)$ prior distribution. An assumption built into the use of this prior is that the difference flux Y is calculated from a template spectrum that is approximately at the offset RV of the observed star. If the template spectrum is estimated with local nonparametric regression using all the observed spectra as in Holzer et al. (2021a), then this is typically true. Were this assumption not to be met by having a template spectrum that did not account for the offset RV of the star, assumptions underlying results in Holzer et al. (2021a) as shown in Equation (5.1) would also be invalid. Therefore, we recommend using a template estimation method that is at least similar to the approach of Holzer et al. (2021a).

We use the product of all six individual prior densities as the full prior density $P\log(K)$, $\log(P), e, \omega, M_0, C$. Then the posterior distribution can be written, up to a proportionality constant, as

$$P\left(\log(K), \log(P), e, \omega, M_0, C \;\middle|\; \left\{\left(T_t, \{(\tilde{X}_{i,t}, \tilde{Y}_{i,t}, \varrho_{i,t})\}_{i=1}^{N}\right)\right\}_{t=1}^{\mathcal{T}}\right) \propto \\ L(\log(K), \log(P), e, \omega, M_0, C) \times P\left(\log(K), \log(P), e, \omega, M_0, C\right) \quad (5.14)$$

where $L(\log(K), \log(P), e, \omega, M_0, C)$ is (a reparameterized version of) the likelihood shown in Equation (5.10).

To sample from the posterior of Equation (5.14), we use the Metropolis MCMC algorithm (Metropolis et al., 1953). We initialize the Markov chain at the MLE previously calculated. Then we use the multivariate Normal distribution with covariance matrix $\hat{\Sigma}$ as the proposal distribution[3]. This allows for taking account of strong correlations that may, and often do, exist between the sampling parameters.

We find that there is essentially no "burn-in" region of the Markov chain that needs to be eliminated before using the sampling for inference. Instead, the chain reaches convergence from the start almost always. (More details on this are provided in Section 5.3.2 below.) In the rare instances when the chain does not have immediate convergence, it is usually because the optimization algorithm described in Section 5.2.2 failed to find the MLE. In this case,

---

[3] To help improve the acceptance rate of the MCMC we actually use $\hat{\Sigma}/4$ as the covariance matrix of the Normal distribution used for proposing new values.

we recommend increasing the grid used to optimize θ_1 and θ_4 which we find usually fixes the issue.

5.3 Simulation Studies

As our proposed gridsearch optimization is perhaps the most unique element of our single-step implementation of the RV method, we use simulation to compare it to the traditional use of a periodogram in the two-step approach. We then proceed to a set of simulations designed to both assess the convergence of our MCMC and compare its results to the traditional two-step procedure of the RV method.

5.3.1 Periodogram vs. Gridsearch Optimization

Both the traditional two-step approach and our proposed single-step approach to the RV method ultimately use posterior sampling to infer the values of the exoplanet parameters. However, naive initialization of the Markov chain used for sampling rarely leads to convergence in a reasonable amount of time. Therefore, both approaches begin by attempting to calculate the MLE which is then used for improved initialization. Perhaps in the two-step approach the most common implementation of this optimization is to first obtain RV estimates for each observed spectrum, subsequently use these estimates in a periodogram to get an initial estimate of the orbital period P, and then optimize all parameters using this initial estimate of P. The use of the periodogram typically is motivated by P being among the most difficult to optimize, while failing to do so almost certainly prevents the finding of optimal values for most other parameters. However, since our approach does not explicitly calculate an RV estimate at each observation time, the use of periodograms becomes non-trivial. Instead, we use a gridsearch approach to optimize P and all other parameters simultaneously.

While it may seem like our optimization is at a disadvantage by not involving periodograms, this is not necessarily the case. Although a gridsearch optimization is more computationally expensive, we demonstrate here that in fact it works at least as good as the approach involving periodograms at finding the MLE. For low-eccentricity orbits, both methods almost always find the MLE. But for high-eccentricity orbits, we demonstrate that our method outperforms the periodogram-based optimization.

With true values of $K^* = 1$ m s^{-1}, $P^* = 3$ days, $e^* = 0.8$, $\omega^* = \frac{\pi}{8}$, $M_0^* = 0$, and $C^* = -4$ m s^{-1} we randomly sampled 50 observation times uniformly between 0 and 50 days, calculating the respective RV at each time with Equation (5.2). Then at each time we take a smooth template spectrum for the star HD 217014 and Doppler shift it by the appropriate Doppler factor ξ calculated from the RV as $\xi_t = 1 + v_t/c$ where c is the speed of light. Finally, we add Poisson-like noise to each spectrum at a SNR of 250. This final step of adding noise realizations to the 50 shifted spectra is then repeated 105 independent times.

Using the traditional approach, for each of the 105 simulations we estimate the RV at each time using the HGRV methodology (Holzer et al., 2021a), afterwards using the Lomb-Scargle periodogram (Scargle, 1982) to get an initial estimate $\hat{P}_{\text{periodogram}}$ of the period. Then we use the gridsearch optimization approach to get the different estimator $\hat{P}_{\text{gridsearch}}$. Table 5.1 compares the two optimizations' ability to recover the true orbital period $P^* = 3$ days.

		$\lvert \hat{P}_{\text{gridsearch}} - P^* \rvert < 0.1$ days	
		True	**False**
$\lvert \hat{P}_{\text{periodogram}} - P^* \rvert < 0.1$ days	**True**	36	6
	False	26	37

Table 5.1: Summary of the results for the simulation study comparing the gridsearch optimization to the periodogram optimization. All 105 simulations involved the same observation times and true orbital parameters. The only difference between each was the noise realizations. The count of simulations where the gridsearch optimization recovered the true orbital period is shown according to the horizontal axis. And the vertical axis represents the count of cases where the periodogram approach recovered the orbital period.

Table 5.1 demonstrates that the gridsearch optimization can significantly outperform the periodogram-based approach in this high-eccentricity setting. This is, at least partially, because maximizing the Lomb-Scargle periodogram power is equivalent to fitting a sine curve to the data with least-squares loss (VanderPlas, 2018). And since high-eccentricity orbits have a very non-sinusoidal shape, it makes sense that the periodogram would have a more difficult time estimating the periodicity. The gridsearch optimization avoids this issue by allowing e and ω (the eccentricity-relevant parameters) to be optimized simultaneously with the period.

5.3.2 MCMC Convergence

We now intend to study the effectiveness of the MCMC sampling. For this we use the same setup as in Section 5.3.1, sampling 50 observation times uniformly between 0 and 50 days. Each set of true exoplanet parameters is then used to calculate the true RV at each time, which we then use to Doppler-shift a template spectrum for 51 Pegasi. Finally, Poisson-like noise is added to each spectrum at a SNR of 250. The optimization and sampling procedures described in Section 5.2 are then employed to obtain credible intervals (CI) for each exoplanet parameter.

For each simulation, we run the Markov chain for a total of 10^5 steps. To assess the convergence of the Markov chain used for posterior sampling, we use the Gelman-Rubin (GR) statistic (Gelman et al., 1992; Brooks and Gelman, 1998). The GR statistic takes in multiple chains and compares the between-chain variance to the within-chain variance. If the chains have all converged to the stationary distribution then the GR should generally be 1.1 or less. We calculate the GR statistic by first splitting the full chain of 10^5 steps into sub-chains of five thousand steps. Every other five thousand length sub-chain, beginning with the second, is then used to calculate the GR. Since the GR needs to be calculated for each of the six parameters, we take the maximum of the six to be used to assess convergence.

Using a simulation with $K^* = 1$ m s^{-1}, $P^* = 3$ days, $e^* = 0.1$, $\omega^* = 2\pi/3$ radians, M_0^* randomly drawn between 0 and 2π, and $C^* = -10$ m s^{-1}, we get the results shown in Figure 5.2.

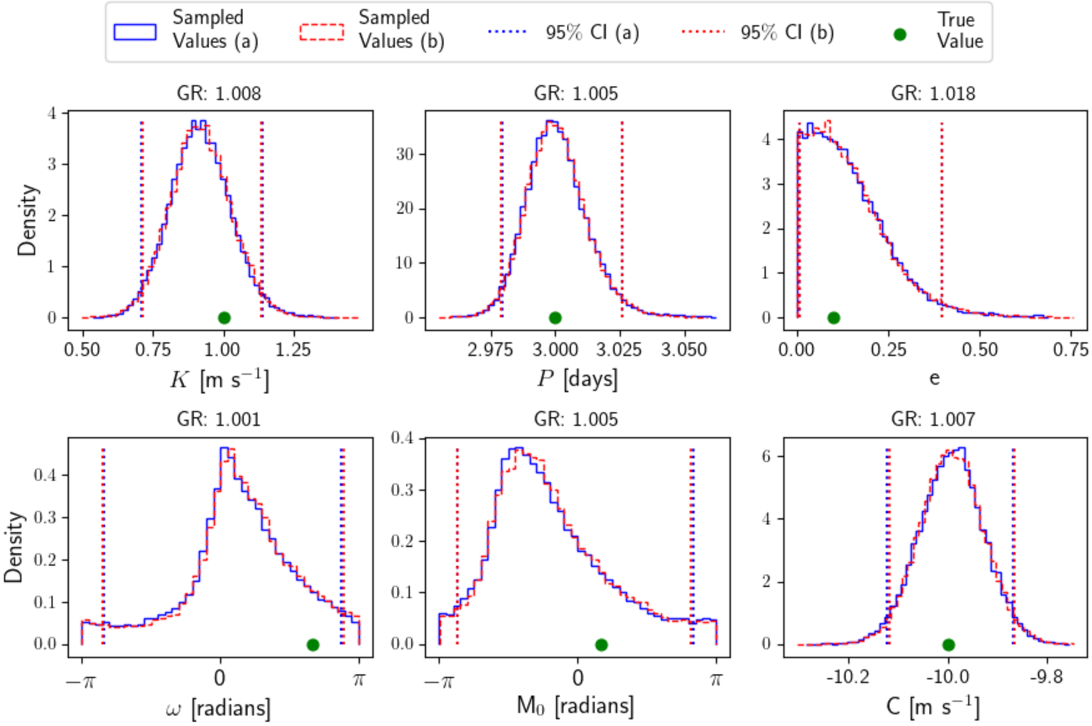

Figure 5.2: Posterior samplings from a simulation with $K^* = 1$ m s^{-1}, $P^* = 3$ days, $e^* = 0.1$, $\omega^* = 2\pi/3$, M_0^* randomly drawn between 0 and 2π, and $C^* = -10$ m s^{-1}all indicated by solid dots. Histograms and 95% CI's for our proposed single-step approach are indicated in the key with the letter (a). The letter (b) indicates the traditional two-step approach. The GR statistic from the single-step approach for each parameter is shown on top of the corresponding panel. No samplings near the beginning of the Markov chain are excluded.

The results shown in Figure 5.2 confirm that the posterior distribution often departs significantly from normality. Since all GR statistics are well below 1.1 it also appears that, even without eliminating any potential "burn-in region" at the beginning of the chain, convergence to the posterior has been reached. Figure 5.2 also illustrates that when e^* is low and the exoplanet's orbit is nearly circular, almost any value of ω and M_0 are credible as these are eccentricity-specific parameters.

For comparison, the results for a simulation with $K^* = 1 \text{ m s}^{-1}$, $P^* = 20$ days, $e^* = 0.7$, $\omega^* = -2\pi/3$, M_0^* randomly drawn between 0 and 2π, and $C^* = -10 \text{ m s}^{-1}$are shown in Figure 5.3.

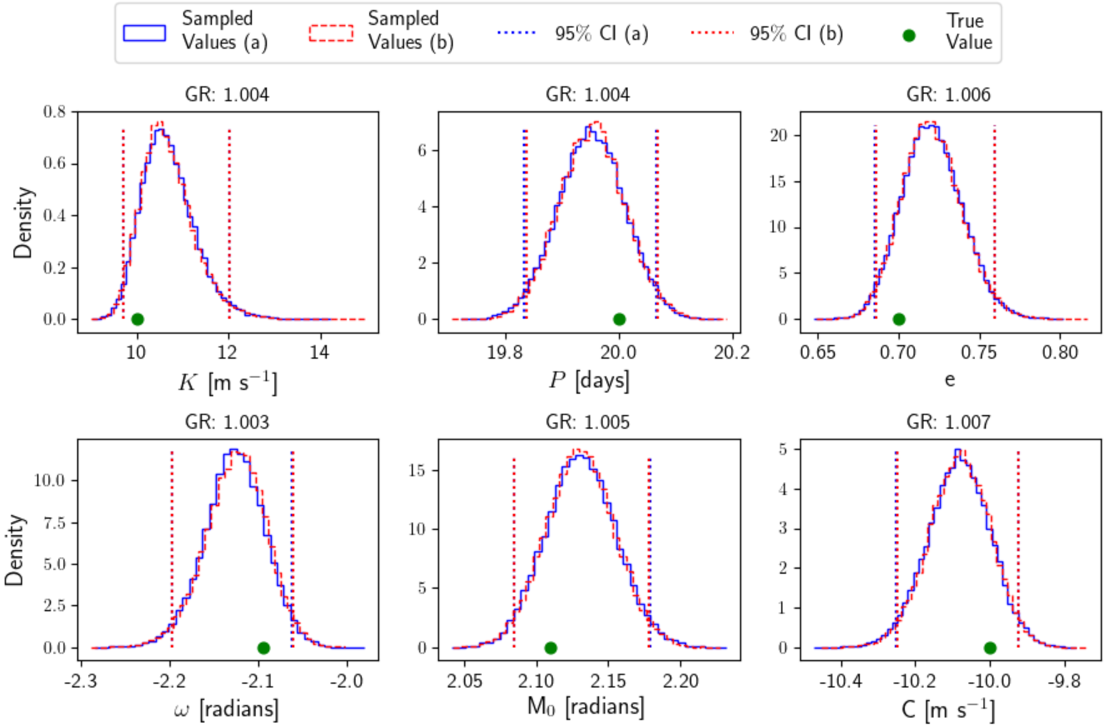

Figure 5.3: Posterior samplings from a simulation with $K^* = 10 \text{ m s}^{-1}$, $P^* = 20$ days, $e^* = 0.7$, $\omega^* = -2\pi/3$, M_0^* randomly drawn between 0 and 2π, and $C^* = -10 \text{ m s}^{-1}$all indicated by solid dots. Histograms and 95% CI's for our proposed single-step approach are indicated in the key with the letter (a). The letter (b) indicates the traditional two-step approach. The GR statistic from the single-step approach for each parameter is shown on top of the corresponding panel. No samplings near the beginning of the Markov chain are excluded.

To demonstrate the ability of our method to adapt to different exoplanet orbits, we extend the simulation study to include every combination of $K^* \in \{1\ m\ s^{-1}, 10\ m\ s^{-1}\}$, $P^* \in \{3 \text{ days}, 20 \text{ days}\}$, $e^* \in \{0.01, 0.1, 0.7\}$, and $\omega^* \in \{-\frac{2\pi}{3}, 0, \frac{2\pi}{3}\}$ with M_0^* chosen uniformly between 0 and 2π each time and $C^* = -10 \text{ m s}^{-1}$. The results from this extension are shown in Table 5.2.

P^***,** K^***,** e^***,** ω^*	$P,\ K,\ e,\ \omega$ 95% **CI (a)**	P, K, e, ω 95% **CI (b)**	**max. GR**
3	$(2.969,\ 3.006)$	$(2.970,\ 3.006)^+$	1.008
1	$(0.743,\ 1.126)^+$	$(0.753,\ 1.122)$	
0.01	$(0.003,\ 0.241)^+$	$(0.003,\ 0.233)$	
0	$(-3.001,\ 3.002)^+$	$(-2.989,\ 2.994)$	
3	$(2.979,\ 3.019)^+$	$(2.979,\ 3.018)$	1.011
1	$(0.766,\ 1.139)^+$	$(0.771,\ 1.141)$	
0.01	$(0.004,\ 0.255)^+$	$(0.004,\ 0.252)$	
$2\pi/3$	$(-2.854,\ 2.884)^+$	$(-2.841,\ 2.867)$	
3	$(2.979,\ 3.015)^+$	$(2.980,\ 3.015)$	1.010
1	$(0.939,\ 1.333)^+$	$(0.937,\ 1.325)$	
0.01	$(0.007,\ 0.292)^+$	$(0.006,\ 0.288)$	
$-2\pi/3$	$(0.626,\ 5.395)$	$(0.581,\ 5.543)^+$	
3	$(2.998,\ 3.002)$	$(2.998,\ 3.002)^+$	1.010
10	$(9.831,\ 10.179)^+$	$(9.833,\ 10.178)$	
0.01	$(0.002,\ 0.041)^+$	$(0.003,\ 0.040)$	
0	$(-0.475,\ 1.985)^+$	$(-0.289,\ 1.854)$	
3	$(2.998,\ 3.001)^+$	$(2.998,\ 3.001)$	1.012
10	$(9.861,\ 10.236)$	$(9.862,\ 10.239)^+$	
0.01	$(0.001,\ 0.028)$	$(0.001,\ 0.029)^+$	
$2\pi/3$	$(-0.771,\ 4.160)^+$	$(-0.800,\ 4.131)$	
3	$(2.998,\ 3.003)^+$	$(2.998,\ 3.003)$	1.012
10	$(9.858,\ 10.214)^+$	$(9.858,\ 10.211)$	
0.01	$(0.001,\ 0.032)$	$(0.001,\ 0.032)^+$	
$-2\pi/3$	$(2.012,\ 6.285)^+$	$(1.989,\ 6.246)$	

Continued on next page

Table 5.2 – continued from previous page

P^*, K^*, e^*, ω^*	$P,\ K,\ e,\ \omega$ 95% **CI (a)**	P, K, e, ω 95% **CI (b)**	**max. GR**
3	$(2.979,\ 3.014)^+$	$(2.979,\ 3.014)$	1.013
1	$(0.867,\ 1.202)$	$(0.867,\ 1.203)^+$	
0.1	$(0.004,\ 0.299)$	$(0.004,\ 0.303)^+$	
0	$(-4.392,\ 1.132)$	$(-4.399,\ 1.172)^+$	
3	$(2.979,\ 3.026)$	$(2.979,\ 3.026)^+$	1.018
1	$(0.711,\ 1.139)^+$	$(0.714,\ 1.134)$	
0.1	$(0.006,\ 0.397)^+$	$(0.006,\ 0.395)$	
$2\pi/3$	$(-2.647,\ 2.739)$	$(-2.657,\ 2.801)^+$	
3	$(2.973,\ 3.009)^+$	$(2.974,\ 3.009)$	1.029
1	$(0.821,\ 1.212)^+$	$(0.829,\ 1.209)$	
0.1	$(0.034,\ 0.464)^+$	$(0.034,\ 0.458)$	
$-2\pi/3$	$(-1.864,\ 0.098)^+$	$(-1.913,\ 0.033)$	
3	$(2.998,\ 3.002)^+$	$(2.998,\ 3.001)$	1.010
10	$(9.716,\ 10.059)$	$(9.718,\ 10.062)^+$	
0.1	$(0.097,\ 0.132)$	$(0.097,\ 0.132)^+$	
0	$(-0.385,\ -0.053)^+$	$(-0.389,\ -0.057)$	
3	$(2.997,\ 3.002)^+$	$(2.997,\ 3.002)$	1.010
10	$(9.754,\ 10.083)^+$	$(9.753,\ 10.081)$	
0.1	$(0.072,\ 0.109)^+$	$(0.073,\ 0.109)$	
$2\pi/3$	$(1.913,\ 2.340)^+$	$(1.924,\ 2.335)$	
3	$(2.999,\ 3.002)$	$(2.999,\ 3.002)^+$	1.009
10	$(9.792,\ 10.176)^+$	$(9.796,\ 10.172)$	
0.1	$(0.080,\ 0.118)^+$	$(0.080,\ 0.117)$	

Continued on next page

Table 5.2 – continued from previous page

P^*, K^*, e^*, ω^*	$P,\ K,\ e,\ \omega$ 95% **CI (a)**	P, K, e, ω 95% **CI (b)**	**max. GR**
$-2\pi/3$	$(-2.404,\ -2.043)$	$(-2.404,\ -2.039)^+$	
3	$(2.978,\ 3.059)^+$	$(2.977,\ 3.057)$	1.068
1	$(0.319,\ 1.235)$	$(0.308,\ 1.355)^+$	
0.7	$(0.188,\ 0.810)$	$(0.105,\ 0.826)^+$	
0	$(-1.286,\ 1.240)^+$	$(-0.987,\ 1.432)$	
3	$(2.974,\ 3.004)^+$	$(2.974,\ 3.004)$	1.008
1	$(0.668,\ 1.787)$	$(0.684,\ 2.427)^+$	
0.7	$(0.513,\ 0.903)$	$(0.527,\ 0.944)^+$	
$2\pi/3$	$(1.665,\ 2.748)^+$	$(1.598,\ 2.657)$	
3	$(2.990,\ 3.013)$	$(2.989,\ 3.016)^+$	1.016
1	$(0.861,\ 2.544)^+$	$(0.854,\ 2.036)$	
0.7	$(0.521,\ 0.877)^+$	$(0.512,\ 0.858)$	
$-2\pi/3$	$(-2.793,\ -1.824)^+$	$(-2.651,\ -1.793)$	
3	$(2.999,\ 3.001)^+$	$(2.999,\ 3.001)$	1.016
10	$(9.803,\ 10.462)^+$	$(9.802,\ 10.455)$	
0.7	$(0.688,\ 0.714)^+$	$(0.688,\ 0.713)$	
0	$(-0.055,\ 0.023)^+$	$(-0.054,\ 0.023)$	
3	$(2.999,\ 3.001)^+$	$(2.999,\ 3.000)$	1.008
10	$(9.425,\ 10.114)^+$	$(9.416,\ 10.095)$	
0.7	$(0.669,\ 0.706)$	$(0.669,\ 0.706)^+$	
$2\pi/3$	$(2.058,\ 2.147)^+$	$(2.058,\ 2.147)$	
3	$(2.997,\ 3.001)^+$	$(2.997,\ 3.001)$	1.008
10	$(9.797,\ 10.304)^+$	$(9.790,\ 10.297)$	

Continued on next page

Table 5.2 – continued from previous page

P^*, K^*, e^*, ω^*	$P,\ K,\ e,\ \omega$ 95% **CI (a)**	P, K, e, ω 95% **CI (b)**	**max. GR**
0.7	$(0.676,\ 0.710)^+$	$(0.675,\ 0.709)$	
$-2\pi/3$	$(-2.158,\ -2.074)^+$	$(-2.157,\ -2.074)$	
20	$(20.000,\ 21.735)^+$	$(20.011,\ 21.732)$	1.010
1	$(0.791,\ 1.151)^+$	$(0.795,\ 1.151)$	
0.01	$(0.004,\ 0.248)^+$	$(0.003,\ 0.243)$	
0	$(-2.990,\ 2.977)$	$(-2.988,\ 2.966)^+$	
20	$(19.473,\ 21.257)$	$(19.442,\ 21.238)^+$	1.022
1	$(0.901,\ 1.265)^+$	$(0.904,\ 1.267)$	
0.01	$(0.006,\ 0.307)$	$(0.006,\ 0.309)^+$	
$2\pi/3$	$(-1.495,\ 3.473)^+$	$(-1.300,\ 3.384)$	
20	$(19.092,\ 20.678)^+$	$(19.133,\ 20.707)$	1.009
1	$(0.861,\ 1.223)^+$	$(0.869,\ 1.226)$	
0.01	$(0.004,\ 0.240)^+$	$(0.004,\ 0.238)$	
$-2\pi/3$	$(0.400,\ 5.814)^+$	$(0.429,\ 5.821)$	
20	$(19.936,\ 20.125)^+$	$(19.937,\ 20.124)$	1.012
10	$(9.894,\ 10.236)^+$	$(9.895,\ 10.232)$	
0.01	$(0.001,\ 0.032)^+$	$(0.001,\ 0.032)$	
0	$(-2.435,\ 2.486)^+$	$(-2.338,\ 2.357)$	
20	$(19.872,\ 20.037)^+$	$(19.874,\ 20.036)$	1.014
10	$(9.891,\ 10.242)$	$(9.887,\ 10.242)^+$	
0.01	$(0.000,\ 0.022)^+$	$(0.000,\ 0.022)$	
$2\pi/3$	$(-3.002,\ 2.990)^+$	$(-3.015,\ 2.972)$	
20	$(19.913,\ 20.080)^+$	$(19.917,\ 20.080)$	1.011

Continued on next page

Table 5.2 – continued from previous page

P^*, K^*, e^*, ω^*	$P,\ K,\ e,\ \omega$ 95% **CI (a)**	P, K, e, ω 95% **CI (b)**	**max. GR**
10	$(9.785,\ 10.151)$	$(9.781,\ 10.150)^{+}$	
0.01	$(0.000,\ 0.025)^{+}$	$(0.000,\ 0.025)$	
$-2\pi/3$	$(-3.012,\ 3.019)^{+}$	$(-3.010,\ 3.006)$	
20	$(18.767,\ 20.320)$	$(18.776,\ 20.336)^{+}$	1.010
1	$(0.828,\ 1.228)$	$(0.822,\ 1.229)^{+}$	
0.1	$(0.005,\ 0.276)^{+}$	$(0.005,\ 0.273)$	
0	$(-1.560,\ 3.647)^{+}$	$(-1.522,\ 3.632)$	
20	$(19.100,\ 20.591)^{+}$	$(19.118,\ 20.583)$	1.018
1	$(0.884,\ 1.244)$	$(0.879,\ 1.246)^{+}$	
0.1	$(0.021,\ 0.344)$	$(0.021,\ 0.345)^{+}$	
$2\pi/3$	$(1.250,\ 3.831)^{+}$	$(1.198,\ 3.771)$	
20	$(18.968,\ 21.044)^{+}$	$(18.976,\ 21.032)$	1.017
1	$(0.836,\ 1.192)^{+}$	$(0.834,\ 1.188)$	
0.1	$(0.009,\ 0.344)^{+}$	$(0.009,\ 0.338)$	
$-2\pi/3$	$(2.935,\ 7.150)$	$(2.860,\ 7.211)^{+}$	
20	$(19.961,\ 20.109)$	$(19.961,\ 20.109)^{+}$	1.007
10	$(9.867,\ 10.236)^{+}$	$(9.865,\ 10.228)$	
0.1	$(0.090,\ 0.123)$	$(0.090,\ 0.123)^{+}$	
0	$(-0.288,\ 0.089)^{+}$	$(-0.285,\ 0.090)$	
20	$(19.951,\ 20.128)$	$(19.952,\ 20.131)^{+}$	1.010
10	$(9.751,\ 10.076)$	$(9.753,\ 10.078)^{+}$	
0.1	$(0.085,\ 0.120)^{+}$	$(0.085,\ 0.119)$	
$2\pi/3$	$(1.854,\ 2.248)$	$(1.855,\ 2.248)^{+}$	

Continued on next page

Table 5.2 – continued from previous page

P^*, K^*, e^*, ω^*	$P,\ K,\ e,\ \omega$ 95% **CI (a)**	P, K, e, ω 95% **CI (b)**	**max. GR**
20	$(19.894,\ 20.063)^{+}$	$(19.893,\ 20.062)$	1.009
10	$(9.736,\ 10.083)^{+}$	$(9.736,\ 10.083)$	
0.1	$(0.085,\ 0.127)^{+}$	$(0.085,\ 0.126)$	
$-2\pi/3$	$(-2.282,\ -1.939)^{+}$	$(-2.279,\ -1.945)$	
20	$(19.405,\ 20.861)^{+}$	$(19.430,\ 20.870)$	1.024
1	$(0.722,\ 1.285)^{+}$	$(0.721,\ 1.246)$	
0.7	$(0.366,\ 0.690)^{+}$	$(0.369,\ 0.683)$	
0	$(-0.838,\ 0.188)$	$(-0.837,\ 0.199)^{+}$	
20	$(19.147,\ 21.036)^{+}$	$(19.206,\ 21.091)$	1.014
1	$(0.711,\ 1.533)$	$(0.684,\ 1.506)^{+}$	
0.7	$(0.359,\ 0.800)$	$(0.280,\ 0.800)^{+}$	
$2\pi/3$	$(1.771,\ 2.818)$	$(1.765,\ 2.851)^{+}$	
20	$(18.858,\ 21.727)^{+}$	$(18.923,\ 21.773)$	1.012
1	$(0.569,\ 1.610)^{+}$	$(0.566,\ 1.478)$	
0.7	$(0.325,\ 0.860)^{+}$	$(0.322,\ 0.850)$	
$-2\pi/3$	$(3.527,\ 4.693)^{+}$	$(3.537,\ 4.669)$	
20	$(19.952,\ 20.030)^{+}$	$(19.952,\ 20.030)$	1.010
10	$(9.704,\ 10.283)$	$(9.699,\ 10.294)^{+}$	
0.7	$(0.690,\ 0.715)^{+}$	$(0.691,\ 0.715)$	
0	$(-0.065,\ 0.023)^{+}$	$(-0.064,\ 0.022)$	
20	$(19.939,\ 20.061)$	$(19.938,\ 20.062)^{+}$	1.013
10	$(9.863,\ 10.519)$	$(9.866,\ 10.523)^{+}$	
0.7	$(0.682,\ 0.724)$	$(0.683,\ 0.725)^{+}$	

Continued on next page

Table 5.2 – continued from previous page

P^*, K^*, e^*, ω^*	$P,\ K,\ e,\ \omega$ 95% **CI (a)**	P, K, e, ω 95% **CI (b)**	**max. GR**
$2\pi/3$	$(2.053,\ 2.132)^+$	$(2.055,\ 2.131)$	
20	$(19.833,\ 20.066)^+$	$(19.837,\ 20.067)$	1.007
10	$(9.695,\ 12.027)^+$	$(9.685,\ 11.999)$	
0.7	$(0.686,\ 0.759)$	$(0.685,\ 0.759)^+$	
$-2\pi/3$	$(-2.198,\ -2.062)^+$	$(-2.196,\ -2.062)$	

Table 5.2: Results of applying the single step RV method to simulated data. The true values of P, K (in units of m s^{-1}), e, and ω for each simulation are given in the first column. The resulting 95% CI for each of these four parameters is provided in columns 2 and 3 for our single-step method (indicated by the letter "a") and the traditional two-step method (indicated by the letter "b") respectively. For all simulations M_0^* is randomly chosen uniformly in the interval $(-\pi, \pi)$ and $C^* = -10$ m s^{-1}. The maximum of the six GR statistics for our single-step method in each simulation is given in the last column. The CI's that do not cover the true value of the parameter are highlighted in red. For each simulation and parameter, the $+$ symbol indicates the CI that is wider: either the one from our single-step method or the one from the two-step method.

Table 5.2 also compares the output of our combined approach to that of the two-step approach. For the traditional two-step approach we estimate the RV's and their uncertainties with the methodology of Holzer et al. (2021a). Then we use the implementation of Fulton et al. (2018) to get 95% credible intervals for the final exoplanet parameters.[4]

Since the maximum GR in each case shown in Table 5.2 is well below 1.1 we again conclude that the Markov chain has converged to the posterior. Support for this is also provided by the fact that the large majority of 95% CI's cover the true parameter values, but occasionally don't. Furthermore, we find the CI's to be very similar between the two-step approach and our single-step approach.

---

[4] The approach in Fulton et al. (2018) for inferring the values of the exoplanet parameters from a set of RV estimates requires an initial good estimate of each parameter. We use the MLE as given by the gridsearch optimization described in Section 5.2.2 as this initialization. We also use the same priors for each parameter as given in Section 5.3.2.

For the large majority of simulations used to produce Table 5.2 we find that the estimated covariance matrix almost always gives some moderate to strong correlations between the exoplanet parameters. Often times θ_4 is strongly correlated with either $\theta_1,\ \theta_2$, or θ_3, which most frequently happens at low-eccentricity orbits.

5.4 Application to EXPRES

To test our proposed single-step methodology to real data, we use recently collected spectra from EXPRES (Jurgenson et al., 2016; Petersburg et al., 2020). We use the barcentric corrected wavelengths, normalized flux and its uncertainty, and the telluric model provided by EXPRES for each spectrum. Since the likelihood in Equation (5.10) is defined in terms of the difference flux, $Y_{i,t}$, which is calculated from a template spectrum, we use the template estimation approach on Holzer et al. (2021a) for each star. The likelihood's transformed wavelength, $X_{i,t}$, also requires values of the parameters n, d_j, μ_j, and σ_j for each $j \in \{1, ..., n\}$. Here again we use the absorption feature finding algorithm and Gaussian fitting process of Holzer et al. (2021a).

5.4.1 HD 217014 (51 Pegasi)

We begin with the well-known star HD 217014 for which there is a known planet (Mayor and Queloz, 1995; Marcy et al., 1997; Butler et al., 2006; Wang and Ford, 2011b; Bedell et al., 2019; Wilson et al., 2019; Petersburg et al., 2020). EXPRES has 116 observations of HD 217014 that range from May, 2018 to October, 2020. Using all 116 of these spectra, we begin by correcting for the telluric contamination by removing the parts of the spectra where the normalized flux of the provided telluric model is less than 0.98, and divide out the normalized telluric flux from the normalized observed flux everywhere else. We then limit each spectrum to be between 4850 and 6800 Å as both the Signal-to-Noise Ratio (SNR) decreases below 4850 Å and there are many telluric features that are not well modeled above

6800 Å.

By applying the proposed methodology of Section 5.2, with the same prior distributions as in Section 5.2.3, we obtain samples from the posterior distribution as shown in Figure 5.4.

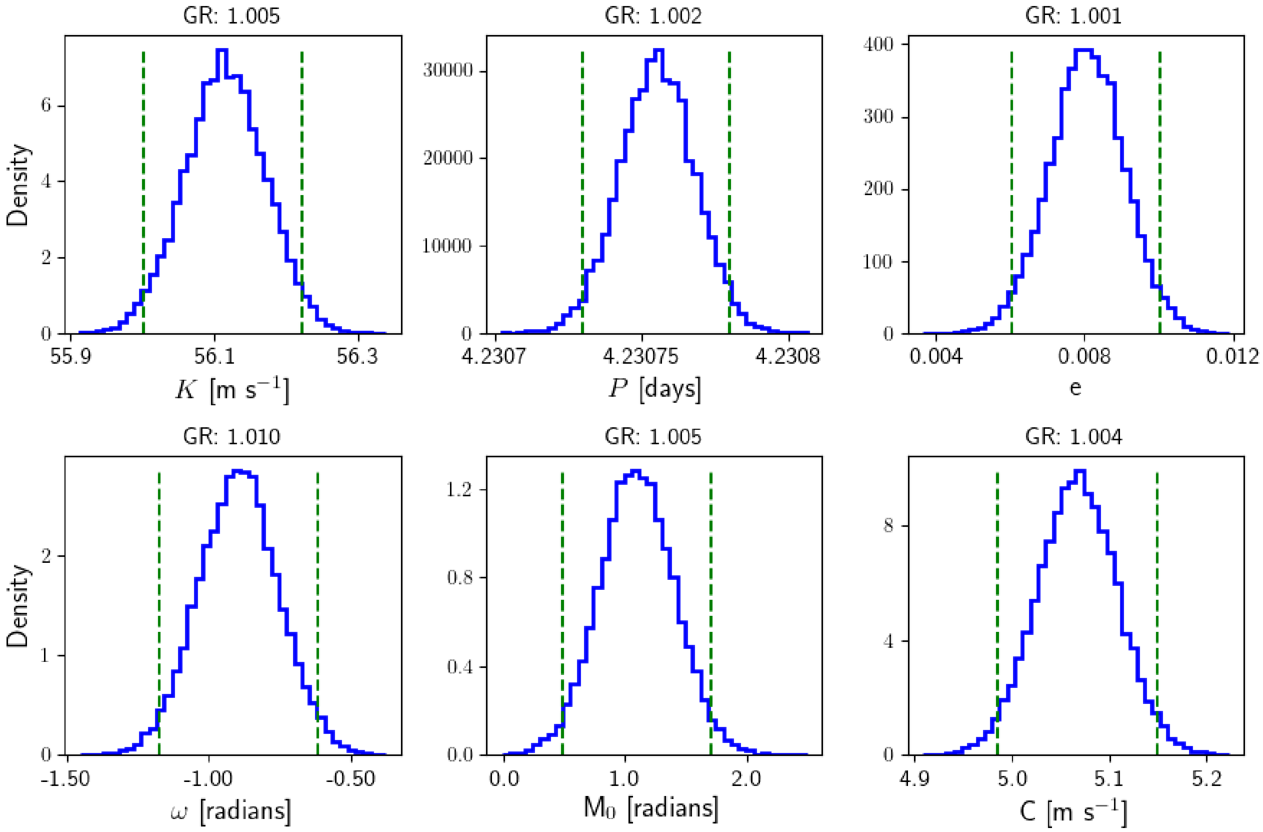

Figure 5.4: Sampling from the posterior distribution for HD 217014. Histograms are shown in solid blue. 95% CI are shown in vertical dashed lines. The GR statistic for each parameter is shown on top of the corresponding panel. No samplings at the beginning of the Markov chain are excluded.

Since the maximum of the six GR statistics is 1.010 we conclude that the Markov chain is sampling the posterior. The posterior means and 95% CI's for the six orbital parameters are given in Table 5.3.

These derived orbital parameter values match well with those reported in existing literature. Furthermore, to the best of our knowledge these are the most precise measurements

	MLE	95% **Conf. Int.**	**Post. Mean**	95% **CI**	Units
K	56.116	$(56.005, 56.223)$	56.114	$(56.001, 56.223)$	m s^{-1}
P	4.23076	$(4.23073, 4.23078)$	4.23076	$(4.23073, 4.23078)$	days
e	0.0081	$(0.0061, 0.0100)$	0.0081	$(0.0060, 0.0101)$	
ω	-0.886	$(-1.169, -0.626)$	-0.900	$(-1.173, -0.618)$	radians
M_0	1.092	$(0.487, 1.701)$	1.094	$(0.488, 1.702)$	radians
C	5.066	$(4.985, 5.149)$	5.067	$(4.985, 5.149)$	m s^{-1}

Table 5.3: HD 217014 derived orbital parameters. The maximum likelihood estimator (MLE) is given in the first column. The 95% confidence interval, which is calculated using the diagonal of the estimated covariance matrix and applying the Delta Method (also referred to as propagation of uncertainty), is given in the second column. The posterior mean and the 95% CI are given in the third and fourth column respectively. And the units of each parameter are specified in the last column.

of K, P, e, and ω so far reported for HD 217014.[5] Perhaps the most interesting aspect highlighted in Figure 5.4 and Table 5.3 is that this is the first instance in existing literature where the eccentricity e of the planetary orbit around HD 217014 is significantly non-zero, which also allows for a much tighter constraint on the angle of periastron ω.

5.4.2 HD 3651

Next we apply the methodology to the star HD 3651 which is known to have a single high-eccentricity planetary companion (Fischer et al., 2003; Butler et al., 2006; Wittenmyer et al., 2019; Brewer et al., 2020). This star was observed 137 times by EXPRES between August, 2019 and December 2020. Using all the collected spectra with the same corrections as in Section 5.4.1, applying our single-step methodology gives the posterior sampling shown in Figure 5.5.

Once again, since the maximum GR statistic is 1.009, we conclude that the Markov chain is sampling the posterior. Table 5.4 gives a more detailed overview of both the posterior inference and MLE for each parameter.

---

[5] For HD 217014, the most precise measurements for K, P, e, and ω are given in Petersburg et al. (2020), Wang and Ford (2011b), Petersburg et al. (2020), and Bedell et al. (2019) respectively, upon which the width of our 95% CI's give a 56%, 66%, 66%, and 83% improvement respectively.

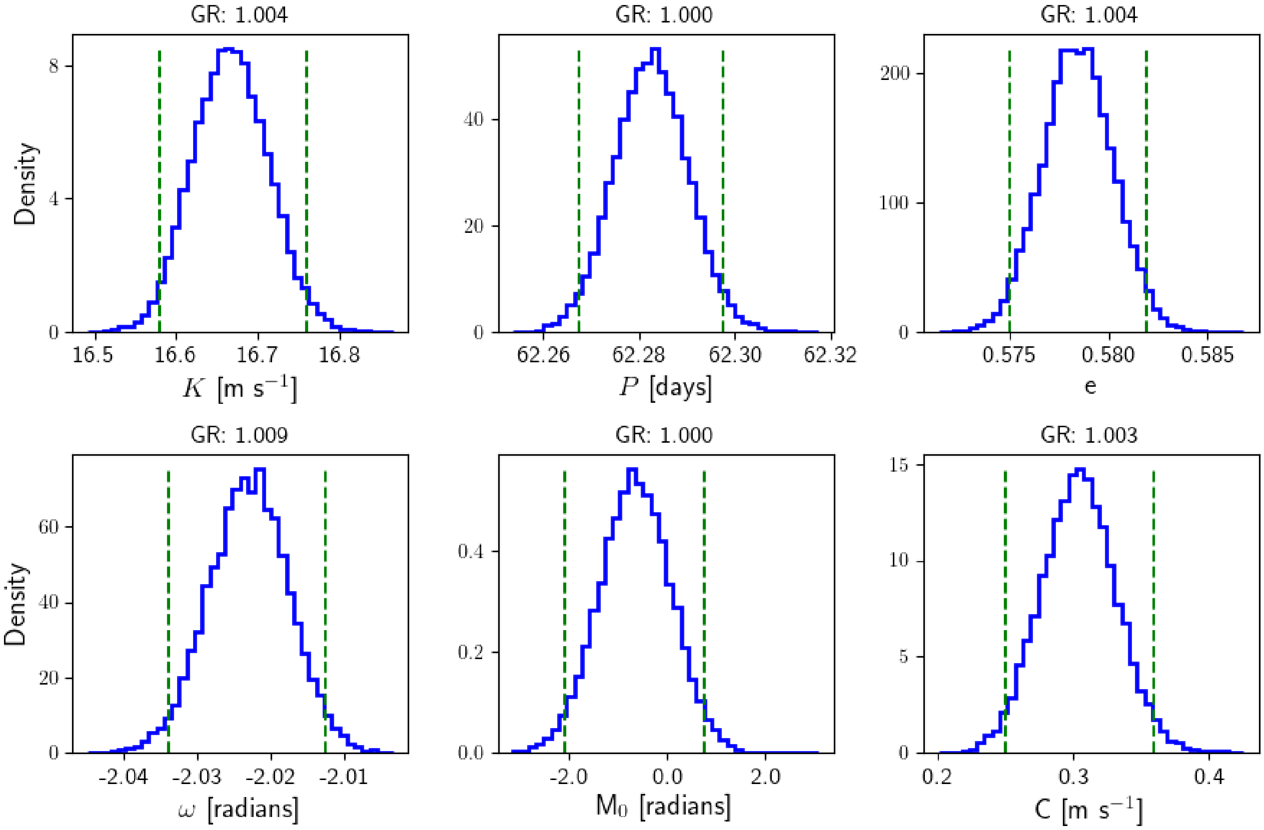

Figure 5.5: Sampling from the posterior distribution for HD 3651. Histograms are shown in solid blue. 95% CI are shown in vertical dashed lines. The GR statistic for each parameter is shown on top of the corresponding panel. No samplings at the beginning of the Markov chain are excluded.

	MLE	95% **Conf. Int.**	**Post. Mean**	95% **CI**	Units
K	16.655	$(16.565, 16.745)$	16.666	$(16.580, 16.759)$	m s^{-1}
P	62.288	$(62.273, 62.304)$	62.282	$(62.268, 62.298)$	days
e	0.5780	$(0.5744, 0.5815)$	0.5784	$(0.5750, 0.5820)$	
ω	-2.022	$(-2.033, -2.011)$	-2.023	$(-2.034, -2.013)$	radians
M_0	-1.225	$(-2.713, 0.262)$	-0.656	$(-2.099, 0.767)$	radians
C	0.297	$(0.243, 0.352)$	0.304	$(0.250, 0.359)$	m s^{-1}

Table 5.4: HD 3651 derived orbital parameters. The maximum likelihood estimator (MLE) is given in the first column. The 95% confidence interval, which is calculated using the diagonal of the estimated covariance matrix and applying the Delta Method (also referred to as propagation of uncertainty), is given in the second column. The posterior mean and the 95% CI are given in the third and fourth column respectively. And the units of each parameter are specified in the last column.

Our derived values for K and ω are in agreement with existing literature. Furthermore, the width of our 95% CI's for K and ω give a 79% and 90% improvement on the most precise values reported in Brewer et al. (2020) and Wittenmyer et al. (2019) respectively. However, our results suggest that the exoplanet around HD 3651 has a slightly longer orbital period and less eccentric orbit than that reported in Wittenmyer et al. (2019). As a check, we evaluated the parameter region suggested by Wittenmyer et al. (2019) and found no points at which the likelihood is greater than that at the MLE in Table 5.4. While the 95% CI reported in Wittenmyer et al. (2019) for P has approximately half the width of that in Table 5.4, our 95% CI for e has a width that is approximately one-tenth that of Wittenmyer et al. (2019).

5.4.3 HD 141004

Finally, we use the set of spectra collected by EXPRES for the star HD 141004 which has a recently discovered exoplanet orbiting it (Hirsch et al., 2021; Rosenthal et al., 2021). There were 160 observations of this star between Apr. 26, 2018 and June 20, 2021. Figure 5.6 gives the posterior sampling from our single-step methodology, and Table 5.5 details the MLE, posterior mean, 95% confidence intervals, and 95% CI's for the orbital parameters.

	MLE	95% **Conf. Int.**	**Post. Mean**	95% **CI**	Units
K	6.137	$(6.016, 6.257)$	6.133	$(6.017, 6.253)$	m s^{-1}
P	15.483	$(15.482, 15.485)$	15.483	$(15.482, 15.485)$	days
e	0.427	$(0.408, 0.446)$	0.426	$(0.407, 0.445)$	
ω	-1.740	$(-1.784, -1.696)$	-1.739	$(-1.783, -1.694)$	radians
M_0	-0.21	$(-2.20, 1.77)$	-0.27	$(-2.26, 1.67)$	radians
C	0.367	$(0.295, 0.440)$	0.367	$(0.293, 0.440)$	m s^{-1}

Table 5.5: HD 141004 derived orbital parameters. The maximum likelihood estimator (MLE) is given in the first column. The 95% confidence interval, which is calculated using the diagonal of the estimated covariance matrix and applying the Delta Method (also referred to as propagation of uncertainty), is given in the second column. The posterior mean and the 95% CI are given in the third and fourth column respectively. And the units of each parameter are specified in the last column.

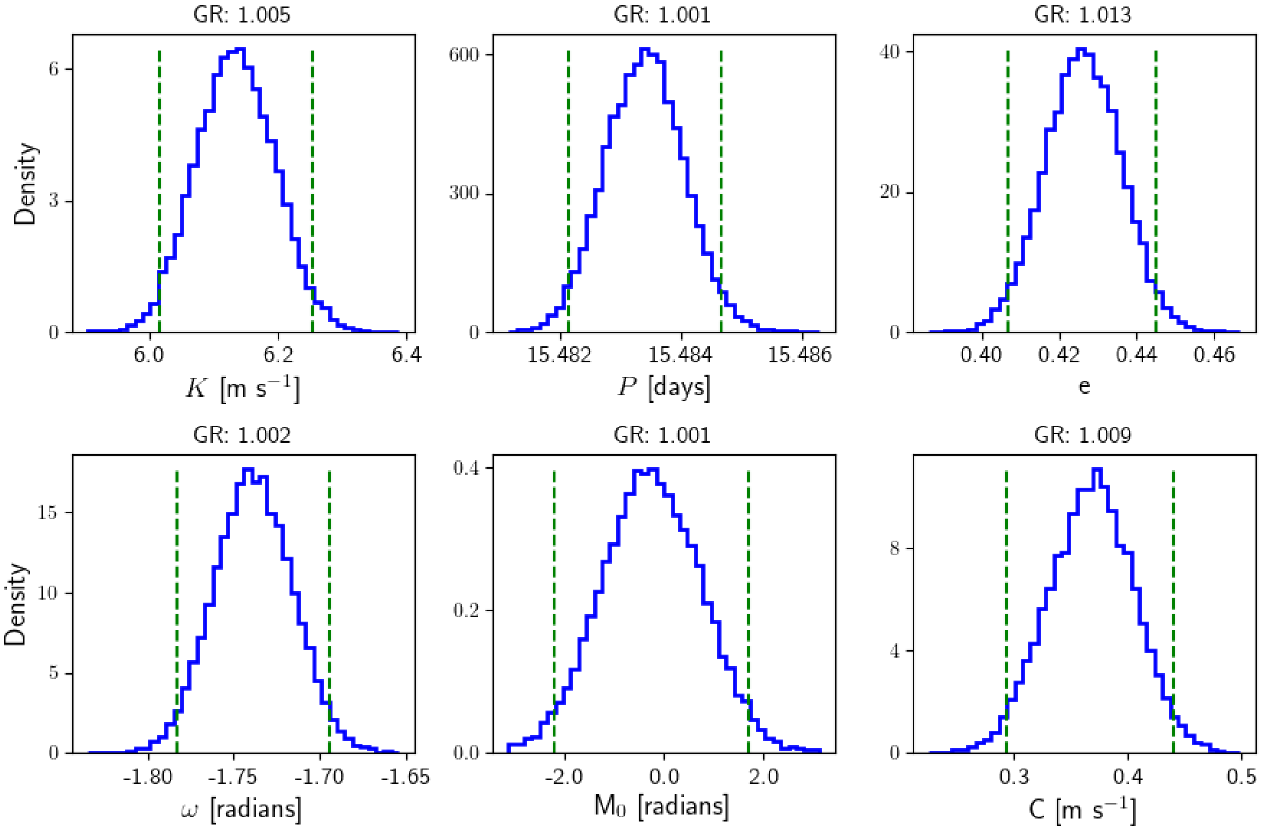

Figure 5.6: Sampling from the posterior distribution for HD 141004. Histograms are shown in solid blue. 95% CI are shown in vertical dashed lines. The GR statistic for each parameter is shown on top of the corresponding panel. No samplings at the beginning of the Markov chain are excluded.

As with HD 217014, this is the first time the exoplanet around HD 141004 has been found to have an eccentricity that is significantly non-zero. Furthermore, we find that our estimate for K is significantly larger than that reported in Hirsch et al. (2021). In addition, we find that the orbital period is slightly (with statistical significance) below that reported in both Hirsch et al. (2021) and Rosenthal et al. (2021). We thoroughly searched the parameter space suggested by Hirsch et al. (2021) and Rosenthal et al. (2021) but all points in this region had a likelihood value that was significantly less than that at the MLE reported in Table 5.5.

5.5 Discussion

We introduce a method that allows for one to go directly from a time-series of stellar spectra to inferring the values of exoplanet parameters, without any need to explicitly calculate the RV at each observation time.

In Section 5.3.1 we demonstrated that at high values of eccentricity, our gridsearch optimization approach outperforms the traditional attempt to calculate the MLE by first estimating the RV at each time and using them in a Lomb-Scargle periodogram. This suggests that many highly-eccentric exoplanets have remained undiscovered that may now be detectable with our new approach.

Unlike in Ford (2006), we find that a single reparameterization of the exoplanet parameters is sufficient for posterior sampling in both low- and high-eccentricity orbits. Furthermore, while Ford (2006) provides an algorithm for adjusting the proposal distribution in MCMC, noting that this has a major effect on the rate of convergence, we find that by estimating the covariance matrix and using it in a multivariate normal proposal distribution essentially eliminates the need for such an algorithm. There are many reasons for why this is likely the case. First, as previously mentioned, it is very common for the parameters to be strongly correlated to each other. Furthermore, we find that which parameters have such correlations does not remain consistent. Our approach of using an estimated covariance matrix in a multivariate Normal proposal distribution allows us to account for such correlations when sampling the posterior.

A second reason why using a multivariate Normal proposal distribution is advantageous is that it removes the need to repeatedly adjust the step size in each parameter based on the acceptance rate of previous Markov steps. Under the assumption that the priors do not heavily affect the posterior, the curvature of the log-likelihood gives a good initial estimate of the uncertainty in each parameter. And this can inform us of how large the Markov step should be in each parameter. All of this is accounted for when using the multivariate Normal proposal.

We find that the most computationally expensive component of our single-step implementation of the RV method is the calculating of the orbital parameters' MLE. Fortunately, our gridsearch approach is easily parallelized to speed this up significantly. If, however, one finds that a gridsearch optimization is still not suitable, one could still choose to calculate RV estimates and use a periodogram as usual. In this case, which is what we did for the application to HD 141004 in Section 5.4.3, we recommend still running a gridsearch over high-eccentricity orbits that could be missed with a periodogram (see Section 5.3).

Perhaps the most notable potential of our demonstrated methodology is in extending it to correct for effects such as stellar activity and tellurics. Many methods have been developed for correcting the effects of stellar activity. Some do so by aiming to correct initial RV estimates using either stellar activity indicators calculated from a cross-correlation function (Gilbertson et al., 2020c) or the cross-correlation function itself (Jones et al., 2017; Zhao and Tinney, 2020; Collier Cameron et al., 2021). Since these approaches are applied using the dimensionally-reduced data, they are specifically targeting spectrum-wide effects of stellar activity. Other methods note that stellar activity affects different spectral lines differently, and therefore aim to correct for activity-sensitive spectral lines in the RV estimation (Dumusque, 2018; Ning et al., 2019; Cretignier et al., 2020; Lafarga et al., 2020). Because our likelihood in Equation (5.10) is defined by the time series of stellar spectra, it is kept general enough to easily be adjusted to include both spectrum-wide and line-specific effects of stellar activity. In addition, the likelihood could be adjusted to include a time-varying component for tellurics as in Bedell et al. (2019).

5.6 Conclusion

We find that the RV method for discovering exoplanets need not include a step of explicitly estimating the RV from each observed spectrum. Instead, it is computationally feasible to estimate the orbital parameters of a potential exoplanet directly from the time series of spectra from the host star.

Bibliography

Akeson, R., Chen, X., Ciardi, D., Crane, M., Good, J., Harbut, M., Jackson, E., Kane, S., Laity, A., Leifer, S., et al. (2013). The nasa exoplanet archive: data and tools for exoplanet research. *Publications of the Astronomical Society of the Pacific*, 125(930):989. 123

Anglada-Escudé, G. and Butler, R. P. (2012). The harps-terra project. i. description of the algorithms, performance, and new measurements on a few remarkable stars observed by harps. *The Astrophysical Journal Supplement Series*, 200(2):15. 15, 16, 18, 117

Astudillo-Defru, N., Bonfils, X., Delfosse, X., Ségransan, D., Forveille, T., Bouchy, F., Gillon, M., Lovis, C., Mayor, M., Neves, V., et al. (2015). The harps search for southern extra-solar planets-xxxvi. planetary systems and stellar activity of the m dwarfs gj 3293, gj 3341, and gj 3543. *Astronomy & Astrophysics*, 575:A119. 16, 117

Baranne, A., Queloz, D., Mayor, M., Adrianzyk, G., Knispel, G., Kohler, D., Lacroix, D., Meunier, J.-P., Rimbaud, G., and Vin, A. (1996). Elodie: A spectrograph for accurate radial velocity measurements. *Astronomy and Astrophysics Supplement Series*, 119(2):373–390. 15, 16, 73

Barker, P. (1984). Ripple correction of high-dispersion iue spectra-blazing echelles. *The Astronomical Journal*, 89:899–903. 57, 118

Bedell, M., Hogg, D. W., Foreman-Mackey, D., Montet, B. T., and Luger, R. (2019). wobble: a data-driven analysis technique for time-series stellar spectra. *The Astronomical Journal*, 158(4):164. 57, 65, 138, 140, 145

Blackman, R. T., Fischer, D. A., Jurgenson, C. A., Sawyer, D., McCracken, T. M., Szymkowiak, A. E., Petersburg, R. R., Ong, J. J., Brewer, J. M., Zhao, L. L., et al. (2020). Performance verification of the extreme precision spectrograph. *The Astronomical Journal*, 159(5):238. 8, 15, 29, 57, 61, 118

Blackman, R. T., Szymkowiak, A. E., Fischer, D. A., and Jurgenson, C. A. (2017). Accounting for chromatic atmospheric effects on barycentric corrections. *The Astrophysical Journal*, 837(1):18. 8, 29, 57, 118

Boisse, I., Bouchy, F., Hébrard, G., Bonfils, X., Santos, N., and Vauclair, S. (2011). Disentangling between stellar activity and planetary signals. *Astronomy & Astrophysics*, 528:A4. 73

Bonferroni, C. (1936). Teoria statistica delle classi e calcolo delle probabilita. *Pubblicazioni del R Istituto Superiore di Scienze Economiche e Commericiali di Firenze*, 8:3–62. 84

Bouchy, F., Pepe, F., and Queloz, D. (2001). Fundamental photon noise limit to radial velocity measurements. *Astronomy & Astrophysics*, 374(2):733–739. 16, 20, 32, 117

Branch, M. A., Coleman, T. F., and Li, Y. (1999). A subspace, interior, and conjugate gradient method for large-scale bound-constrained minimization problems. *SIAM Journal on Scientific Computing*, 21(1):1–23. 60

Brewer, J. M., Fischer, D. A., Blackman, R. T., Cabot, S. H., Davis, A. B., Laughlin, G., Leet, C., Ong, J. J., Petersburg, R. R., Szymkowiak, A. E., et al. (2020). Expres. i. hd 3651 as an ideal rv benchmark. *The Astronomical Journal*, 160(2):67. 140, 142

Brooks, S. P. and Gelman, A. (1998). General methods for monitoring convergence of iterative simulations. *Journal of computational and graphical statistics*, 7(4):434–455. 128

Butler, R. P., Marcy, G. W., Fischer, D. A., Brown, T. M., Contos, A. R., Korzennik, S. G., Nisenson, P., and Noyes, R. W. (1999). Evidence for multiple companions to υ andromedae. *The Astrophysical Journal*, 526(2):916. 3

Butler, R. P., Marcy, G. W., Williams, E., McCarthy, C., Dosanjh, P., and Vogt, S. S. (1996). Attaining doppler precision of 3 m s-1. *Publications of the Astronomical Society of the Pacific*, 108(724):500. 32

Butler, R. P., Wright, J., Marcy, G., Fischer, D., Vogt, S., Tinney, C., Jones, H., Carter, B., Johnson, J., McCarthy, C., et al. (2006). Catalog of nearby exoplanets. *The Astrophysical Journal*, 646(1):505. 138, 140

Candès, E. J., Li, X., Ma, Y., and Wright, J. (2011). Robust principal component analysis? *Journal of the ACM (JACM)*, 58(3):11. 82

Chaplin, W. J., Cegla, H. M., Watson, C. A., Davies, G. R., and Ball, W. H. (2019). Filtering solar-like oscillations for exoplanet detection in radial velocity observations. *The Astronomical Journal*, 157(4):163. 101

Ciuryło, R. (1998). Shapes of pressure-and doppler-broadened spectral lines in the core and near wings. *Physical Review A*, 58(2):1029. 31

Collier Cameron, A., Ford, E., Shahaf, S., Aigrain, S., Dumusque, X., Haywood, R., Mortier, A., Phillips, D., Buchhave, L., Cecconi, M., et al. (2021). Separating planetary reflex doppler shifts from stellar variability in the wavelength domain. *Monthly Notices of the Royal Astronomical Society*, 505(2):1699–1717. 145

Cosentino, R., Lovis, C., Pepe, F., Cameron, A. C., Latham, D. W., Molinari, E., Udry, S., Bezawada, N., Black, M., Born, A., et al. (2012). Harps-n: the new planet hunter at tng. In *Ground-based and Airborne Instrumentation for Astronomy IV*, volume 8446, page 84461V. International Society for Optics and Photonics. 15

Cretignier, M., Dumusque, X., Allart, R., Pepe, F., and Lovis, C. (2020). Measuring precise radial velocities on individual spectral lines-ii. dependance of stellar activity signal on line depth. *Astronomy & Astrophysics*, 633:A76. 17, 21, 72, 82, 117, 145

Cunha, D., Santos, N., Figueira, P., Santerne, A., Bertaux, J.-L., and Lovis, C. (2014). Impact of micro-telluric lines on precise radial velocities and its correction. *Astronomy & Astrophysics*, 568:A35. 116

Dai, C.-Q., Wang, Y., and Liu, J. (2016). Spatiotemporal hermite–gaussian solitons of a (3+ 1)-dimensional partially nonlocal nonlinear schrödinger equation. *Nonlinear Dynamics*, 84(3):1157–1161. 19

Dall, T., Santos, N., Arentoft, T., Bedding, T., and Kjeldsen, H. (2006). Bisectors of the cross-correlation function applied to stellar spectra-discriminating stellar activity, oscillations and planets. *Astronomy & Astrophysics*, 454(1):341–348. 73

Davis, A. B., Cisewski, J., Dumusque, X., Fischer, D. A., and Ford, E. B. (2017). Insights on the spectral signatures of stellar activity and planets from pca. *The Astrophysical Journal*, 846(1):59. 17, 69, 72, 73, 82

Delisle, J.-B., Ségransan, D., Dumusque, X., Diaz, R., Bouchy, F., Lovis, C., Pepe, F., Udry, S., Alonso, R., Benz, W., et al. (2018). The harps search for southern extra-solar planets-xliii. a compact system of four super-earth planets orbiting hd 215152. *Astronomy & Astrophysics*, 614:A133. 69

Desort, M., Lagrange, A.-M., Galland, F., Udry, S., and Mayor, M. (2007). Search for exoplanets with the radial-velocity technique: quantitative diagnostics of stellar activity. *Astronomy & Astrophysics*, 473(3):983–993. 17, 69, 72, 116

Doppler, C. (1842). *Über das farbige Licht der Doppelsterne und einiger anderer Gestirne des Himmels*. Calve. 2, 4, 28

Dumusque, X. (2018). Measuring precise radial velocities on individual spectral lines-i. validation of the method and application to mitigate stellar activity. *Astronomy & Astrophysics*, 620:A47. 16, 17, 21, 72, 104, 117, 145

Dumusque, X., Boisse, I., and Santos, N. (2014). Soap 2.0: A tool to estimate the photometric and radial velocity variations induced by stellar spots and plages. *The Astrophysical Journal*, 796(2):132. 69, 81, 106

Dumusque, X., Borsa, F., Damasso, M., Díaz, R. F., Gregory, P., Hara, N., Hatzes, A., Rajpaul, V., Tuomi, M., Aigrain, S., et al. (2017). Radial-velocity fitting challenge-ii.

first results of the analysis of the data set. *Astronomy & Astrophysics*, 598:A133. 17, 69, 72

Einstein, A. et al. (1905). On the electrodynamics of moving bodies. *Annalen der Physik*, 17(891):50. 29

Figueira, P., Santos, N., Pepe, F., Lovis, C., and Nardetto, N. (2013). Line-profile variations in radial-velocity measurements-two alternative indicators for planetary searches. *Astronomy & Astrophysics*, 557:A93. 73

Fischer, D. A., Anglada-Escude, G., Arriagada, P., Baluev, R. V., Bean, J. L., Bouchy, F., Buchhave, L. A., Carroll, T., Chakraborty, A., Crepp, J. R., et al. (2016). State of the field: extreme precision radial velocities. *Publications of the Astronomical Society of the Pacific*, 128(964):066001. 13, 17, 72, 116

Fischer, D. A., Butler, R. P., Marcy, G. W., Vogt, S. S., and Henry, G. W. (2003). A sub-saturn mass planet orbiting hd 3651. *The Astrophysical Journal*, 590(2):1081. 140

Ford, E. B. (2005). Quantifying the uncertainty in the orbits of extrasolar planets. *The Astronomical Journal*, 129(3):1706. 121

Ford, E. B. (2006). Improving the efficiency of markov chain monte carlo for analyzing the orbits of extrasolar planets. *The Astrophysical Journal*, 642(1):505. 121, 123, 144

Frank, S. (2008). *OVI absorbers in SDSS spectra*. PhD thesis, The Ohio State University. 21

Frick, P., Baliunas, S., Galyagin, D., Sokoloff, D., and Soon, W. (1997). Wavelet analysis of stellar chromospheric activity variations. *The Astrophysical Journal*, 483(1):426. 94

Fulton, B. J., Petigura, E. A., Blunt, S., and Sinukoff, E. (2018). Radvel: the radial velocity modeling toolkit. *Publications of the Astronomical Society of the Pacific*, 130(986):044504. 137

Gelman, A., Rubin, D. B., et al. (1992). Inference from iterative simulation using multiple sequences. *Statistical science*, 7(4):457–472. 128

Giguere, M. J., Fischer, D. A., Zhang, C. X., Matthews, J. M., Cameron, C., and Henry, G. W. (2016). A combined spectroscopic and photometric stellar activity study of epsilon eridani. *The Astrophysical Journal*, 824(2):150. 69, 73

Gilbertson, C., Ford, E. B., and Dumusque, X. (2020a). Towards extremely precise radial velocities: I. simulated solar spectra for testing exoplanet detection algorithms. *arXiv preprint arXiv:2005.01489*. 93, 102

Gilbertson, C., Ford, E. B., Jones, D. E., and Stenning, D. C. (2020b). Toward extremely precise radial velocities. ii. a tool for using multivariate gaussian processes to model stellar activity. *The Astrophysical Journal*, 905(2):155. 103

Gilbertson, C., Ford, E. B., Jones, D. E., and Stenning, D. C. (2020c). Toward extremely precise radial velocities. ii. a tool for using multivariate gaussian processes to model stellar activity. *The Astrophysical Journal*, 905(2):155. 145

Gray, D. (1984). Measurements of rotation and turbulence in f, g, and k dwarfs. *The Astrophysical Journal*, 281:719–722. 94

Gray, D. F. (2005). *The observation and analysis of stellar photospheres*. Cambridge University Press. 29, 31

Gray, D. F. and Baliunas, S. L. (1995). Magnetic activity variations of epsilon eridani. *The Astrophysical Journal*, 441:436–442. 94

Halverson, S., Terrien, R., Mahadevan, S., Roy, A., Bender, C., Stefánsson, G. K., Monson, A., Levi, E., Hearty, F., Blake, C., et al. (2016). A comprehensive radial velocity error budget for next generation doppler spectrometers. In *Ground-based and Airborne Instrumentation for Astronomy VI*, volume 9908, page 99086P. International Society for Optics and Photonics. 116

Han, E., Wang, S. X., Wright, J. T., Feng, Y. K., Zhao, M., Fakhouri, O., Brown, J. I., and Hancock, C. (2014). Exoplanet Orbit Database. II. Updates to Exoplanets.org. *Proceedings of the Astronomical Society of the Pacific*, 126(943):827. ix, 14, 116

Hatzes, A. P. (2002). Starspots and exoplanets. *Astronomische Nachrichten*, 323(3-4):392–394. 17, 69, 72

Hirsch, L. A., Rosenthal, L., Fulton, B. J., Howard, A. W., Ciardi, D. R., Marcy, G. W., Nielsen, E., Petigura, E. A., de Rosa, R. J., Isaacson, H., et al. (2021). Understanding the impacts of stellar companions on planet formation and evolution: A survey of stellar and planetary companions within 25 pc. *The Astronomical Journal*, 161(3):134. 142, 143

Holzer, P. H., Cisewski-Kehe, J., Fischer, D., and Zhao, L. (2021a). A hermite–gaussian based exoplanet radial velocity estimation method. *The Annals of Applied Statistics*, 15(2):527–555. 18, 117, 118, 125, 127, 137, 138

Holzer, P. H., Cisewski-Kehe, J., Zhao, L., Ford, E. B., Gilbertson, C., and Fischer, D. A. (2021b). A stellar activity f-statistic for exoplanet surveys (safe). *The Astronomical Journal*, 161(6):272. 72

Isaacson, H. and Fischer, D. (2010). Chromospheric activity and jitter measurements for 2630 stars on the california planet search. *The Astrophysical Journal*, 725(1):875. 17, 69, 72

Johnston, W. (2014). The weighted hermite polynomials form a basis for l 2 (r). *The American Mathematical Monthly*, 121(3):249–253. 30, 76

Jones, D. E., Stenning, D. C., Ford, E. B., Wolpert, R. L., Loredo, T. J., and Dumusque, X. (2017). Improving exoplanet detection power: Multivariate gaussian process models for stellar activity. *arXiv preprint arXiv:1711.01318*. 17, 72, 73, 101, 145

Jurgenson, C., Fischer, D., McCracken, T., Sawyer, D., Szymkowiak, A., Davis, A., Muller, G., and Santoro, F. (2016). Expres: a next generation rv spectrograph in the search for earth-like worlds. In *Ground-based and Airborne Instrumentation for Astronomy VI*, volume 9908, page 99086T. International Society for Optics and Photonics. 15, 57, 74, 117, 138

Kelch, W. (1978). Stellar model chromospheres. viii-70 ophiuchi a/k0 v/and epsilon eridani/k2 v. *The Astrophysical Journal*, 222:931–940. 94

Labutin, T. A., Zaytsev, S. M., and Popov, A. M. (2013). Automatic identification of emission lines in laser-induced plasma by correlation of model and experimental spectra. *Analytical chemistry*, 85(4):1985–1990. 21

Lafarga, M., Ribas, I., Lovis, C., Perger, M., Zechmeister, M., Bauer, F., Kürster, M., Cortés-Contreras, M., Morales, J., Herrero, E., et al. (2020). The carmenes search for exoplanets around m dwarfs-radial velocities and activity indicators from cross-correlation functions with weighted binary masks. *Astronomy & Astrophysics*, 636:A36. 145

Lagrange, A.-M., Desort, M., and Meunier, N. (2010). Using the sun to estimate earth-like planets detection capabilities-i. impact of cold spots. *Astronomy & Astrophysics*, 512:A38. 17, 69, 72

Lanczos, C. (1938). Trigonometric interpolation of empirical and analytical functions. *Journal of Mathematics and Physics*, 17(1-4):123–199. 29, 76

Leet, C., Fischer, D. A., and Valenti, J. A. (2019). Toward a self-calibrating, empirical, light-weight model for tellurics in high-resolution spectra. *The Astronomical Journal*, 157(5):187. 8, 58, 95

Marcy, G. W., Butler, R. P., Williams, E., Bildsten, L., Graham, J. R., Ghez, A. M., and Jernigan, J. G. (1997). The planet around 51 pegasi. *The Astrophysical Journal*, 481(2):926. 57, 65, 138

Marhic, M. (1978). Oscillating hermite-gaussian wave functions of the harmonic oscillator. *Lett. Nuovo Cim*, 22(9):376–378. 19

Mayor, M., Pepe, F., and Queloz, D. (2003). Setting new standards with harps. *The Messenger*, 114(1):20. 15

Mayor, M. and Queloz, D. (1995). A jupiter-mass companion to a solar-type star. *Nature*, 378(6555):355. 3, 57, 75, 116, 138

Mészáros, S. and Prieto, C. A. (2013). On the interpolation of model atmospheres and high-resolution synthetic stellar spectra. *Monthly Notices of the Royal Astronomical Society*, 430(4):3285–3291. 44, 58, 62

Metropolis, N., Rosenbluth, A. W., Rosenbluth, M. N., Teller, A. H., and Teller, E. (1953). Equation of state calculations by fast computing machines. *The journal of chemical physics*, 21(6):1087–1092. 125

Meunier, N., Desort, M., and Lagrange, A.-M. (2010). Using the sun to estimate earth-like planets detection capabilities-ii. impact of plages. *Astronomy & Astrophysics*, 512:A39. 17, 69, 72, 116

Moré, J. J. (1978). The levenberg-marquardt algorithm: implementation and theory. In *Numerical analysis*, pages 105–116. Springer. 66, 122

Ning, B., Wise, A., Cisewski-Kehe, J., Dodson-Robinson, S., and Fischer, D. (2019). Identifying activity-sensitive spectral lines: A bayesian variable selection approach. *The Astronomical Journal*, 158(5):210. 104, 145

Paulson, D. B., Cochran, W. D., and Hatzes, A. P. (2004). Searching for planets in the hyades. v. limits on planet detection in the presence of stellar activity. *The Astronomical Journal*, 127(6):3579. 69

Pepe, F., Mayor, M., Galland, F., Naef, D., Queloz, D., Santos, N., Udry, S., and Burnet, M. (2002). The coralie survey for southern extra-solar planets vii-two short-period saturnian companions to hd 108147 and hd 168746. *Astronomy & Astrophysics*, 388(2):632–638. 15, 16, 73, 75

Petersburg, R. R., Ong, J. J., Zhao, L. L., Blackman, R. T., Brewer, J. M., Buchhave, L. A., Cabot, S. H., Davis, A. B., Jurgenson, C. A., Leet, C., et al. (2020). An extreme-precision radial-velocity pipeline: First radial velocities from expres. *The Astronomical Journal*, 159(5):187. xxi, 9, 15, 16, 43, 54, 57, 61, 62, 63, 65, 66, 74, 75, 93, 117, 138, 140

Planck, M. (1901). On the law of distribution of energy in the normal spectrum. *Annalen der physik*, 4(553):1. 6, 8

Pont, F., Aigrain, S., and Zucker, S. (2011). Reassessing the radial-velocity evidence for planets around corot-7. *Monthly Notices of the Royal Astronomical Society*, 411(3):1953–1962. 73

Queloz, D., Bouchy, F., Moutou, C., Hatzes, A., Hébrard, G., Alonso, R., Auvergne, M., Baglin, A., Barbieri, M., Barge, P., et al. (2009). The corot-7 planetary system: two orbiting super-earths. *Astronomy & Astrophysics*, 506(1):303–319. 73

Queloz, D., Henry, G., Sivan, J., Baliunas, S., Beuzit, J., Donahue, R., Mayor, M., Naef, D., Perrier, C., and Udry, S. (2001). No planet for hd 166435. *Astronomy & Astrophysics*, 379(1):279–287. 17, 69, 72, 73, 116

Rajpaul, V., Aigrain, S., Osborne, M. A., Reece, S., and Roberts, S. (2015). A gaussian process framework for modelling stellar activity signals in radial velocity data. *Monthly Notices of the Royal Astronomical Society*, 452(3):2269–2291. 69, 101

Rajpaul, V. M., Aigrain, S., and Buchhave, L. A. (2020). A robust, template-free approach to precise radial velocity extraction. *Monthly Notices of the Royal Astronomical Society*, 492(3):3960–3983. 20

Rall, L. B. (1986). The arithmetic of differentiation. *Mathematics Magazine*, 59(5):275–282. 123

Riffel, R. A. (2010). profit: a new alternative for emission-line pro file fit ting. *Astrophysics and Space Science*, 327(2):239–244. 19

Rimmele, T. R. and Radick, R. R. (1998). Solar adaptive optics at the national solar observatory. In *Adaptive Optical System Technologies*, volume 3353, pages 72–82. International Society for Optics and Photonics. 9, 81

Rosenthal, L. J., Fulton, B. J., Hirsch, L. A., Isaacson, H. T., Howard, A. W., Dedrick, C. M., Sherstyuk, I. A., Blunt, S. C., Petigura, E. A., Knutson, H. A., et al. (2021). The california legacy survey i. a catalog of 177 planets from precision radial velocity monitoring of 719 nearby stars over three decades. *arXiv preprint arXiv:2105.11583*. 142, 143

Saar, S. H. and Donahue, R. A. (1997). Activity-related radial velocity variation in cool stars. *The Astrophysical Journal*, 485(1):319. 17, 69, 72, 94, 116

Scargle, J. D. (1982). Studies in astronomical time series analysis. ii-statistical aspects of spectral analysis of unevenly spaced data. *The Astrophysical Journal*, 263:835–853. 122, 127

Sharpee, B., Williams, R., Baldwin, J. A., and van Hoof, P. A. (2003). Introducing emili: Computer-aided emission line identification. *The Astrophysical Journal Supplement Series*, 149(1):157. 21

Simola, U., Dumusque, X., and Cisewski-Kehe, J. (2019). Measuring precise radial velocities and cross-correlation function line-profile variations using a skew normal density. *Astronomy & Astrophysics*, 622:A131. 69

Simon, T., Kelch, W., and Linsky, J. (1980). Outer atmospheres of cool stars. vi-models for epsilon eridani based on iue spectra of c ii, mg ii, si ii, and si iii. *The Astrophysical Journal*, 237:72–81. 94

Sneden, C., Bean, J., Ivans, I., Lucatello, S., and Sobeck, J. (2012). Moog: Lte line analysis and spectrum synthesis. *Astrophysics Source Code Library*. 45, 75

Thatcher, J. D., Robinson, R. D., and Rees, D. E. (1991). The chromospheres of late-type stars–i. ε eridani as a test case of multiline modelling. *Monthly Notices of the Royal Astronomical Society*, 250(1):14–23. 94

Tonegawa, M., Totani, T., Iwamuro, F., Akiyama, M., Dalton, G., Glazebrook, K., Ohta, K., Okada, H., and Yabe, K. (2015). Field: Automated emission line detection software for subaru/fmos near-infrared spectroscopy. *Publications of the Astronomical Society of Japan*, 67(3). 21

Tuomi, M., Anglada-Escudé, G., Gerlach, E., Jones, H. R., Reiners, A., Rivera, E. J., Vogt, S. S., and Butler, R. P. (2013). Habitable-zone super-earth candidate in a six-planet system around the k2. 5v star hd 40307. *Astronomy & Astrophysics*, 549:A48. 69

VanderPlas, J. T. (2018). Understanding the lomb–scargle periodogram. *The Astrophysical Journal Supplement Series*, 236(1):16. 128

Wang, J. and Ford, E. B. (2011a). On the eccentricity distribution of short-period single-planet systems. *Monthly Notices of the Royal Astronomical Society*, 418(3):1822–1833. 57, 65

Wang, J. and Ford, E. B. (2011b). On the eccentricity distribution of short-period single-planet systems. *Monthly Notices of the Royal Astronomical Society*, 418(3):1822–1833. 138, 140

Wengert, R. E. (1964). A simple automatic derivative evaluation program. *Communications of the ACM*, 7(8):463–464. 123

Wilson, M. L., Eastman, J. D., Cornachione, M. A., Wang, S. X., Johnson, S. A., Sliski, D. H., Schap III, W. J., Morton, T. D., Johnson, J. A., McCrady, N., et al. (2019). First radial velocity results from the miniature exoplanet radial velocity array (minerva). *Publications of the Astronomical Society of the Pacific*, 131(1005):115001. 138

Wise, A., Dodson-Robinson, S., Bevenour, K., and Provini, A. (2018). New methods for finding activity-sensitive spectral lines: Combined visual identification and an automated pipeline find a set of 40 activity indicators. *The Astronomical Journal*, 156(4):180. 104

Wittenmyer, R. A., Clark, J. T., Zhao, J., Horner, J., Wang, S., and Johns, D. (2019). Truly eccentric–i. revisiting eight single-eccentric planetary systems. *Monthly Notices of the Royal Astronomical Society*, 484(4):5859–5867. 140, 142

Wolszczan, A. and Frail, D. A. (1992). A planetary system around the millisecond pulsar psr1257+ 12. *Nature*, 355(6356):145–147. 3

Wright, J. and Eastman, J. (2014). Barycentric corrections at 1 cm s-1 for precise doppler velocities. *Publications of the Astronomical Society of the Pacific*, 126(943):838. 8, 29, 118

Xu, X., Cisewski-Kehe, J., Davis, A. B., Fischer, D. A., and Brewer, J. M. (2019). Modeling the echelle spectra continuum with alpha shapes and local regression fitting. *The Astronomical Journal*, 157(6):243. 9, 57, 118

Zhao, J. and Tinney, C. (2020). Fiesta–disentangling stellar variability from exoplanets in the fourier domain. *Monthly Notices of the Royal Astronomical Society*, 491(3):4131–4146. 145

Zhao, Y., Ge, J., Yuan, X., Zhao, T., Wang, C., and Li, X. (2019). Identifying mg ii narrow absorption lines with deep learning. *Monthly Notices of the Royal Astronomical Society*, 487(1):801–811. 21